Study of light effect on the electrical properties of a magnetic tunnel junction

Yong Xu

THÈSE

Pour l'obtention du titre de :

DOCTEUR de L'UNIVERSITÉ DE LORRAINE

Spécialité: *Physique*

Présentée par :

XU Yong

Etude des effets de la lumière sur les propriétés électriques d'une jonction tunnel magnétique

---

Thèse soutenue publiquement le 25 Novembre 2014 à Nancy devant le jury composé de :

M. Dafine Ravelosona	Directeur de Recherche CNRS, IEF	Rapporteur
M. Matthias Kläui	Professeur, Johannes Gutenberg-University Mainz	Rapporteur
M. Chia-Ling Chien	Professeur, Johns Hopkins University	Examinateur
M. Xiaofeng Jin	Professeur, Fudan University	Examinateur
M. Hervé Rinnert	Professeur, Université de Lorraine	Examinateur
M. Stéphane Mangin	Professeur, Université de Lorraine	Directeur de thèse
M. Michel Hehn	Professeur, Université de Lorraine	Co-directeur de thèse
M. Yuan Lu	Ingénieur de Recherche CNRS, IJL	Co-directeur de thèse

TABLE DES MATIÈRES

LISTE DES ILLUSTRATIONS

REMERCIEMENTS

My deepest gratitude goes first to my supervisor *Stéphane Mangin*. In fact, I never thought I would obtain a PhD degree in France until I met him in Beijing about four years ago. He was in a tour of scientific visit to several cities in China. After the visit, he proposed that I can try to apply for a PhD position in Nancy. Luckily it works. I'd like to thank *Stéphane* not only for offering the PhD position, but also the pleasant experience of working and discussing together. As an energetic professor (probably the most energetic that I have ever seen), he is very active in all kinds of scientific activities. His experience and instruction have been invaluable in helping me research and present my findings

During the past three years, *Michel Hehn* has done all the samples discussed in the thesis. I work a lot with *Michel*, especially during the second year when *Stéphane* was working in the USA. I thank the other co-supervisor *Yuan Lu.* He seems to know everything about semiconductor materials. I will always remember the first day that I arrived in Nancy and did not speak French at all, he helped me with everything that needs French: apartment, bank, insurance, registration etc. Thanks to *Sébastien Petit-Watelot*, who is really an expert in dynamics and magnetism. We worked together on lock-in amplifier, COMSOL software, signal amplifier and function generator and other scientific equipment or software. Without him, I would not be able to achieve with comprehensive understanding of the challenging problems. In the third year of my thesis, I work *Hervé Rinnert* a lot on his laser setup, including the OPO laser setup and Raman setup. Those results are of great importance in the clarification of the puzzles that we encountered. I benefit a lot from the discussion with *Daniel Lacour* and his help when facing problems with setup and software. *François Montaigne* is the head of clean room and a lot of thanks for his help in sample design and lithography process.

I am grateful for *Karine Dumesnil*'s help during my application for the scholarship of PhD position. Thanks to *Thomas Hauet*, the head of CC Magnétisme. I appreciate the support from *Stéphane Andrieu* when studying MgO-based MTJs. *Philippe Lambert* helped me in printing the thesis, organization of the 'pot de thèse' and so on.

I would like to acknowledge *Gwladys Lengaigne* for all the MTJs that she processed and the excellent training about the equipment in the clean room that she has done for me. Thanks to *Laurent Bouvot* for solving the problems that I encountered when cutting the samples and doing wire-bonding. Thanks to *Stefan Mc-Murtry* for his help with E-beam lithography. *Stéphane Suire* is always helpful when people are dealing with the problems of magnetic measurements.

I need to acknowledge all the PhD students and post-docs in team of nanomagnetism and spintronics. *Mathias Bersweiler* worked with me in a same office for more than two years. Thanks a lot for the numerous rides … Thanks to *Amina Neggache*. I really admire her for her ability to master four languages. Thanks to *Weiwei Lin* for his suggestions and discussion during the research. *Tao Liu, Shiheng Liang and Bingshan Tao* were already my friends in Beijing four years ago. I feel very fortunate to meet them again in Nancy. Many thanks and best wishes to *Charles-Henri Lambert*, *Damien Louis*, *Mohammed-Salah Elhadri*, *Marion Lavanant-Jambert*, *Robert Tolley* and those have left Nancy: *Christel Berthelot, Hanna Riahi*, *Amandine Duluard*, *Mathieu Da Silva*, *Sylvain Le Gall*, *Kaname Mitsuzuka* and *Rajani kanth Ammanabrolu*. Thanks to *Norman Haag*, our colleague in University of Kaiserslautern, for the kind reception when I performed experiments there.

Thanks a lot to the friends that I meet in Nancy. I enjoy very much our time together. Last and most important, I would like to thank and dedicate this thesis to my girlfriend and my parents.

0-1 CONTEXT

Magnetic materials and devices have played a major role in science and technology for the last half century. Hard disk drives dominate information storage [1,2] and magnetic random access memory (MRAM) is emerging in the field of memory [3]. Advances in new magnetic materials and devices will be crucial for continued progress in computation and data storage in the face of dramatic increases in power consumption in highly scaled CMOS devices.

The International Technology Roadmap for Semiconductors [4] has forecast a "red brick wall" in the semiconductor industry by 2016. Progress can no longer be accomplished by merely scaling transistors to smaller sizes. Nanomagnetic systems provide unique opportunities to continuous advances in device performance and storage capacities since they are inherently non-volatile due to the magnetic order properties.

Combined with advances in semiconductor science and technology, nanomagnetism has resulted in the growing field of spintronics that relies on the use of a new degree of freedom the spin of electron in addition to its electric charge. In the field of spintronics, the influence of the magnetic configuration on polarized current has been studied and led to the discovery of effects such as Giant Magneto-Resistance (GMR) [5] or Tunneling Magneto-Resistance (TMR) [6]. More recently the inverse effect, the spin transfer torque (STT) effect [7], has been demonstrated: spin polarized current can also influence magnetic configurations. Present spintronic devices are complex metal hetero-structures that combine many layers and state-of-the-art lithography [8]. Their basic functionality arises from spin dependent electronic transport of polarized currents by magnetic layers separated by a non-magnetic metallic spacer layer in GMR systems or an insulating spacer in Magnetic Tunnel Junction (MTJ). [9].

In order to study those effects and propose new functionalities one need to be able to manipulate accurately both magnetization and electron spin. For instance the writing process for MRAM is performed by

manipulating magnetization whereas the reading process is performed by measuring the voltage across the device as a current is injected.

While historically, magnetization was manipulated through the application of magnetic fields, there is now many ways to control magnetization at the nanoscale. Indeed magnetization and spin manipulation using excitations such as short-pulse or RF magnetic fields [10], electric fields [11], temperature pulses [12], polarized currents [13] and polarized light [14] are emerging. The low-power manipulation of magnetization, preferably at ultra-short time scales, has become a fundamental challenge with implications for future magnetic information memory and storage technologies. Advances in new magnetic materials and devices could also be crucial for continued progress in computational performance in the face of dramatic increases in power consumption. Low-power spin-based memory and logic devices could complement or supplement traditional semiconductor microelectronics.

Concerning the reading process, which consists of detecting the magnetic configuration using the GMR/TMR effect, very little has been done. The reading process is also an energy-consuming process since an electrical current generator needs to be used to inject a current in the device for voltage measurement. In this work we show how light can be used to replace the electric generator and provide self-powered spintronic devices.

0-2 MOTIVATIONS

The all optical manipulation of magnetic material compatible with spintronic devices using 100 fs polarized laser pulse has been demonstrated in the Nanomagnetism and Spintronic group at the Institut Jean Lamour. [14,15] This new possibility opens new opportunities and all optical manipulation of the magnetization could soon be transferred to the magneto-recording industry. [16] If light can be used to reverse magnetization orientation and thus write information, it is now

interesting to know if it can also be used to read the stored information without any current injection. Several papers have reported the appearance of a voltage in spintronic devices when shined with light. [17,18] Starting from this motivation, we studied the effect of the interaction between light and Magnetic Tunnel Junctions.

0-3 METHODS

For this study, several light sources have been used to study the influence of light on MTJs. MTJ is a complex system with various materials. Each material has its own optical properties. The complexity is further increased by the geometry and design of MTJ. In order to study the influence of light on MTJ, we should be able to distinguish the different materials in the transport study and understand how the geometry of MTJ would affect the transport properties.

For example, with OPO (optical parametric oscillator) laser we have studied the wavelength dependence of photo-voltage by changing the wavelength of laser continuously. The optical properties of materials in a MTJ, e.g. silicon substrate and metals, vary with the wavelength of light. From the wavelength dependence, we can usually have the signature of different materials. For example, the absorption in Silicon is strong in visible range and decreases as the wavelength increases. For metals, the wavelength dependence usually needs to take into account several physical processes, e.g. free-electron effects, interband transitions and plasmons. Moreover, the laser induced signal can be studied in the time domain. Since each physical process has its own characteristic time constant, we can distinguish different physical process using the time resolved signal.

We also used laser setup equipped with translation stage, which is used for mapping the light induced voltage. Given that the laser spot size is small enough, we could determine the characteristic length of laser induced voltage. The experiment is also performed with the presence of external magnetic field. The influence of laser can thus be studied in

different magnetic configurations. Finite element simulations of heat propagation using COMSOL are performed to study the heat propagation in our system. The simulation results are compared with experiment data.

Samples with different geometries, including samples without contact, with one contact and with two contacts between electrode and Si substrate are studied to highlight the importance of contacts between electrode and substrate for the induced photo-voltage. Transport study on samples (DC and AC measurements) with different geometries answers the question of how the geometry of MTJ would affect the transport properties with light. Different parts of MTJ are fully described and simulated using equivalent electric circuits. The experimental results of transport behavior can be well understood in the framework of equivalent circuit.

0-4 OUTLINE OF MANUSCRIPT

This manuscript is divided in five chapters.

The first part is dedicated to the introduction of the physical concepts and to the background knowledge required for the analysis of the experimental results shown in chapter III, IV and V. In Chapter I, the field of spintronics and MTJ devices in particular, will be introduced. Moreover since we are studying the interaction between light and spintronic devices, relevant physical effects such as thermoelectric effects and photovoltaic effects are presented.

In Chapter II, we introduce the experimental aspects of our work: procedure of sample preparation, different measurement approaches and setups are described. After showing how physical vapor deposition (PVD) is used to grow multilayers, we present the vibrating sample magnetometer (VSM) technique which permit to determine the magnetic properties of the multilayers that will be used in the processing of MTJ. The lithography techniques used to pattern the MTJ are also described. In

the second part of this chapter the transport measurement setups developed for this PhD are presented. On these setups the MTJ electrical properties (current, voltage in different geometry) can be measured under controlled laser illumination. We described how we took special care to avoid any additional signal coming from the measurement set up or the environment. A simple example of COMSOL simulation is also shown at the end of Chapter II to give the basics of heat transfer module of COMSOL that will be used to get a numerical solution to the heat equation in the complex MTJ geometry..

In chapter III we present previous results consistence with a giant spin-dependent thermoelectric effect. The thermovoltage in this geometry could reach 1mV. Moreover a magnetothermovoltage effect could be measured with ratio similar to the tunnel magnetoresistance ratio. Those effects could be explained theoretically by the presence of a resonant state at the Fermi level. In order to study and increase this effect we prepared sample with different oxidation times in order to modify the supposed resonant state. We were extremely surprised to measure a voltage of 100mV for a temperature different across the tunnel junction of about 100mK. It led to an unreasonable Seebeck and ZT coefficient. This huge effect could be interesting for self-powered applications. After several tests we found out that when the MTJs were cut to be tested, electrical shortcuts between the Si substrate and the Magnetic Tunnel Junctions appeared. This shortcut that had impact neither on the value of resistance nor on the magnetoresistance, but had a huge effect on the laser induced voltage which could no longer be considered as pure thermovoltage.

In chapter IV we worked on two model MTJs systems, one with and one without well controlled electrical contact between the MTJ electrodes and the Si substrate. By combining static measurements as well as frequency dependence techniques we could model the interaction between light and the devices as an electrical generator and determine its characteristics. We then studied the light wavelength as well as the beam position dependence. Moreover the response of the system after a light pulse helps us to distinguish two origins to the effect. One would be photovoltaic effect between the light and the silicon. The second would be a Seebeck effect due to a temperature gradient in the silicon. For those two phenomena a Schottky barrier at the interface between the substrate and the contact needs to be present.

In Chapter V we present more recent results that show the impact of a perpendicular temperature gradient in some MTJ engineered structure. A voltage develops that originates from the anomalous Nernst effect.

In Conclusion we are summarizing our work and present some prospective.

1-1 SPINTRONICS

In conventional electronics, passive and active devices use and/or manipulate the electric charge of the electrons and ignore the existence of the spin of the electron. However, since the pioneer work of Mott in the thirties [19], it is known that in magnetic materials the scattering probability of electrons is spin-dependent. This effect has been theoretically and experimentally studied in 1970s. It was found that in ferromagnetic 3d metals, the conduction can be understood using a two-current model, and the conductance of the majority spin channel and of the minority spin channel can be different by more than a factor of ten [20].

As an extension, the spin should play a role in electronics if magnetic materials are inserted in electronic devices. This idea was limited by technological aspects, especially the deposition of multilayers with controlled thicknesses and roughnesses at atomic scale. The technological limitations have been solved by adapting molecular beam epitaxy (MBE) to metal materials or reducing the flux of deposition and improving vacuum in other techniques like sputtering.

Associating nanometer thick Fe magnetic thin films with non-magnetic Cr thin films in multilayer structures made by MBE, P. Grünberg et al [21] and A. Fert et al [5] discovered the Giant Magneto Resistance (GMR) effect in 1988. The explanation of the effect has been given on the basis of the two-current model developed in 1970 and on the fact that the spin of the electron is conserved when it propagates through the non-magnetic layer (need for thin layers). The spin-polarized electrons in each channel will experience different scattering potentials in the different magnetic states. As depicted in Fig. 1-1, in antiparallel configuration, both spin-polarized channels will experience scattering evens while in the case of parallel configuration, only one channel is scattered. It turns out that changing the configuration of the magnetic layers changes the measured electrical resistance. The importance of this discovery is self-evident: the magnetoresistance ratio reached 100% in the first publications [22] while the value of anisotropic magnetoresistance did not exceed a few percent, and therefore such

effect was depicted as “giant”. The Nobel Prize in Physics 2007 was awarded jointly to Albert Fert and Peter Grünberg "for the discovery of Giant Magnetoresistance".

The discovery of GMR effect marked the birth of spintronics, which literally means the combination of spin degree of freedom into more traditional electronics. The role of the spin of the electrons has then become a field of high interest for fundamental research as well as for the development of new electronic devices. The combined used of both the charge and the spin of electrons provided new phenomena, new capabilities and functionalities [23]. GMR was shown in multilayers made by other deposition techniques, especially using sputtering that extended the possibilities of industrial applications. Other materials have been tested like copper for the non-magnetic spacer material because of its high spin diffusion length preserving the spin polarization over nanometers [24]. The spin-valve emerged with the development of exchange biased hard layers [25] and nowadays, everybody has already used a spintronic device. Indeed, the read heads of the hard drives use the GMR phenomenon. More details on the GMR effect can be found in reference [26].

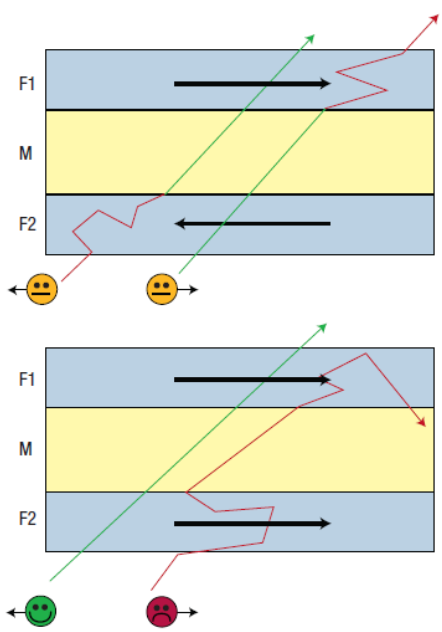

Figure 1 - 1: Schematic representation of scattering process in GMR film. *The trilayer consists of two FM layers F1 and F2 separated by a non-magnetic metal spacer layer M. In P configuration (lower panel), the spin-up electrons (spin parallel to the magnetization) can travel through the sandwich nearly unscattered, providing a conductivity shortcut and a low resistance. On the contrary, in the AP configuration (upper panel) both spin-up and spin-down electrons need to go through strong scattering in either F1 or F2, giving rise to a higher overall resistance. [1]*

By replacing the metal spacer by an insulator, another important class of spintronics device is obtained: Magnetic Tunnel Junctions. In this structure, two ferromagnetic layers are separated by a thin electrical insulating layer. Through the application of a voltage across the junction, the electrons are forced to tunnel through the insulating layer, from one ferromagnetic layer to the other. Once again, the resistance of the device will depend on the relative orientation of the magnetizations of the magnetic layers in contact with the tunnel barrier. In the following, we will briefly review the basis of this field. More details can be found in [27]. The first report about MTJ dated back to 1975 by Julière [6] and the community did not pay too much attention because the effect was very small and measured at low temperature. Once again, the control of the growth of thin insulating layer was the bottleneck to the development of this activity. In 1995, Moodera et al [28] was the first to show a relative variation of resistance of more than 10% at room temperature using alumina oxide tunnel barriers. This lunched a strong activity in this field.

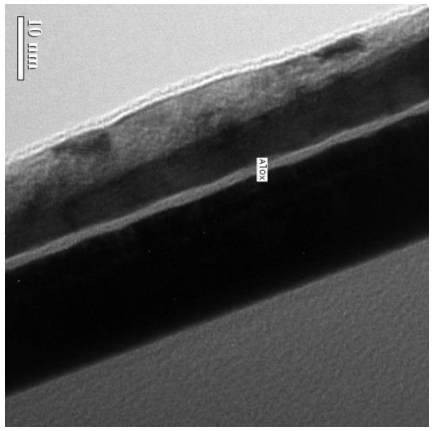

Figure 1 - 2: TEM image of an Al_2O_3 MTJ made in the framework of the PhD.

Jullière's model was based on the concept of spin polarization at the Fermi level defined as:

$$P_i = \frac{N_{M,i} - N_{m,i}}{N_{M,i} + N_{m,i}},$$

where $N_{M,i}$ and $N_{m,i}$ are the densities of state the electrode number i for the spin majory and spin minority electrons respectively.

As for GMR, the basic hypothesis consists to consider two conduction channels each associated to a spin direction, the spin being conserved in the tunneling process. Thanks to the Fermi golden rule and considering low applied voltages and low temperatures, the conductance for each spin channel is proportional to the product of the density of states on either side of the barrier. The conductance is then the sum of the conductance of the two spin channels and is different in the parallel and antiparallel configurations. As shown in Fig. 1-3 where simplified band structures of the ferromagnetic electrodes are sketched, the total conduction can be expressed as:

$G_P = N_{M1}N_{M2} + N_{m1}N_{m2}$ for parallel configuration,

$G_{AP} = N_{M1}N_{m2} + N_{m1}N_{M2}$ for the antiparallel configuration.

The tunnel magnetoresistance is then defined by:

$$TMR = \frac{R_{AP} - R_P}{R_P} = \frac{G_P - G_{AP}}{G_{AP}} = \frac{2P_1P_2}{1 - P_1P_2}.$$

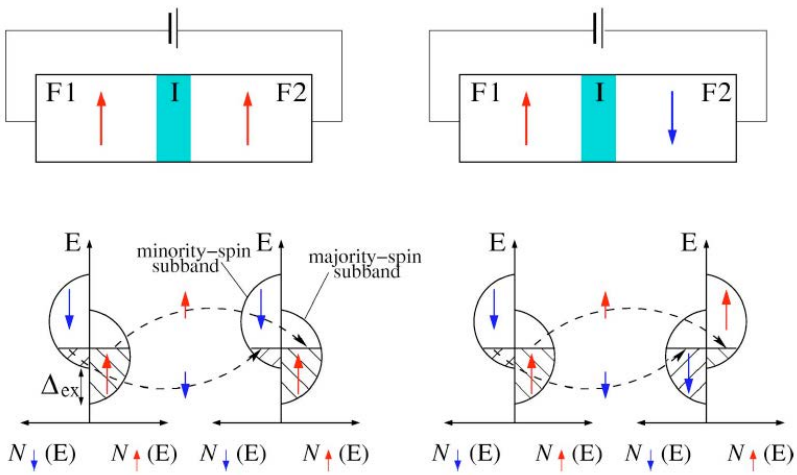

Figure 1 - 3: Tunneling process in the magnetic tunnel junction. *The upper part shows the schematic representation of MTJ in the parallel magnetizations configuration (left) and the antiparallel magnetizations configuration (right). Bottom: schematic of the density of states of electrode 1 and electrode 2 in the parallel magnetizations configuration (left) and the antiparallel magnetizations configuration (right). [9]*

Using the spin polarization measured on different ferromagnetic materials, TMR exceeding 70% were expected. This perspective of high magnetoresistance combined with low current consumption thanks to the use of an insulator, and high spatial integration thanks to the out-of-plane configuration led to an intense research activity and the development of new materials, more accurate theories, new predictions and new related effects.

First of all, Slonczewski proposed in an analytical model that the tunnel polarization depends on the ferromagnetic/insulator couple. [29] Using numerical computations, Montaigne et al showed that, based on the free electron, the main trends of the Al_2O_3 tunnel barriers could be reproduced. [30] Improving the quality of the Al_2O_3 tunnel barrier, the TMR value could be increased and 70% of TMR has effectively been reached by Wang et al [31] using CoFeB electrodes after thermal annealing.

Theoretical developments taking into account the symmetry of the electron Bloch wave functions in the electrodes and the symmetry dependent attenuation length in the insulator made by W.H. Butler et al. [32,33]. J. Mathon et al [34] predicted more than 1000% of TMR in Fe(100)/MgO(100)/Fe(100) epitaxial tunnel barriers. Several years later, 200% of TMR at room temperature were reported by Yuasa et al [35] and Parkin et al [36]. In comparison to amorphous alumina oxide tunnel barrier, the attenuation length in MgO(100) is strongly symmetry dependent reinforcing the weight of the 100% polarization of the Δ1 state in the Fe(100) electrode (Fig. 1-4).

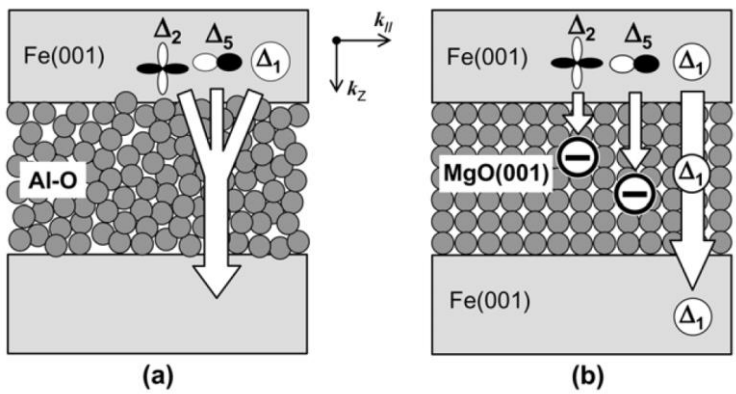

Figure 1 - 4: Schematic illustrations of electron tunneling. *Tunneling process through (a) an amorphous Al–O barrier and (b) a crystalline MgO(001) barrier are different. [37]*

The physics of MgO(100) tunnel barrier appears to be more rich and, with 600% of TMR at room temperature, is more interesting for applications. Therefore, quite all the studies have focused on this material. The TMR appears to oscillate with the MgO tunnel barrier [38], an interlayer exchange coupling mediated by tunneling electrons has been shown [39]. The existence of surface states and their impact on the tunnel transport has been shown [40] and Cr can act as an insulator in (100)Fe/Cr/Fe/MgO/Fe multilayers that also gave an experimental proof the impact of symmetries in such systems [41]. On one hand, physics is richer but on the hand, the tunnel characteristics are often difficult to interpret especially the variations as a function of temperature or applied

bias voltage. For additional information on MgO(100) tunnel barrier, the reader can refer to the review article [37].

Nowadays, the magnetic tunnel junction technology appears to be a mature technology to be used in applications. High variation of resistance, low power consumption, high integration are many assets than can be used in magnetic sensors, electronic devices, oscillators etc… While Magnetic tunnel junctions are widely used as read-head in modern hard disk technology, one emblematic electronic system is the magnetic random access memory (MRAM). MRAM is composed by an array of magnetic tunnel junctions (Fig. 1-5) and each MTJ stores a bit of information. The state is coded by its resistance, for example '0' for the parallel state of magnetization and '1' for the antiparallel state. Bigger is the difference of resistance, easier is the reading of the stored information. To measure one bit, a difference of resistance is measured between the bit and word line connecting the MTJ to be read. To write information, the magnetic state of the MTJ has to be changed.

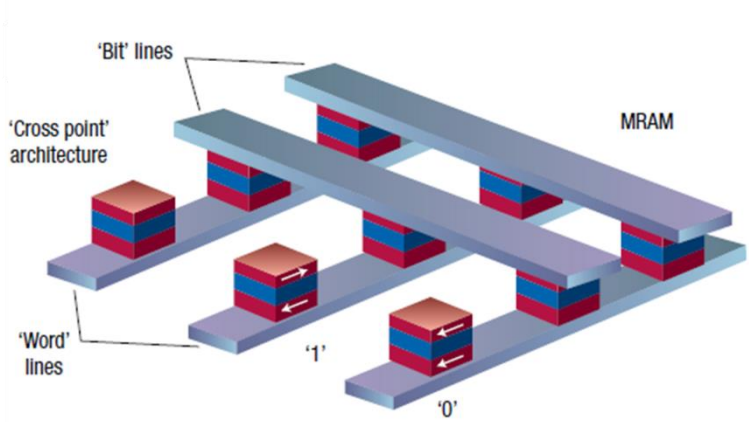

Figure 1 - 5: Structure of magnetic random access memory. *MRAM is an array of MTJs. Each MTJ can be accessed with the address given by 'bit' line and 'word' line. The magnetic configuration of ferromagnetic layers, AP and P correspond to '1' and '0', respectively. [1]*

While local magnetic fields applied using the bit and word lines have been used in the beginning, the spin transfer torque (STT) effect [7,42] has been chosen to reduce the cross talk in high density MRAMs. The use of high current densities limits the number of writings because of the aging of the nm thick insulator. Recently, other writing schemes are actually under study. Spin-orbit torques (SOT) can be used to switch magnetization without current flowing across the tunnel barrier [13,43–46].

Heat and temperature gradient can also be used to manipulate magnetization. Indeed temperature gradients in magnetic nanostructures can give rise to the generation of pure spin current. Following the well-known Seebeck effect [47], new phenomenon named Spin Seebeck Effect have been recently studied [48]. The created currents from a temperature gradient can lead to magnetization reversal of single domain particles [49] or domain wall motion along a wire [50,51]. Other literature are showing that heat and generated current may be used in spintronic devices [52–54]. It is also to possible to combine local heat and spin torque to reduce the current needed to switch the magnetization. [55]

Moreover it has recently been shown that magnetization could be reversed using a polarized light coming from a femtosecond pulse laser [15,16] even for ferromagnetic materials used in spintronic devices [14]. In this case, laser pulse transfers both heat and angular momentum. Even if the microscopic origin of the phenomena is still under heavy discussion those result open the possibility to manipulate magnetization and consequently to *write* information in magnetic memories using light.

In this thesis we will concentrate on the possibility to use light to probe the magnetic configuration inside spintronic devices and so to *read* the information.

1-2 THERMOELECTRIC/THERMOMAGNETIC EFFECT

In this section, the two thermoelectric/thermomagnetic effects relevant to this thesis are described.

Seebeck effect

Named after the German-Estonian physicist Thomas Johann Seebeck, it describes the phenomenon of the electric current generation from a thermal gradient. (See for instance [56]) In absence of magnetic field, the electric current density $\boldsymbol{j}$ can be expressed as:

$$j_i = \sigma_{ik} E_k - \sigma_{ik} \alpha_{km} \frac{\partial T}{\partial x_m}.$$

In this equation, called the generalized Ohm's law, j_i is the i^{th} component of electric current density, σ_{ik} are the components of the electric conductivity tensor, E_k is the k^{th} component of the electric field. Compared to the traditional Ohm's law, an additional tensor appears whose components are noted as α_{km} and called Seebeck coefficients. These coefficients are prefactors of $\frac{\partial T}{\partial x_m}$: the components of the thermal gradient.

In the isotropic case, the tensors described by σ_{ik} and α_{km} components becomes respectively a scalar σ and a scalar α.

For open circuit geometry ($\boldsymbol{j} = 0$) shown in Fig. 1-6 we have:

$$\boldsymbol{E} = \alpha \boldsymbol{\nabla T},$$

while in the isotropic case of close circuit ($\boldsymbol{E} = \boldsymbol{0}$) also shown in Fig. 1-6, we have:

$$\boldsymbol{j}/_{\sigma} = -\alpha \boldsymbol{\nabla T},$$

where σ and α are respectively the conductivity and the Seebeck coefficients.

Moreover, considering a unitary section we can integrate the previous expression along the normal direction. This leads to:

$$I = G_V \Delta V + G_T \Delta T,$$

where I is the current per surface unit, $G_V \propto \sigma$ and $G_T \propto \sigma\alpha$.

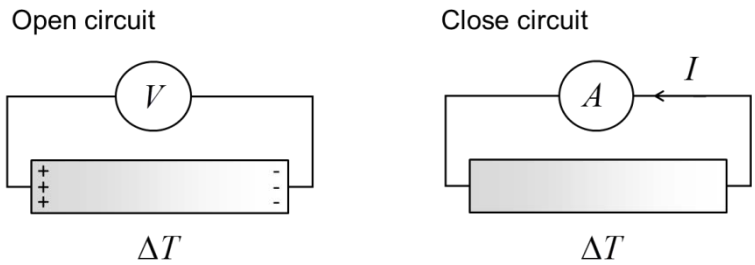

Figure 1 - 6: Seebeck effect in an open and a close circuit. *A temperature gradient generates voltage or a current in open circuit and close circuit, respectively. Charges accumulate at the hot and cold ends in the open circuit geometry.*

The Seebeck effect is often regarded as one potential way to provide clean energy. Up to now the generation of electricity from Seebeck effect is still at an insignificant position compared to energy generation from fossil sources. However, it has been used in some special circumstances, for instance to provide energy for satellites and other space probes. [57] The main reason of this confined development lies in the conversion efficiency which is still too low to be competitive in practical application. [58]

Nernst-Ettingshausen effect (often shortened as Nernst effect)

In presence of a magnetic field $\boldsymbol{B}$ the generalized Ohm's law can be rewritten at the first order in $\boldsymbol{B}$ as:

$$\boldsymbol{E} = {}^{\boldsymbol{j}}/_{\tilde{\sigma}} + \tilde{\alpha}\boldsymbol{\nabla T} + R_H \boldsymbol{B} \times \boldsymbol{j} + Q^{\perp} \boldsymbol{B} \times \boldsymbol{\nabla T},$$

where R_H is the Hall coefficient and $Q^{\perp}$ the Nernst-Ettingshausen coefficient in reference to Walther Nernst and Albert von Ettingshausen [59]. The notation $\tilde{\sigma}$ and $\tilde{\alpha}$ correspond to the conductivity and Seebeck tensors respectively.

From the last term of this equation we can see that the simultaneous presence of a thermal gradient and a magnetic field can lead to the appearance of an electrical field: this is the phenomenology of the Nernst-Ettingshausen effect. Here we can note the similarity (when

swapping $\boldsymbol{j}$ and $\boldsymbol{\nabla T}$) between the term responsible for the Hall effect: $R_H \boldsymbol{B} \times \boldsymbol{j}$ and the term responsible for the Nernst effect: $Q^{\perp} \boldsymbol{B} \times \boldsymbol{\nabla T}$.

In the case of a ferromagnetic conductor in an open circuit ($\boldsymbol{j} = 0$) and in absence of external magnetic field we can defined the planar Nernst coefficient α_z and the anomalous Nernst-Ettingshausen coefficient $Q_{AN}^{\perp}$ by analogy with the definition of the both AMR (anisotropy of magnetoresistance) and anomalous Hall effect. [60] This leads to the following equation:

$$\boldsymbol{E} = \alpha \boldsymbol{\nabla T} + (\alpha_z - \alpha)(\boldsymbol{\nabla T} \cdot \boldsymbol{m}) \cdot \boldsymbol{m} + Q_{AN}^{\perp} \boldsymbol{m} \times \boldsymbol{\nabla T},$$

where $\boldsymbol{m}$ the normalized magnetization vector.

1-3 PHOTOVOLTAIC EFFECT

Photovoltaic effect is a direct conversion from sunlight into electricity in a energy point of view. Compare to fossil energy, it has been seen as a sustainable clean energy. The capacity of photovoltaic power is expanding fast in recent years. For example at the end of 2012, photovoltaic capacity in Germany contributed 4.6% of their annual gross electricity generation. [61]

At present, fossil fuels are the primary energy source in the world. They are formed by nature through complex processes in a time scale of millions of years. Fossil fuels are known to be non-renewable because the consumption rate is much higher than the rate of production by nature. In addition to the limited viable reserves, the consumption of fossil fuels raises serious environmental concerns. The two problems are overcome for the photovoltaic power. Solar source has a vast potential in the planet, especially in regions with high isolation like Africa or India.

In the following, we present the mechanism of photovoltaic effect in p-n junction and Schottky junction. The transport properties and the optical properties are also discussed.

Mechanism

The photovoltaic effect is the creation of voltage or electric current in a material upon exposure to light. When the sunlight or any other light is incident upon the surface of semiconductor, the electrons present in the valence band absorb energy and, being excited, jump to the conduction band and become free. These highly excited non-thermal electrons diffuse, and some of them reach a junction where they are accelerated into a different material by a built-in potential (Galvani potential). This generates an electromotive force, and thus part of the light energy is converted into electric energy. In most photovoltaic applications the radiation is sunlight, and the devices are called solar cells. As shown in Fig. 1-7 in the case of a p-n junction solar cell, illuminating the material creates an electric current as excited electrons and the remaining holes are swept in different directions by the built-in electric field of the depletion region.

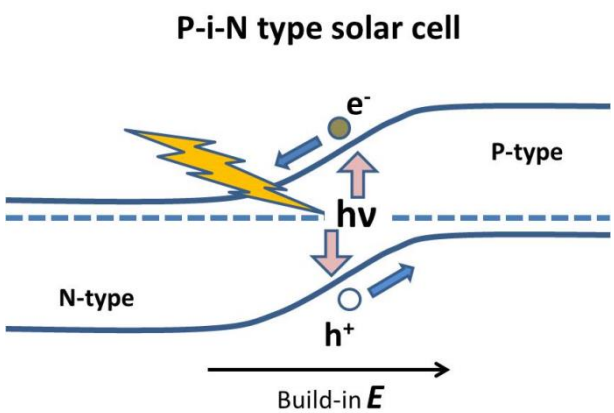

Figure 1 - 7: Principle of photovoltaic device with p-n junction. *Electrons and holes generated due to the absorption of photons are separated from each other in the build-in electric field.*

In our study, we have employed Schottky junction type of solar cells as the source of photocurrent. Solar cells of this type have a long history, dating back to 1883, when Charles Fritts coated selenium with a thin layer of gold to make one of the world's first solar cells. However, since

then, they have commanded only a small amount of attention from researchers and corporations due to their inherent low output voltage compared with p-n junction or hetero-junction type of solar cell. No popular solar-cell design uses metals in the active region, other than for contacts. Nevertheless, in the past decade or two, university research and an industrial pilot production line have demonstrated the potential commercial viability of one particular Schottky junction solar cell design, the silicon "MIS-IL solar cell" (metal-insulator-semiconductor inversion-layer), and moreover they continue to be used fairly commonly in a lab setting due to their simple architecture. [62]

Background on Schottky barriers

As shown in Fig. 1-8, an interface between a metal and semiconductor can induce a depletion or inversion layer in the semiconductor. A built-in potential called the "Schottky barrier" appears between the bulk of the semiconductor and the surface. The magnitude of the potential is called the "Schottky barrier height" (SBH, Φ_B). For a perfect abrupt junction between the metal and semiconductor, the Schottky-Mott model [63] gives the SBH in terms of the electron affinity of the semiconductor (Φ_S), the work-function of the metal (Φ_M), and the band gap (E_g). For a p-type semiconductor, $\Phi_B = E_g + \Phi_S - \Phi_M$, while for an n-type semiconductor, $\Phi_B = \Phi_M - \Phi_S$. In reality, however, the SBH is not well described by the Schottky-Mott model because of interface states and defects.

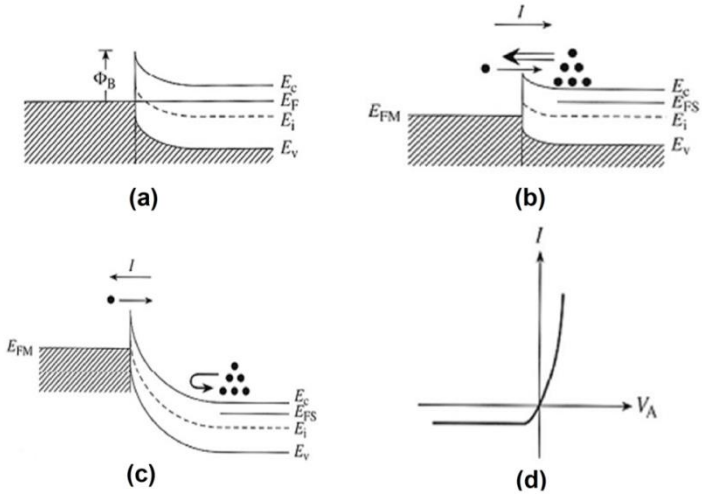

Figure 1 - 8: The behavior of SB at different bias voltage. *(a) Band structure of Schottky contact for metal/n-type semiconductor. (b) Schottky junction at forward bias condition. (b) Schottky junction at reverse bias condition. (d) Typical IV curve for Schottky diode. [63]*

IV characteristics of Schottky diodes

A forward bias will reduce the barrier height unbalancing the electron current flow, resulting in a huge forward current that increases exponentially with applied voltage (Fig. 1-8b). At reversed bias, the current (majority carriers moving from the metal to the semiconductor) is dominated by Schottky-Richardson emission (also called "Thermionic emission"). Here, the carriers in the metal randomly have enough energy to pass over the barrier height. The magnitude of this current is reasonably constant with respect to applied voltage, since the energy barrier from the metal to the semiconductor is reasonably constant, unlike the energy barrier from the semiconductor to the metal, which reduces markedly in forward bias. The typical IV curves for Schottky diode is schematically shown in Fig.1-8d).

The IV character of a Schottky contact can be formularized as following:

$$I = I_S \left[exp\left(\frac{qV_A}{kT}\right) - 1 \right],$$

where $I_S = AA^*T^2\exp(-\Phi_B/kT)$, $A^* = 4\pi qm^*k^2/h^3 = 120[A/cm^2K]$, where Φ_B is Schottky barrier height, V_A is applied voltage, A is area, and A^* is Richardson's constant.

Effect of light on solar-cell

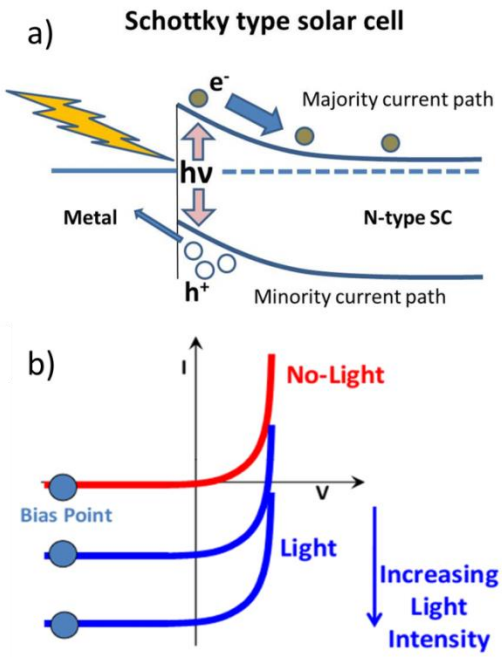

Figure 1 - 9: The transport behavior of SB in the presence of light. *(a) Scheme of majority and minority current paths. (b) The change of IV curve of the Schottky diode with light.*

When shining of light on the surface of Schottky contact, if the photon energy (hν) is larger than the band gap of semiconductor, one photon can generate one electron-hole pair in the depletion layer region. With the sweeping of electric field in depletion layer, the generated carriers will flow in the circuit and create photocurrent. Across the MS barrier, there are two types of current paths between the metal and the semiconductor: "minority carrier current path" and "majority carrier current path", as

shown in Fig.1-9a). The two paths is asymmetric because that the electric field drives the minority carriers towards the barrier, where they can pile up to a certain degree while waiting to tunnel through. The majority carriers, on the other hand, are being driven away from the interface by the electric field. So slowing the passage of minority carrier can dramatically reduce the net photocurrent flow.

Summed up the majority and minority current paths, we get a general formula for the behavior of Schottky diode with light as following:

$$I_{total} = I_{dark} + I_{due\ to\ light},$$

$$I_{total} = I_0\left(e^{\frac{qV_A}{kT}} - 1\right) + (-qA)WG_L,$$

where the saturation current $I_0 = I_{0,minority} + I_{0,majority}$. W is the width of depletion layer. G_L is electron-hole pair generating rate which is proportional to the power of light and depends on the wavelength of light and semiconductor materials (see below). We show the typical IV curves of Schottky diode with light in Fig. 1-9b). The photocurrent density is initially linear with the illumination intensity, but it saturate at strong intensity of light because of the slow evacuation rate of minority carriers at the interface.

In open circuit case, the continuous creating electron-hole pairs will result in an accumulation of carriers at both sides of semiconductor, and generate a forward bias. This forward bias will enhance the diffusion current from semiconductor to metal. In the end, the diffusion current and photocurrent are balanced to produce a net zero current in the circuit.

Note that the above mentioned is a somewhat a simplified picture. The full electrostatics of the MS system, including image-charge lowering [64], field emission [64], interface-state dynamics, and so forth, means it does not satisfy the classic diode equation, but rather can have large ideality factors, non-saturating reverse current, and other complications. [65,66]

Solar-cell absorption efficiency *vs.* wavelength, and materials

The absorption coefficient determines how far into a material light of a particular wavelength can penetrate before it is absorbed. Semiconductor materials have a sharp edge in their absorption coefficient, since light which has energy below the band gap does not have sufficient energy to

excite an electron into the conduction band from the valence band. Consequently this light is not absorbed. The absorption coefficient for several semiconductor materials is shown in Fig.1-10.

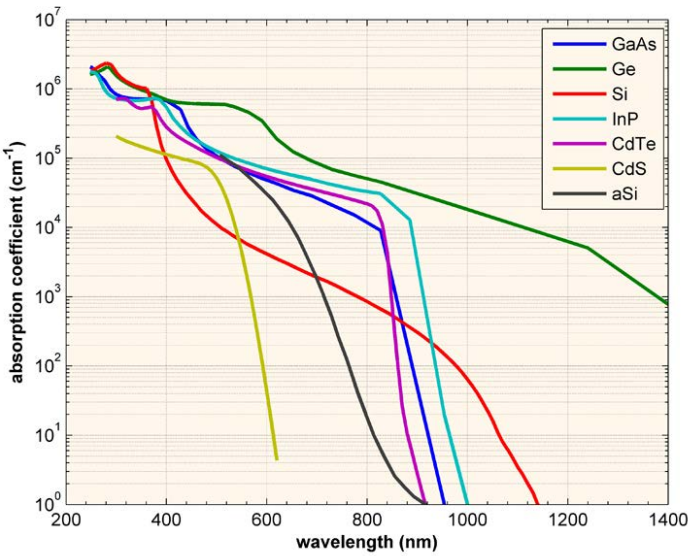

Figure 1 - 10: The absorption coefficient α of several semiconductors. *The absorption coefficients at 300K are plotted as as a function of the vacuum wavelength of light. [67]*

The above graph shows that even for those photons which have energy above the band gap, the absorption coefficient is not constant, but still depends strongly on wavelength. The probability of absorbing a photon depends on the likelihood of having a photon and an electron interact in such a way as to move from one energy band to another. For photons which have energy very close to that of the band gap, the absorption is relatively low since only those electrons directly at the valence band edge can interact with the photon to cause absorption. As the photon energy increases, a larger number of electrons can interact with the photon and result in the increase of absorption coefficient. From Fig.1-10, we can see the Si absorption band edge is at about 1200nm. We have used this character to study our light powered MTJ with different wavelength illumination to distinguish the contribution of photovoltaic effect.

The absorption coefficient, α, is related to the extinction coefficient, k, by the following formula: $\alpha=4\pi k/\lambda$, where λ is the wavelength. (If λ is in nm, multiply by 10^7 to get the absorption coefficient in units of cm^{-1}.) The relationship means that different wavelengths penetrate different distances into a semiconductor before most of the light is absorbed. The absorption depth is given by the inverse of the absorption coefficient α^{-1}, and it is a useful parameter which gives the distance into the material at which the light drops to about 36% of its original intensity (a factor of $1/e$). Since high energy light (short wavelength), such as blue light, has a large absorption coefficient, it is absorbed in a short distance (for silicon solar cells within a few microns) of the surface, while red light (lower energy, longer wavelength) is absorbed less strongly. Even after a few hundred microns, not all the red light is absorbed in silicon. Fig.1-11 gives the absorption depth of different semiconductor as a function of wavelength.

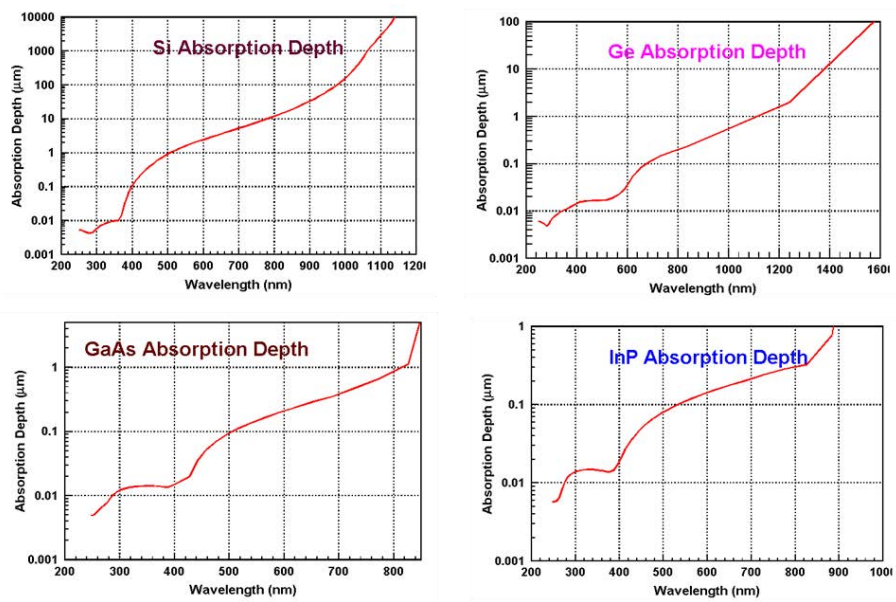

Figure 1 - 11: The absorption depth of several semiconductors.
The absorption depth at 300K are plotted as as a function of the vacuum wavelength of light. [67]

Besides the direct excitation of free electrons, a photovoltaic effect can also arise simply due to the heating caused by absorption of the light. The heating leads to an increase in temperature, which is accompanied by temperature gradients. These thermal gradients in turn may generate a voltage through the Seebeck effect. Whether direct excitation or thermal effects dominate the photovoltaic effect will depend on many material parameters. In our study, we have found the two effects both play role to create photocurrent.

Advantages and disadvantages

The goal of this thesis is to employ the light generated photocurrent to power on MRAM device. The efficiency of the light generated power should be essential issue to be considered. In our study, Schottky type solar cell is used. However, it still needs to be improved for the architecture to enhance the absorption efficiency. Compared to p-n solar cell, Schottky solar cell has advantages and disadvantages as below.

Advantages:

1. Cheap cost. Schottky contacts is easy to form in some cases and the Schottky cell eliminates the top-surface, oppositely doped collector layer;
2. Because the turn-off time of device is limited by minority carrier lifetime, Schottky diodes have little minority carrier stored charge and thus have application in fast switching applications (solar invertors, motors, etc…). On the other hand, Minority carrier charge storage in p-n junctions tends to limit the switching times of p-n junction diodes. We have taken advantage of this point to make a time-solved study on the light powered MTJ;
3. Collecting junction is optimally placed at the surface of the solar cell where most of the generation occurs.

Disadvantages:

1. Inherently low output voltage Voc
2. Full metal coverage creates reflection issues. The absorption of light by the metal layer is very strong. It is necessary to attach a metal grid on top of surface, however this reintroduces shading effects and higher costs.
3. Generally higher leakage currents in Schottky contacts
4. Generally lower breakdown voltages imply higher shunting of the junctions

1-4 THERMOELECTRIC EFFECTS IN SPINTRONICS

Heat has attracted a lot interest in the magnetic society in the past few years. Heat could help to lower the energy gap for magnetic recording [68], and heat could induce spin current/spin accumulation in magnetic systems. Heat is regarded as a new approach to manipulate the spin system. Combining the heat and spin degree of freedom, a number of nouveau effects, e.g. spin-dependent Seebeck effect, spin-dependent Peltier effect, spin Seebeck effect, have been discovered or at least predicted. Following the classification of Bauer [69], reported effects can be classified into two categories depending whether spin accumulation exists or not. Magneto-Seebeck corresponds to the thermoelectric effect without any spin accumulation in magnetic systems. [17,18,70] The other category involves the participation of spin current, such as spin Seebeck effect [48,71,72] and thermal spin transfer torque. [52,73]

In the following, the interaction between heat current and electric current is presented in the framework of magneto-Seebeck effect (no spin accumulation). Following the two-current model [20], the electric current consists of two spin-polarized currents. The conventional thermoelectric effect can be extended by taking into account the two spin-polarized currents. Note that the heat current will be taken as spin-unpolarized, although the opposite scenario has been proposed and studied. [74,75]

Electrons move under electric field and electric current density J is defined to be:

$$J = \sigma E = \sigma \nabla \mu / e,$$

where E is the electrical field, μ the electrochemical potential and σ the electric conductivity. Similarly the heat current Q under a temperature gradient ∇T is defined as:

$$Q = \kappa \nabla T,$$

where κ is the thermal conductivity. Thermoelectric effects are results of coupling the the two currents. If we take the thermoelectric effect into consideration, the electric current J and thermal current Q can be expressed as:

$$\begin{pmatrix} J \\ Q \end{pmatrix} = \sigma \begin{pmatrix} 1 & ST \\ ST & \kappa T/\sigma \end{pmatrix} \begin{pmatrix} \nabla\mu/e \\ -\nabla T/T \end{pmatrix},$$

in which S is the Seebeck coefficient or thermoelectric power and ST is also called as Peltier coefficient. Seebeck effect describes the electrical current due to temperature gradient while Peltier coffient describes the inverse effect. Note the symmetric coefficient matrix is a natural outcome of Onsager reciprocal relation.

Conventional thermoelectric matrix can be naturally extended within the framework of two-current model to incorporate the spin degree of freedom. [69] In isotropic and monodomain metallic ferromagnet electrons go through two spin channels and total electron conductivity can be expressed as: $\sigma = \sigma^{(\uparrow)} + \sigma^{(\downarrow)}$, where $\sigma^{\uparrow}$ and $\sigma^{\downarrow}$ are spin-dependent conductivities and Seebeck coefficient $S = (\sigma^{(\uparrow)}S^{(\uparrow)} + \sigma^{(\downarrow)}S^{(\downarrow)})/(\sigma^{(\uparrow)} + \sigma^{(\downarrow)})$. The charge current J_C, the spin current J_S and heat current Q are given as:

$$\begin{pmatrix} J_C \\ J_S \\ Q \end{pmatrix} = \sigma \begin{pmatrix} 1 & P & ST \\ P & 1 & P'ST \\ ST & P'ST & \kappa T/\sigma \end{pmatrix} \begin{pmatrix} \nabla\mu_C/e \\ \nabla\mu_S/2e \\ -\nabla T/T \end{pmatrix},$$

in which $\mu_C = (\mu_\uparrow + \mu_\downarrow)/2$, $\mu_S = (\mu_\uparrow - \mu_\downarrow)/2$, and $\mu_\uparrow$ and $\mu_\downarrow$ stand for the electrochemical potential for spin up and spin down, respectively, and P and P' stand for the spin-polarization of conductivity and its energy derivative:

$$P = \left.\frac{\sigma^{\uparrow} - \sigma^{\downarrow}}{\sigma}\right|_{\epsilon_F}; P' = \left.\frac{\partial(P\sigma)}{\partial\epsilon}\right|_{\epsilon_F}.$$

The matrix reveals the interaction between spin current and heat current: spin current J_S can be induced by temperature gradient, namely spin-dependent Seebeck effect, and heat current Q can be induced by spin accumulation, namely spin-dependent Peltier effect. Both coeffients are given to be $\sigma P'ST$.

There were a lot effort concerning the impact of heat in more complex systems, such as spin valve structure and MTJ.

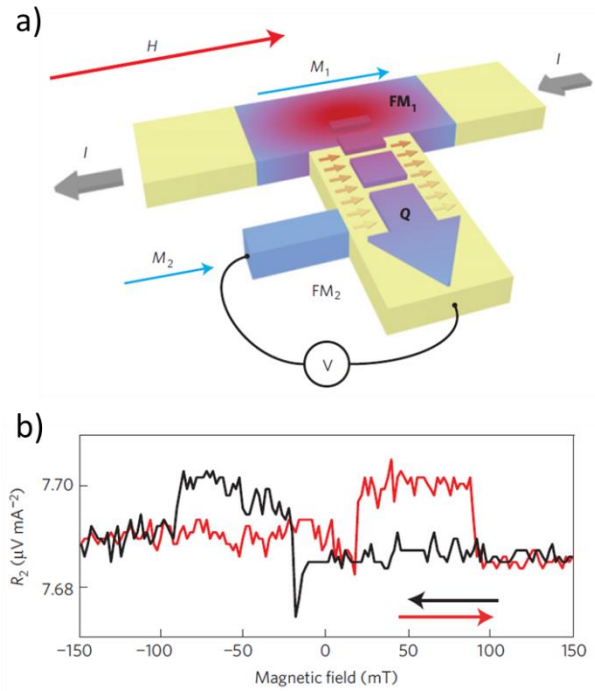

Figure 1 - 12: Conceptual diagram for Seebeck spin injection from FM to NM material. *Joule heating in FM1 creates a heat current Q into the non-magnetic material. Spin injected by the heat current is probed using another ferromagnet FM2. Spin signal is detected using lock-in technique at second harmonic because heat gradient ΔT scales with I2. [53]*

In spin valve structures, the Seebeck effect for Fe/Cr superlattice system was reported. [76,77] More recently, spin injected by heat current is shown by the detection of spin dependent Seebeck voltage. Similar scenario is also presented in the experiment of Seebeck tunneling from FM to silicon. [52]

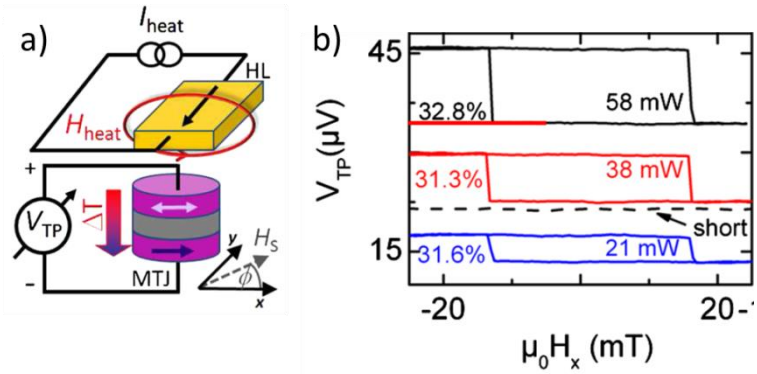

Figure 1 - 13: Measurement of Seebeck effect in MgO MTJ. *a) Sketch of measurement setup. A current I heat through the HL creates a temperature gradient in the stack and the Seebeck voltage is measured in in-plane magnetic field. b) Easy axis Seebeck voltage versus magnetic field under heating powers of 21mW (blue), 37.8mW (red), and 58.05mW (black). [70]*

In MTJ systems where the transport property is largely determined by the thin insulation layer, the Seebeck also reported for MgO systems. A few publications about Seebeck effect in the MTJ structure were published in the past few years. [17,18,70,78,79] Experimentally in reported studies, temperature gradient is either applied by a resistance heater or laser. Fig. 1-13 shows the Seebeck effect in MgO based MTJ with temperature gradient applied using electrical heating. The advantage for resistance heater is that measurement setup is largely simplified since no external setup is needed to give rise to the temperature gradient in the sample. Laser is convenient in sample processing and easily adapted for the lock-in measurement (AC modulated with light chopper or AC electric source). Fig. 1-14 shows the Seebeck voltage measured with laser heating modulated with optical chopper.

Concerning the MgO MTJ, Generally speaking, the Seebeck effect in MTJ structures is similar to the counterpart in classical Seebeck effect in non-magnetic systems. Seebeck effect is greatly decided by the slope of DOS near the Fermi level. For example, Czerner et al showed that the interfacial atomic termination has a strong influence on the magneto-Seebeck effect. [80]

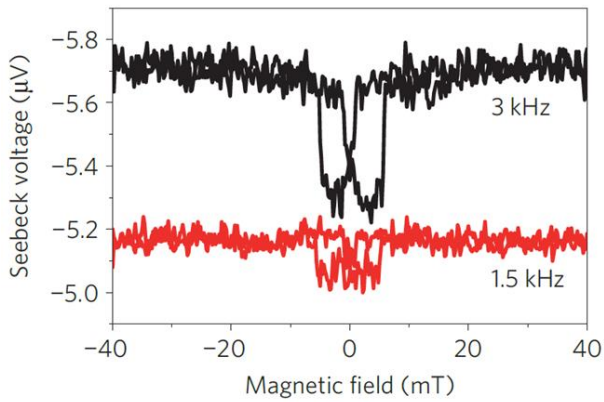

Figure 1 - 14: Seebeck voltages for MgO MTJ under laser heating. *Seebeck voltage is shown as a function of magnetic field for 1.5 and 3 kHz lock-in modulation. [18]*

The transport property of MTJ is largely determined by the interface. Similarly the interfacial states are viewed as important factor in Seebeck of MTJ structure. Interfacial engineering, such as insertion layer, could be a feasible way to increase the magneto-Seebeck coefficient.

In the Al_2O_3 based MTJ, our group reported Seebeck voltage as high as 1mV. [17] Fig. 1-15c) shows the light induced voltage and current as a function of external magnetic field. The temperature gradient is applied using laser diode. The laser induced voltage depends on the magnetic configuration while the laser induced current is independent of the magnetic configuration. Interfacial resonant state is proposed to explain the reported giant voltage in Al_2O_3 structures.

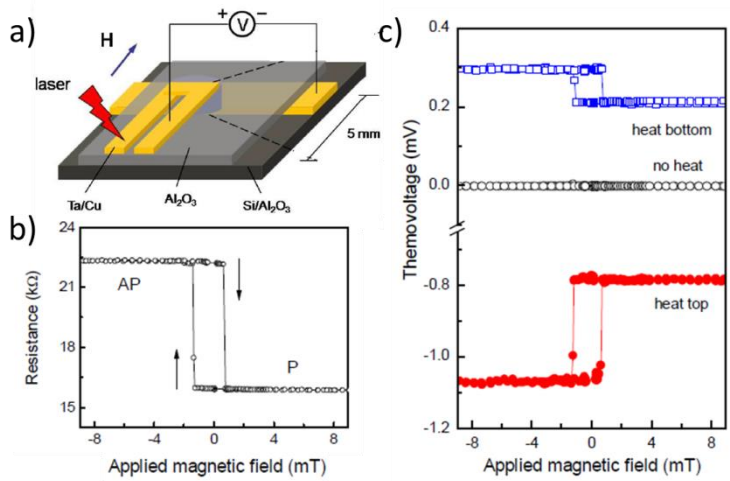

Figure 1 - 15: Light induced voltage on AlOx MTJ. *a) Sketch of measurement on AlOx MTJ: Voltage between top electrode and bottom electrode while laser shines at bottom or top electrode. b) Resistance as a function of magnetic field. c) Measured voltage as a function of magnetic field while heats shines at bottom electrode (blue), and top electrode (red). [17]*

1-5 SUMMARY

In this chapter, we briefly reviewed the field of spintronics and two effects related to the thesis, thermoelectric effects and photovoltaic effect. Indeed, great progresses have been made in the field of spintronics since the discovery of GMR effect. At present, the physical understanding of conventional spintronic phenomenon, such as GMR or TMR, is more or less complete. Many interesting effects are emerging with the introduction of new concepts. One example is the magneto-Seebeck effect observed in magnetic tunnel junctions with applied temperature gradient. The observations of magneto-Seebeck voltage in MgO and Al_2O_3 based MTJ are discussed in last section of this chapter.

In this chapter we will present the experimental background of the experiences and the simulation protocols. After presenting the sample fabrication process, we will discuss about the importance of fully modeling the electrical detection set-up to avoid artefacts that can lead to misinterpretations. Finally the different structures that have been simulated will be presented with their associated protocol. The results will be discussed in the following chapters.

2-1 PVD AND SAMPLES

The samples made in this thesis are deposited by magnetron sputtering and then processed using optical lithography. The characterization techniques, including magnetic measurements and transport measurements, such as spatial resolved and/or time resolved measurement, are introduced in the following sections.

The multilayers have been grown using an Alliance Concept UHV sputtering set up with base pressure less than 3×10^{-9} mbar. (Fig. 2-1)

Figure 2 - 1: Photo of the Alliance Concept UHV sputtering used in the PhD work.

In this sputtering, 10 targets are available and fixed on magnetrons that can be connected to either DC or RF sources. In order to clean the sample surface, the substrate holder can also be polarized, either in DC or RF modes. Two process gaz lines are available in the machine: the conventional Ar but sputtering using pure O_2 or a mixture of Ar/O_2 is also possible.

The typical multilayer structure is: substrate/Ta (5nm)/Co (10nm)/IrMn (7.5nm)/Co (5nm)/Al_2O_3 (2nm)/Co (10nm)/Pt (5nm). This multilayer has been studied and optimized in a previous PhD work [81]. The Ta (5nm) is amorphous and is used to promote the adhesion of the multilayer on the substrate, to reduce the interdiffusion of atoms of the substrate and promote the (111) texture of the Co(10nm). This Co layer is used to promote texture of the (111) IrMn antiferromagnetic layer. The Co thickness was chosen to optimize the texture and reduce the resistance of the bottom electrode. The (111) crystalline orientation is needed to have a high exchange coupling constant at the IrMn (7.5nm)/Co (5nm) interface. The maximum of exchange coupling constant is observed at 5nm of IrMn and decreases strongly when the thickness is reduced. Therefore, 7.5nm was chosen to keep high exchange even with fluctuation of the IrMn thickness. The IrMn exchange biases a Co (5nm) layer which is (111) textured. The thickness has been chosen to have a high exchange bias field (inversely proportional to the Co layer thickness) and to limit the diffusion of Mn towards the tunnel barrier during thermal annealing to set up the bias.

The amorphous Al_2O_3 tunnel barrier was made in two steps [82]: first of all, a 2nm thick aluminum layer was rf sputtered. Then, using an Ar/O2 mixture, the 2nm thick aluminum layer was oxidized using a RF polarization of the substrate holder. While the O_2 oxidizes the surface, the Ar sputters the surface to get a smooth surface. As a result, a 2nm thick Al_2O_3 layer is obtained.

The oxidation time was optimized to get the highest TMR value. Fig. 2-2 shows TMR of Al_2O_3 MTJ of different oxidation time. On one hand, when the Al layer is under oxidized, the Al layer between the Co and

Al_2O_3 layers depolarizes the electrons and reduces TMR. On the other hand, when the Al layer is over oxidized, the Co bottom layer is oxidized reducing the TMR. The optimum of oxidation time has to be found.

Finally, the Co (10nm)/Pt (5nm) top electrode is deposited, Co (10nm) to ensure a continuous soft electrode and Pt (5nm) to protect the Co layer against oxidation and the technological processes during lithography. After the deposition of the full stack, the multilayer was annealed under an applied field of 200 Oe at 200°C during 1 hour to set up the exchange bias field.

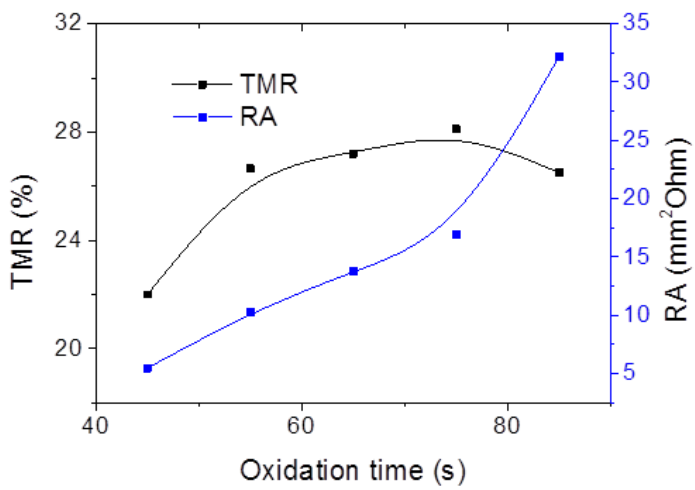

Figure 2 - 2: Evolution of TMR and RA as a function oxidation time *for substrate/Ta (5nm)/Co (10nm)/IrMn (7.5nm)/Co (5nm)/AlO_x (2nm)/Co (10nm)/Pt (5nm). TMR (black, left) is maximal for 75s of oxidation. Resistance area (blue, right) increases as the oxidation time increases.*

The same magnetic properties of the multilayer stack and the same tunnel characteristics have been obtained independent of the substrate. In my PhD, several substrates have been used.

Substrate	Information

Glass	Corning 1737
n-Si (100)	1-10 Ohm·cm
n-Si (100)	1000 Ohm·cm
p-Si (100)	1-10 Ohm·cm
p-Si (100)	1000 Ohm·cm
n-Si (100)/SiO_2(100 nm)	1-10 Ohm·cm
n-GaAs	0.01-0.1 Ohm·cm

Table 2 - 1: List of substrates used in this thesis.

Some Si wafers have been covered using an insulating layer: SiO_2 (100nm) made by thermal oxidation, MgO (10nm or 20nm) made by sputtering. The layer is continuous and is crystalline on the Si(100) layer [83].

2-2 MAGNETOMETRY

Before patterning the sample, magnetometry measurements have been performed on the full films to characterize the magnetic properties. The magnetic measurements of the multilayers have been performed in the Institut Jean Lamour at room temperature by using a Vibrating Sample Magnetometer (VSM). Pictures of the set up can be found in Fig. 2-3. All the "magnetization versus field" M-H loops have been recorded for an applied field parallel to the sample surface.

Figure 2 - 3: VSM setup of Institut Jean Lamour. *The functionalities of different parts of the VSM are explained.*

Fig. 2-3 shows a typical M-H loop. Three contributions to the M-H loop can be identified. From the layer thicknesses and the amplitude of the magnetization jumps, the more shifted loop attributed to the 5nm thick exchange biased Co layer. The other two Co layers have the same thickness and so the same magnetization jump, but one is slightly exchange biased with IrMn. Those characteristics are important to understand the results shown in Chapter 3, 4 and 5.

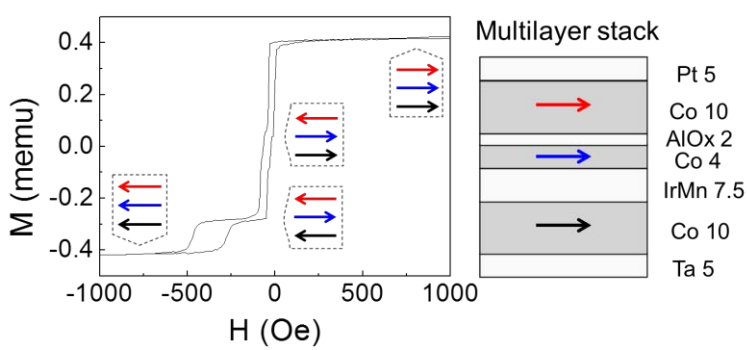

Figure 2 - 4: Magnetization as a function of field for the multilayer stack. *The multilayer structure is shown on the right: Ta*

(5nm)/Co (10 nm)/IrMn (7.5nm)/Co (4nm)/Al_2O_3 (2nm)/Co (10nm)/Pt (5nm). The magnetization orientations of the three magnetic Co layers (arrows of different colors) are shown during the full loop.

2-3 LITHOGRAPHY

In order to force the electrons to tunnel through the Al_2O_3 tunnel barrier, the multilayer is patterned into devices to take an electric contact on the top and the bottom electrodes. The geometry of a typcial sample is shown in the Fig. 2-5.

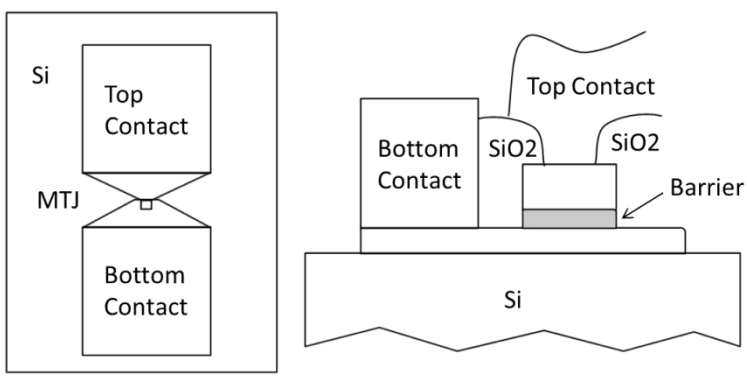

Figure 2 - 5: Sketch of MTJ geometry. *a) Top view; b) side view. (Size not to scale.)*

In a first step, the upper layers Al_2O_3/Co/Pt are patterned into squares. In our study, the lateral size of the MTJ was varied between 50 µm and 100µm. Fig. 2-6 shows optical view of the shape of the resist. Dry Ar Ion milling with secondary ion mass spectrometry (SIMS) analysis is used to etch the parts of the multilayer that are not protected by the resist.

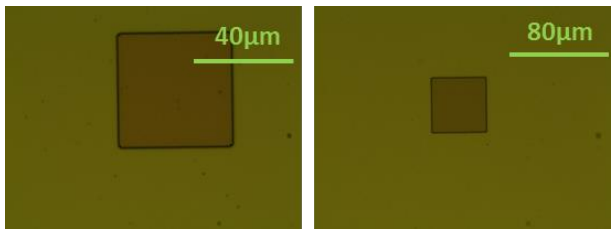

Figure 2 - 6: Optical microscope photo of resist in the shape of square junction. *Resist on top of the multilayer stack to define the lateral shape of the tunnel barrier.*

Using the SIMS analysis, the ion etching was stopped after or just at the end of the removal of the Al_2O_3 layer. It can be seen in Fig. 2-7 that the signal of the Co increases from 440s after a decrease.

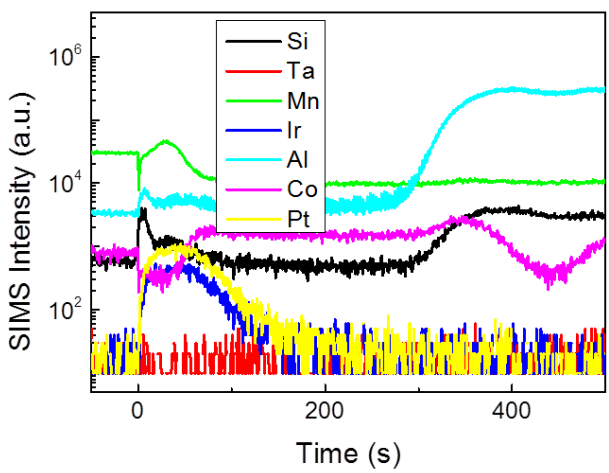

Figure 2 - 7: SIMS analysis during the Ar etching in the first step. *The SIMS signal is plotted as a function of etching time.*

In a second step, the bottom electrode is defined. The shape of the resist that will be etched into the multilayer stack is given in Fig. 2-8. Once again, dry Ar ion milling with SIMS analysis is used to etch the parts of

the multilayer that are not protected by the resist. It is important to note at this point, that the bottom electrode is composed of the bottom layers up to the Al_2O_3 tunnel barrier i.e the following stack: Ta (5nm)/Co (10nm)/IrMn (7.5nm)/Co (5nm). We have the two exchanged biased Co layers in the bottom electrode. This will play an important role in the measurement of the Nernst effect detected in these samples.

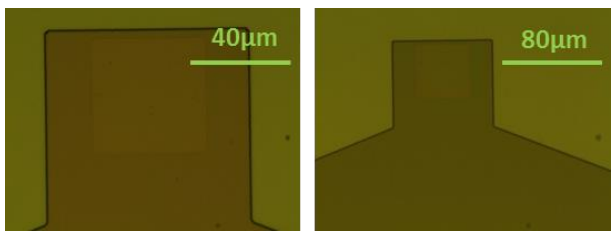

Figure 2 - 8: Optical microscope photo of resist in the shape of bottom electrode. *Resist on top of the multilayer stack to define the lateral shape of the bottom electrode.*

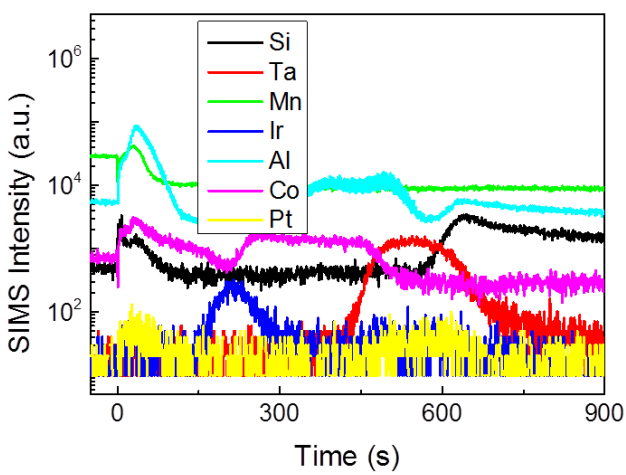

Figure 2 - 9: SIMS analysis during the Ar etching in the second step. *The SIMS signal is plotted as a function of etching time. The ion etching stops in the Si.*

Using the SIMS analysis, the ion etching was stopped in the Si. It can be seen in Fig. 2-9 that the signal of the Si increases after 650s of etching.

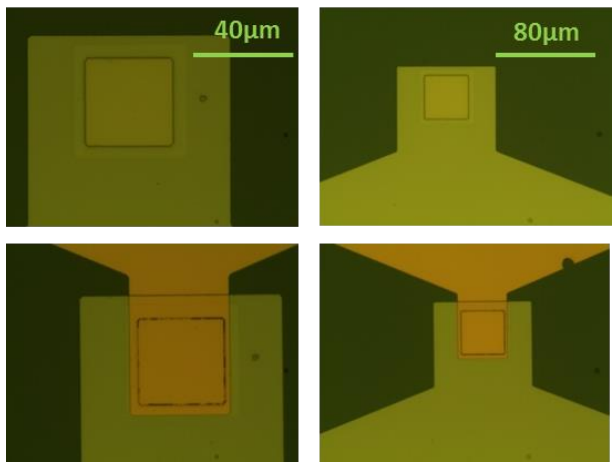

Figure 2 - 10: Optical microscope photo of the opening and top contact. *In the upper two pictures, resist on top of the multilayer stack to define the lateral shape of the tunnel barrier. The lower pictures show the top contact is made on top of the opening.*

In the two last steps, a technological insulator, in our case SiO_2, is sputtered all over the surface, except on top the tunnel barrier and on parts of the bottom electrode. Those regions have been protected by resist and opened by lift off after SiO_2 deposition. The thickness of SiO_2 is 100 nm (Fig. 2-10, top). Finally, the top electrode and a contact on the bottom electrode are added (Fig. 2-10, bottom). This contact can be made either with Ta (10nm)/Pt (100nm), or Cr (10nm)/Au (150nm) or Ta (10nm)/Cu (100nm).

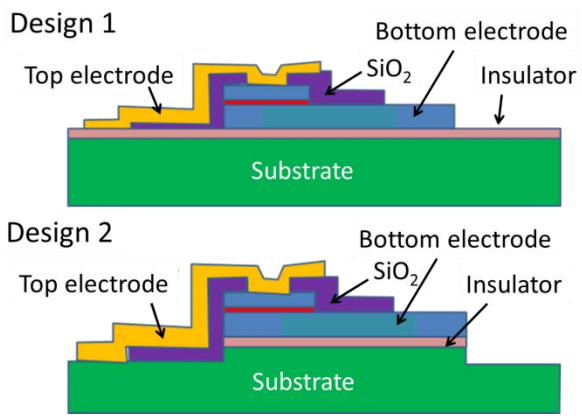

Figure 2 - 11: Two different geometries of the top contact used in this thesis.

As far as the top contact is concerned, two geometries have been chosen. The first design (Fig. 2-11, top) is the conventional design. Either the substrate is an insulating substrate or an insulating layer is deposited between the substrate and the top and the bottom electrode. In the second design (Fig. 2-11, bottom), a conducting substrate is used and an Ohmic contact is made between the top electrode and the substrate. A thin insulating layer is deposited between the bottom electrode and the substrate.

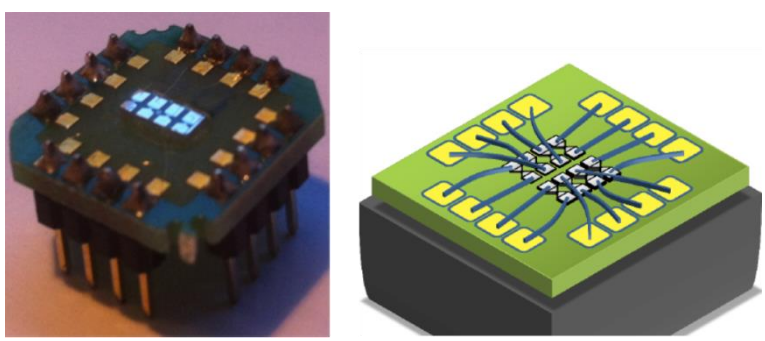

Figure 2 - 12: The pictures of magnetic tunnel junctions mounted on a chip.

After dicing, the MTJs are directly measured in a probe station using tungsten tips or are glued on a chip and bounded (Fig. 2-12, left). An artistic view of the geometry is given in Fig, 2-12 right. A typical R-H loop is given in Fig. 2-13. By the use of the IrMn antiferromagnetic layer and a thin Co layer, the parallel and antiparallel configurations are well defined. In the tunnel transport characteristics, the presence of the 10nm thick Co buffer layer, exchange biased by the IrMn layer, is obviously not detected.

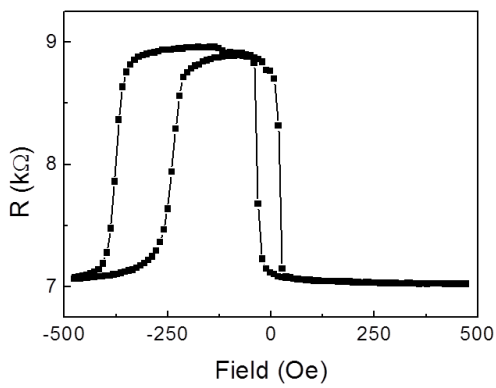

Figure 2 - 13: Typical resistance versus field loop of an Al_2O_3 MTJ. *The multilayer structure consists: Ta (5nm)/Co (10nm)/IrMn (7.5nm)/Co (5nm)/Al_2O_3 (2nm)/Co (10nm)/Pt (5nm). The reversal of the 10nm thick free Co and 5nm thick Co pinned layer are clearly separated.*

2-4 TRANSPORT MEASUREMENT WITH LIGHT

The goal of this work is to highlight thermoelectric effects in spintronic devices. Therefore, a controlled local temperature gradient has to be applied to the device. We make the choice to use a laser. In order to study the different mechanisms that can be involved in the complex

samples we studied, various laser setup have been adopted for the measurement:

1) laser diode
2) laser diode coupled into optical fiber
3) Raman laser
4) OPO (optical parametric oscillator) laser

For DC measurements, simple laser diode (1) of 800nm was used to shine at the sample. Samples are electrically connected to the setup using probes or wire-bonding. In-plane magnetic field can be applied to access the magnetic dependence (Fig. 2-14).

For AC measurements and more accurate DC measurements, the 800nm laser diode is coupled into optical fiber (2) to have smaller spot size and more flexibility. The position of the laser diode is then controlled by a precise translation stage. Keithley nanovoltemeter and Stanford Research SR830 lock-in amplifier are used to measure the DC and AC voltages respectively. To increase the sensitivity for AC measurements, a SR 560 preamplifier can be added.

For the spatial-resolved measurements, we use the Raman laser setup (3) which has a smaller spot size (10μm in diameter) and also a better control of the laser position. The HeNe laser of 632.8 nm is focused systematically with a 100X objective. The laser shines perpendicular to the sample plane. Voltage is recorded with a Keithley 2000 voltmeter as the laser spot scans over the sample.

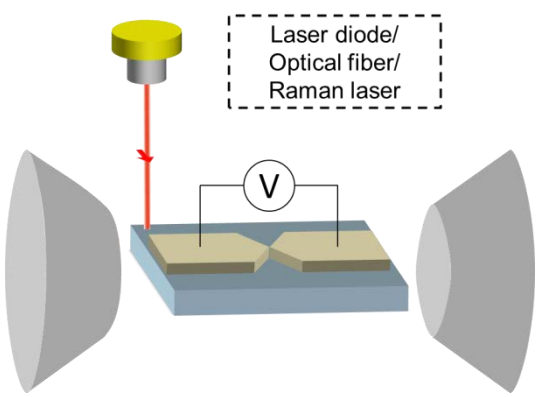

Figure 2 - 14: Sketch of setup for transport measurement. *Laser diode (with optical fiber) or Raman laser is used as laser source. Voltage is measured under tunable magnetic field and tunable laser radiation.*

For time-resolved measurements, an OPO (optical parametric oscillator) pulse laser (4) [84] with wavelength ranging from 400nm to 2200nm was used. In an OPO laser, the input laser wave is converted into two output waves of lower frequency by means of second-order nonlinear interaction. The laser is then focused on the sample. To get a better signal-to-noise ratio, voltage signal is amplified using a preamplifier Stanford Research SR560 with 1 MHz bandwidth and recorded using an oscilloscope.

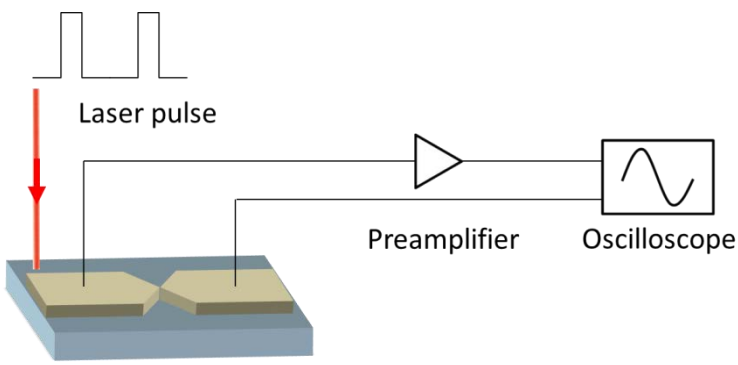

Figure 2 - 15: Sketch of setup for time resolved measurement. *Periodical laser pulse shines at the sample and the voltage signal is amplified using a preamplifier before recorded by an oscilloscope.*

2-5 IMPROVEMENT AND FULL CHARACTERIZATION OF THE ELECTRICAL DETECTION LINE

Because thermoelectric effects and especially spin dependent thermoelectric effects can show weak signal, their accurate detection is difficult and experimental artifacts can lead to misinterpretation. Attention of the experimental setup and its electrical description need to be taken seriously.

First, ideal instrument to measure electrical properties doesn't exist in reality. Real instruments can usually be treated as ideal instruments in certain conditions. In the field of spintronics, usually we have to deal with measurements in extreme conditions, sometimes very close to the application limit. Therefore it is important to keep in mind the application range of the devices. In this section, we discuss several common errors in a real measurement. For all electrical measurements, two kinds of errors can be distinguished: internal errors, due to the electrical architecture of the detection instrument and external errors, due to the wiring of the set-up. Finally we want also to stress that, due to the complexity of the samples, a full electrical description of the latter is necessary to avoid misinterpretation of the measurement.

DC measurement

When we connect a voltmeter, for example a Keithley 2000, to a resistor without any voltage sources, we would expect the reading to be zero. Usually it is not the case. Likewise when the sample under test (DUT) has an internal resistor, the measured voltage can deviate from the real value of the equivalent voltage source of the DUT. We will present here the different error sources for such instrument. For these measurements we used two kinds of DC voltmeters: Keithley 2000 and Keithley 2182A Nanovoltmeter.

Internal Error

Internal errors refer to the error due to internal circuit of the instrument, intrinsic properties of the voltage source and measurement instrument.

Examples including input resistance, input bias current, Johnson noise, 1/f noise.

First, for such measurement, a very important point is that the input resistance of a real voltmeter is not infinite. If the internal resistance of the DUT (R_S) is close or comparable to the input resistance of voltmeter (R_{IN}), the measured voltage is smaller than the real DUT voltage. As is shown in Fig. 2-16a), the measured voltage is $V_M = V_S\left(\frac{R_{IN}}{R_S+R_{IN}}\right)$. For the two multimeters used the internal DC resistance is superior to 10GΩ.

Due to internal circuit of a real voltmeter, input bias current always exists at the input, which could lead to significant error if the resistance of the DUT is big. The measured voltage is then: $V_M = V_S \pm I_{BIAS}R_S$. The input bias current is generally very sensitive to the temperature.

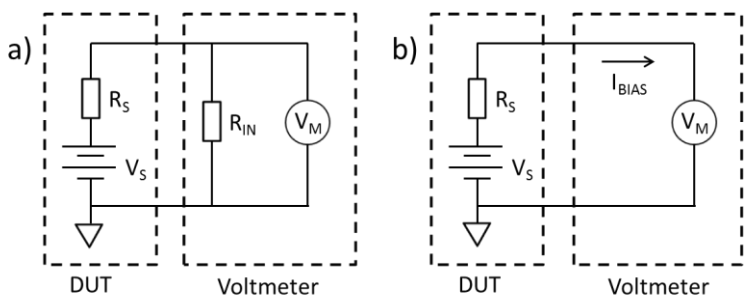

Figure 2 - 16: Influence of finite input resistance and input bias current. *Due to the finit input resistance of the voltmeter (a) or input bias current (b), the measured voltage V_M is different of the source V_S.*

Another limitation for the electrical measurements is the different noise sources present in the DUT and in the multimeter.

For instance the Johnson noise comes from the electron motion excited by the thermal energy. Johnson noise is the theoretical limit for electric measurement. The noise voltage can be calculated using $\sqrt{4kTR\Delta f}$, where k is the Boltzman constant, T the temperature, R the total

resistance of the electrical set-up and Δf the bandwidth of the measurement.

1/f noise presents in almost all electronic devices. The power spectral density (energy or power per Hz) is inversely proportional to the frequency of the signal. The 1/f noise is important at low frequency and DC measurement. At high frequency, 1/f noise is usually overshadowed by other noise.

This list of noise sources is not exhaustive but it can be treated, in the point of view of the voltmeter, as a current noise source in parallel to the input impedance and a voltage noise source in series δV_{noise}. Then the noise voltage measured by the voltmeter is $\delta V_M = \delta V_{noise} + \delta I_{noise} R_S$ if $R_S \ll R_{IN}$.

Because a major part of the noise sources are fluctuations due to the thermal energy, decreasing temperature could lead to smaller noise voltage. Another important point in order to reduce the integrated noise power is to reduce the bandwidth of the measurement and to increase the averaging. Because a real DC measurement doesn't exist, all multimeter have a finite bandwidth. But reducing the bandwidth cause to increase the measurement time, and make the experiment more sensitive to thermal fluctuations. In this context, the key point is to find the best compromised.

The values of the quantities discuss below for the two voltmeters used can be found in the following references [85,86].

External error

Errors due to environmental factors are classified as external error, including thermoelectric voltage, magnetic field, ground loops , pick-up noise et al. The influence of these factors are discussed in the following. Solutions are suggested.

One example of external error comes from temperature variation. When two connectors made of different materials are joined together in a circuit, the metal pair can be viewed as a thermocouple and thus is sensitive to the environment temperature. Thermoelectric voltage behaves as an offset in a voltage measurement. To reduce the

thermoelectric voltage, we need to decrease the Seebeck coefficient or the temperature gradient in the circuit. If the circuit is made of just one metal, the thermoelectric voltage will very small. Otherwise, efforts should be made to maintain a homogenous temperature in the circuit, such as keeping heat source away from measurement.

Spintronic measurements are usually performed in the presence of a changing magnetic field. The induced voltage is propotional to the loop area. If possible, the loop area should be as small as possible to minimize the voltage induced by magnetic field.

Fig. 2-17 shows a circuit with ground loops. When the sample and measurement device are grounded to different points, the voltage between the two ground points applies an additional voltage to the source. To avoid ground loops, all the equipments should be grounded to a single point. Powerful instruments, such as power supply for an electromagnet, should be grounded separately, because the noise from a powerful instruments could be overwhelming for sensitive measurement device.

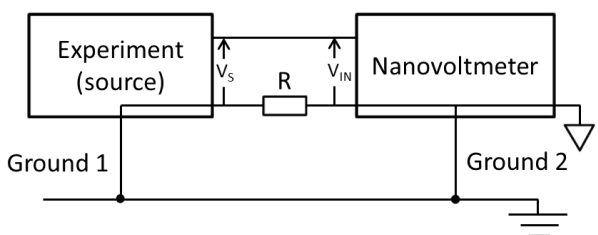

Figure 2 - 17: Illustration of ground loops. *The voltage source and the nanovoltmeter are not grounded to a single grounding point. [87]*

Another error comes from the pick-up noise. Our measurement circuit is usually subject to multiple electromagnetic field, such as 50Hz/60Hz electric grid, fluorescent lights and communication device. In DC measurement, pick-up noise can be averaged out by increasing the integration time or by synchronizing the measurements to the frequency of the line at 50/60 Hz.

AC measurement

AC measurement refers to the voltage measurement performed using lock-in amplifier. Almost all the errors of DC measurement exist in an AC measurement. In addition, errors specific to AC measurement are discussed in the following.

Internal Error

In addition to all the internal errors discussed above, AC measurement is also subject to the influence of capacitors from voltage source and instrument itself. Take Stanford Research 830 lock-in amplifier as an example, an proper measurement need to consider the capacitors from internal circuit. Especially, hidden capacitors like the capacitor of the BNC cables could lead to significant errors in high frequency measurement.

Fig. 2-18 shows a complete circuit of input end for a SR830 lock-in amplifier. This circuit has been obtained from the electrical diagram given by Stanford Research [88]. Capacitors due to external cables and internal wiring are extracted by performing simulation in the frequency range of 10Hz to 50kHz. A function generator with a test resistance in series is used as voltage source. We use output mode A or A-B to measure the frequency dependence. The experiment curve is then fitted with the circuit of Fig. 2-18. As can be seen in Fig. 2-19, excellent fitting can be achieved for test resistance of 15.13kOhm and 100.13kOhm.

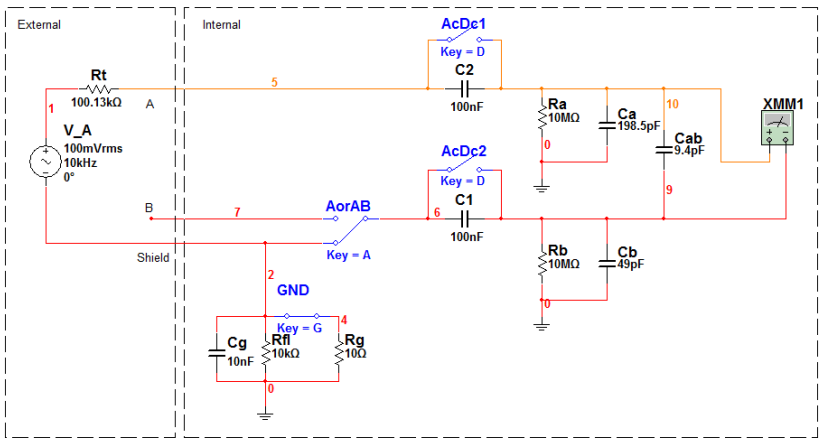

Figure 2 - 18: Circuit to simulate all the hidden capacitors. *The capacitors include the contribution from external wire and internal circuit.*

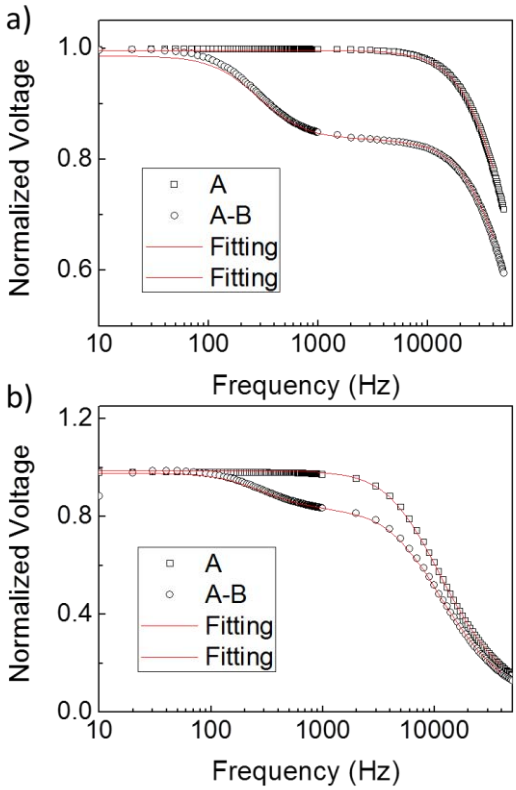

Figure 2 - 19: Voltage versus frequency with different test resistances. *Experimental data (empty dots) and fitting (red line) for test resistance of (a) 15.13kOhm and (b) 100.13kOhm. Fitting is performed using the circuit shown above.*

External error

The problems due to thermoelectric voltage, magnetic field, ground loops , pick-up noise exist in lock-in measurement. Attention should be paid to the pick-up noise. Fig. 2-20 shows an example of pick-up noise. The laser diode powered by a square wave shines at the sample. Lock-in measurement was performed at the same frequency of the square wave. Laser diode is emitting laser but also accompanied with electromagnetic wave as is shown in Fig. 2-20a). We could measure a stable voltage due

to the antenna effect of the sample. Since we are interested in the light induced voltage, such noise could easily lead to misinterpretation.

Pick-up noise can be weaken by moving the noise source away from the measurement and proper shielding of the noise source.

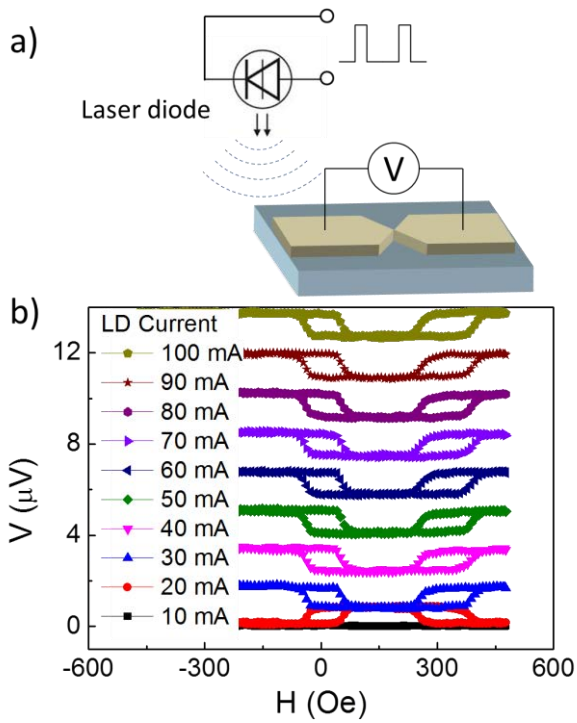

Figure 2 - 20: Pick-up noise in AC measurement. *a) The measurement setup b) The measured voltage at different laser power.*

2-6 SIMULATION

We perform finite element simulation to understand the static/dynamic heat propagation. We use the heat transfer module of COMSOL, which basically provides a numerical solution to the heat equation:

$$\frac{\partial T}{\partial t} - \frac{\kappa}{c_p \rho} \nabla^2 T = 0,$$

in which κ is the thermal diffusivity, c_p specific heat capacity and ρ the mass density of the material. The coefficient $\alpha = \frac{\kappa}{c_p \rho}$ is called thermal diffusivity.

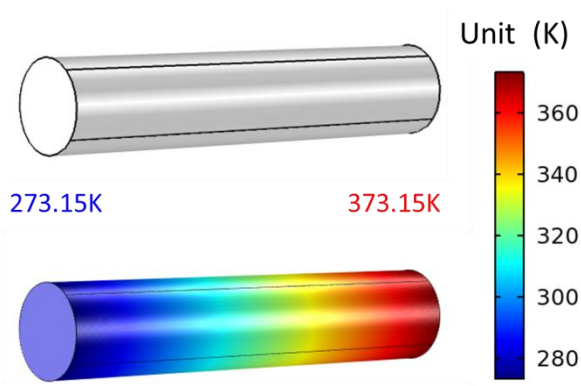

Figure 2 - 21: Example of COMSOL heat transfer simulation. *A Copper cylinder of 1mm radius and 10mm length was defined. (Upper) The two ends are in direct contact with heat sink of 273.15K and 373.15K. The finale temperature distribution is shown in lower part of the figure.*

A simple example of simulation on heat propagation is shown in Fig. 2-21 to explain the simulation process. The example solves the temperature distribution of a copper cylinder of 1mm radius and 10mm length with the two ends in contact with a cold heat sink (273.15K) and a hot heat sink (373.15K). The two heat sinks serve as two boundary conditions for the heat equation. The influence of air is neglected in this simple example. Generally in more

complicate scenarios, inward or outward heat flux could present. All the information is necessary for solving the heat equation. The final heat distribution in the copper cylinder is shown in the lower part of Fig. 2-21.

In Chapter 3, we simulated the temperature distribution under constant laser shining. It has to be mentioned that we don't take into account of the numerous interfaces in multilayers. Note that we don't take in account the numerous interfaces in metallic multilayers. In our case, heat propagations from the lead to the junction area over a distance of several hundreds of μm. Neglecting interfacial thermal resistance will not cause significant error. In Chapter 4, the influence of distance, boundary condition, material choices are checked for the heat propagation in Si substrate. The dynamic of heat propagation will be compared with time-resolved data from experiments.

A few publications [17,18,70] have shown that laser could induce a voltage in magnetic tunnel junctions, the order of which is around a few μV. In our precedent work [17] on Al_2O_3 tunnel junctions, the magnetic dependent voltage has been shown to reach 1 mV. This result has motivated new studies and is the starting point of my PhD work. The aim was to understand the origin of the giant magnetic dependent voltage, and further increase the voltage. Many factors needed to be examined to elucidate the origin of the giant voltage, including substrate, MTJ geometry, materials of the electrodes, materials of the MTJ Al_2O_3 etc...

3-1 PREVIOUS RESULTS

Our precedent work reported measurement result performed in open circuit geometry and in close circuit geometry, as is shown in the inset of Fig. 3-1. The voltage measured in the open circuit geometry depends on magnetic configuration. The ratio $(V_{AP} - V_P)/V_P$ is around 40%, close to TMR ratio. The voltage of AP state or P state increases as the laser power increases, while the ratio is found to be almost independent of the laser power. (Fig. 3-1a) For all the laser power, the laser induced current is independent of the magnetic configuration. (Fig. 3-1b)

If we attribute the effect as Seebeck effect, a phenomenological expression can be given considering the temperature difference across the Al_2O_3 barrier. The temperature difference between both sides of the Al_2O_3 barrier is defined as ΔT whereas the voltage difference is ΔV. As is shown in section 1-2, the total electric current I in the presence of ΔV and ΔT can be written as $I = G_V \Delta V + G_T \Delta T$ in the linear response approximation. G_V is the electrical conductance, and G_T is the thermoelectric coefficient related to charge current response to the heat flux. In the open circuit geometry, we set $I = 0$ and ΔV is proportional to the temperature difference. In the close circuit geometry, we set $\Delta V = 0$ and the close circuit current is proportional to the temperature difference.

This could explain why the open circuit voltage and close circuit current increase as the laser power increases.

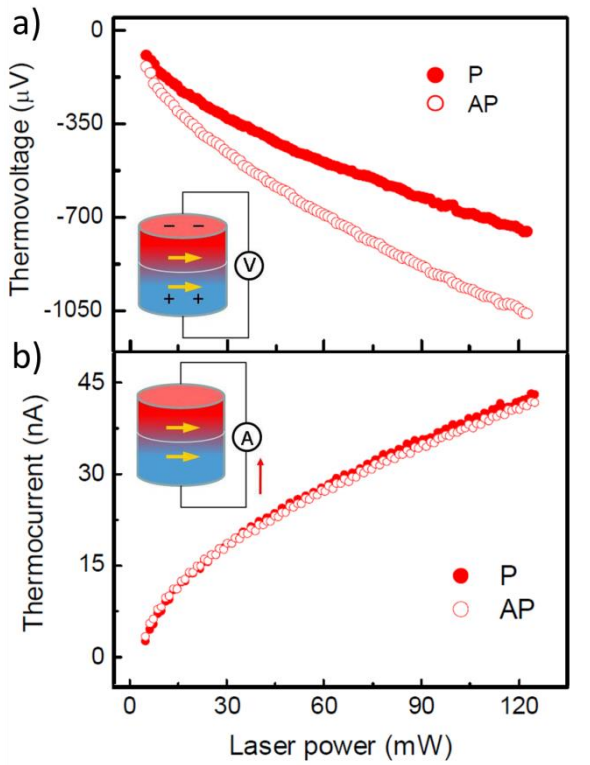

Figure 3 - 1: Previous results of laser measurement. *a) Laser induced voltage in open circuit geometry and b) laser induced current of close circuit geometry as a function of laser power. Inset shows the sketches of the open circuit geometry and the close circuit geometry. [17]*

3-2 PREDICTION OF RESONANT STATES

The Seebeck voltage reaching 1mV is exceptionally large considering that the small temperature gradient across the insulator barrier is quite small. (See section 3-4) The giant Seebeck voltage was explained using a model that invokes the existence of resonant states during the tunnel process. A large non-magnetic resonant state has to exist close to the Fermi level. [17]

Set $I = 0$, we get the Seebeck coefficient: $S = \frac{G_T}{G_V} = \frac{L_{12}}{L_{11}}$. The Onsager coefficient $L_{11} = G_V$ and $L_{12} = G_T$ can be expressed as the order 0 and 1 of the transport function $\sigma(\varepsilon)$, $L_{11} = \int d\varepsilon\sigma(\varepsilon)(-\frac{\partial f}{\partial \varepsilon})$, $L_{12} = \frac{1}{-eT}\int d\varepsilon\sigma(\varepsilon)(\varepsilon - \mu)(-\frac{\partial f}{\partial \varepsilon})$, in which f is the Fermi-Dirac distribution function. L_{11} and L_{12} are proportional to the density of states and its derivative at the Fermi level: $G_V \propto \rho(E)|_{E_F}$ and $G_T \propto \left.\frac{\partial \rho(E)}{\partial E}\right|_{E_F}$. [17,18]

If a peak of non-magnetic resonant states does exist, G_T becomes big and is independent of the magnetization configuration. Experimentally one would expect a giant Seebeck voltage and the voltage ratio deduced from the voltage at P and AP configurations will be close to TMR.

The concept of resonant level is not something new. The thermoelectricity community has been working on the effect of resonant states to increase the Seebeck coefficient. [89] Various other approaches have been used to introduce resonant states, including resonant dilute Kondo effects, hybridization effect and Zeeman splitting. [89–91] In our case, we tried to change interfacial states at the Co/Al_2O_3 interface by changing the oxidation time.

3-3 SAMPLE INFORMATION

A series of AlOx based MTJ was prepared on Si/Al_2O_3 (400 nm) substrate. The MTJ stack consists of a bottom reference layer Ta(5 nm)/PtMn(25 nm)/CoFe (2 nm)/Ru(0.8 nm)/CoFe(3 nm) and a free layer CoFe(2 nm)/NiFe(5 nm)/Ru(4.8 nm)/Au(10 nm) separated by a tunnel barrier made of AlOx(2 nm). We use Cu(200 nm)/Ta as contact for electrical connection. As is discussed in section 2-1, we could optimize the AlOx barrier by tuning the oxidation time. Three samples with oxidation time of 20s, 30s and 40s were prepared for the study.

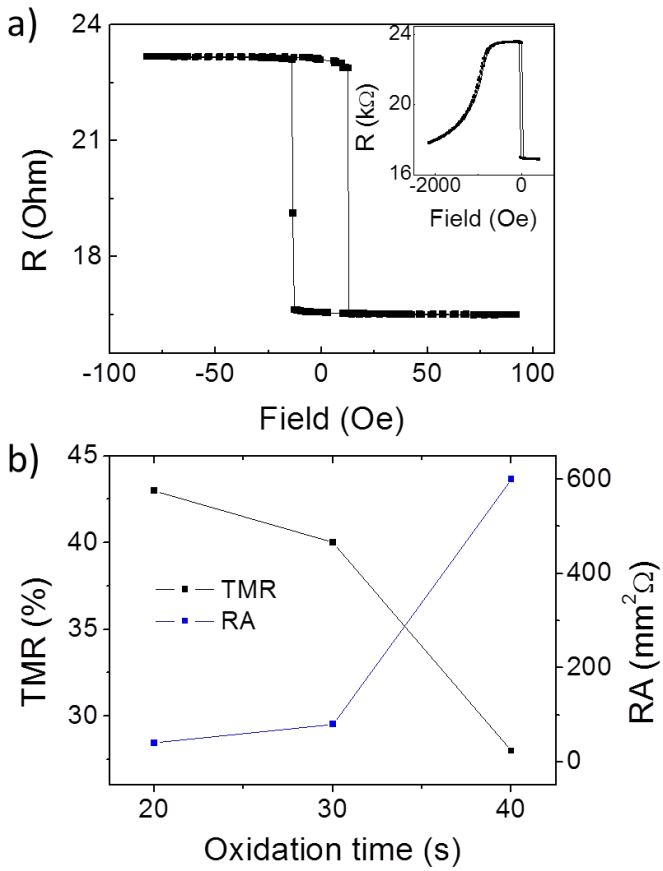

Figure 3 - 2: Resistance measurement of MTJ with different oxidation time. *a) Resistance as a function of external field for sample of 30s oxidation. Inset shows the complete R-H curve. b) TMR (black, left) and resistance area (blue, right) at room temperature as a function of oxidation time.*

Typical R-H curves are shown in Fig. 3-2a). Antiparallel and parallel magnetic configurations are well defined. Sample of 30s oxidation time shows TMR around 40%, which is a typial value for AlOx based MTJ. Fig. 3-2b) shows the TMR and RA values for samples with different oxidation time. For sample with 40s oxidation time, the decreased TMR (28%) indicates that the barrier is over-oxidized and the reference FM layer could have been oxidized its surface. The huge increase of RA for this sample suggests the same conclusion. This sample will be referred as over-oxidized sample in the following.

Inelastic tunneling spectra (IETS) has been proven to be an useful tool to study the tunneling behavior in MTJ. Phonon excitation and magnon excitation were studied using IETS and were compared with calculations. [92–94] If the giant Seebeck voltage comes from resonant sates, we should be able to confirm these states using IETS.

Fig. 3-3 shows the IETS spectra for three samples with different oxidation times. All three samples show spin-dependent peaks at around ±30mV. Among the three samples, MTJ of 20s oxidation shows the strongest peaks. But the amplitude of the peaks strongly depends on the magnetic configuration. Interestingly, for over-oxidized sample (40s), we observed an increase of non-magnetic contribution at around ±30mV. Such non-magnetic contribution is likely due to the oxidized FM layer beneath AlOx barrier. If the reported giant Seebeck voltage (30s oxidation time) is due to non-magnetic resonance, we should observe an even higher Seebeck voltage for the over-oxidized sample.

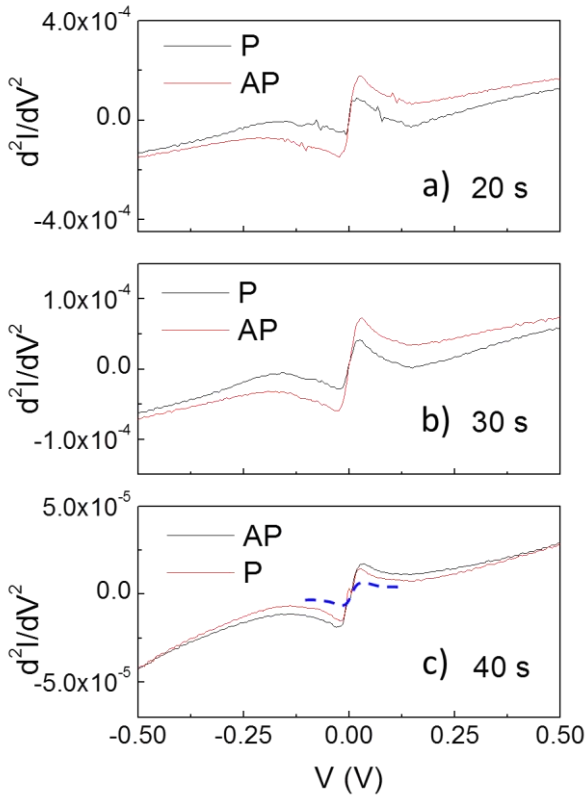

Figure 3 - 3: IETS spectra of P and AP states of MTJs with different oxidation time. *The figures a), b) and c) correspond to oxidation time of 20s, 30s and 40s respectively. The blue dash line in c) represents the increased non-magnetic states for this sample. All the measurements are performed at 15K.*

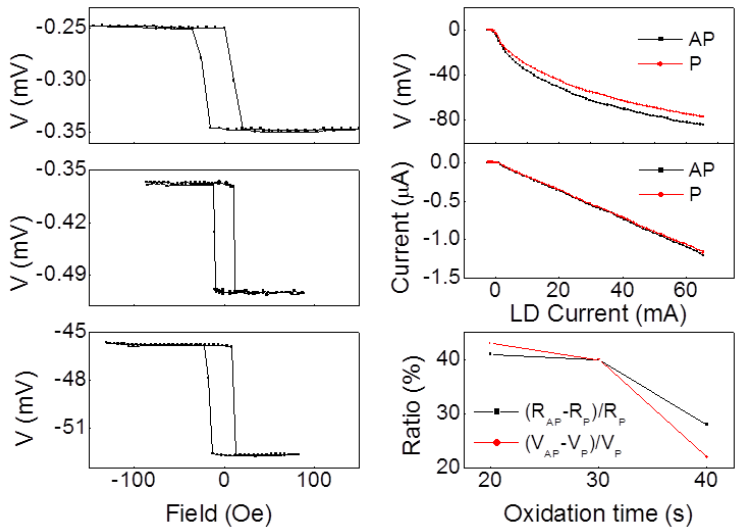

Figure 3 - 4: Electrical measurement under laser radiation. *Voltage versus field for oxidation time of 20s(a), 30s(b) and 40s(c) with laser diode power around 30 mW. d) Voltage and e) current as a function laser diode power. f) TMR and laser induced voltage ratio as a function of oxidation time.*

Fig. 3-4c), d) and e) shows the results from over-oxidized sample under the radiation of laser. For this sample, voltage above 80mV can be measured with a laser power around 60mW. The voltage depends on the magnetic configuration. The voltage increases as laser power increases for both P and AP configurations. (Fig. 3-4d) The laser induced current is independent of magnetic configuration. The behavior is similar with those in our previous work [17], except that the voltage is almost one hundred times larger.

Our model predicts that the ratio of laser induced voltage $(V_{AP} - V_P)/V_P$ should be equal to the TMR ratio. Experimentally the ratio of voltage evolves similarly as TMR as a function of oxidation time. However the exact equivalence is not found. (Fig. 3-4f) For oxidation time of 40s, the voltage ratio is found to be always smaller than the TMR ratio. Such disagreement indicates that other mechanisms might exist in our system.

This huge voltage in 40s oxidation sample was surprising since such huge amplitudes have never been reported in literature. One might guess this is due to the increased temperature gradient in our sample. Therefore, we performed finite element simulation to study the temperature gradient in the sample.

3-4 TEMPERATURE DISTRIBUTION IN METALLIC STRUCTURE

In this section, we focused on the temperature distribution in a MTJ structure under laser shining. To be specific, the sketch of MTJ is shown in the inset of Fig. 3-5. On Si/SiO_2 (200 nm), MTJ is defined as in the figure. The size of top and bottom leads is 1×1 mm^2. A uniform heat flux is applied on the top electrode. The bottom surface of Si is set to room temperature. Changing SiO_2 to Al_2O_3 will not change the result of the simulation, since both materials are amorphous oxides and have similar thermal properties.

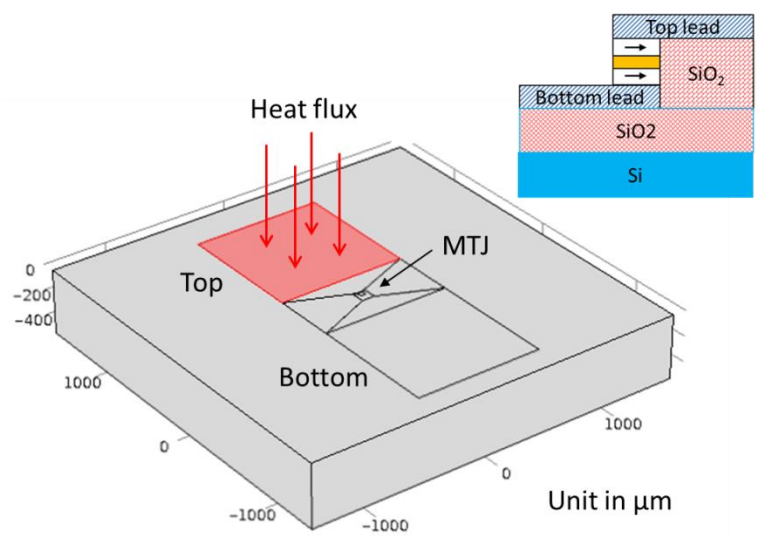

Figure 3 - 5: Problem of heat transfer in MTJ structure on silicon substrate. *The heat flux density 3000 W/m^2 is applied on 1 mm^2 top lead. The total heat flux 30mW is close to the power of a laser diode. Inset shows the sketch of MTJ.*

Fig. 3-6 shows the equilibrium temperature distribution. The top lead is heated to 293.2K, just 0.1K higher than the cool region. Fig. 3-6b) shows the temperature distribution of the slice $x = 0$. Both figures show that the temperature rise happens only at the region under steady heat flux (Marked with red arrows in Fig. 3-5). The simulation shows that the distance of heat propagation is limited to around 500 μm, which is driven by the thickness of Si.

The vertical temperature distribution is shown in Fig. 3-7. The temperature decreases with the depth. The rate of temperature decrease changes at different layers, as is shown in the inset of Fig. 3-7. The black curve shows the evolution of temperature at the center of top lead. The temperature is almost uniform in copper (200nm). The sharp temperature jump happens at the SiO_2 layer. Note that similar temperature jump exists also for temperature evolution at the center of MTJ (red curve). However it is far too small to be visible. Temperature decreases continuously in the bulk of silicon. The decrease speed at MTJ center is smaller than that at the center of top lead. This indicates that we should shine directly at the MTJ to get maximum temperature gradient across the MTJ.

As can be seen in the previous discussion, the temperature gradient in MTJ is very small when we apply a heat flux to the top lead. This is in agreement with related work in literature [18]. Here we assume that 30mW laser power is absorbed by the top lead, while in reality only a small part can be absorbed by the system. The majority of the power will be reflected at the metal surface, giving rise to an even smaller the temperature gradient.

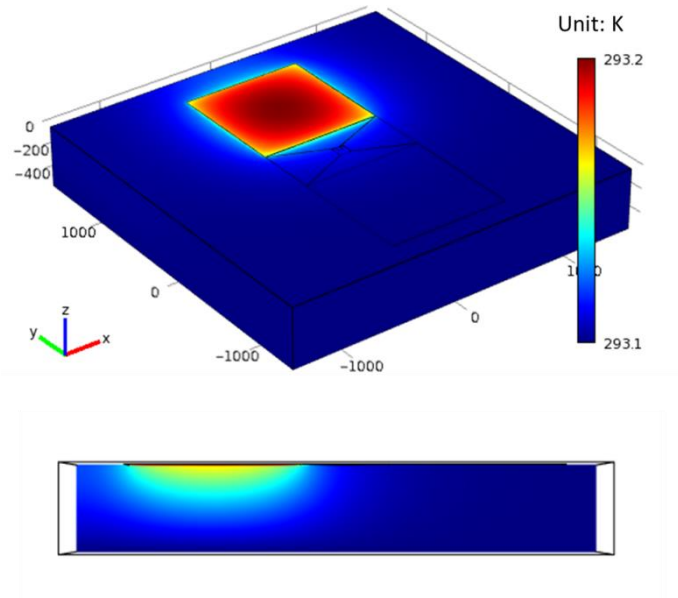

Figure 3 - 6: Static temperature distribution under constant heat flux. *(a) and (b) shows the simulation result for the whole structure and the slice at x=0 respectively.*

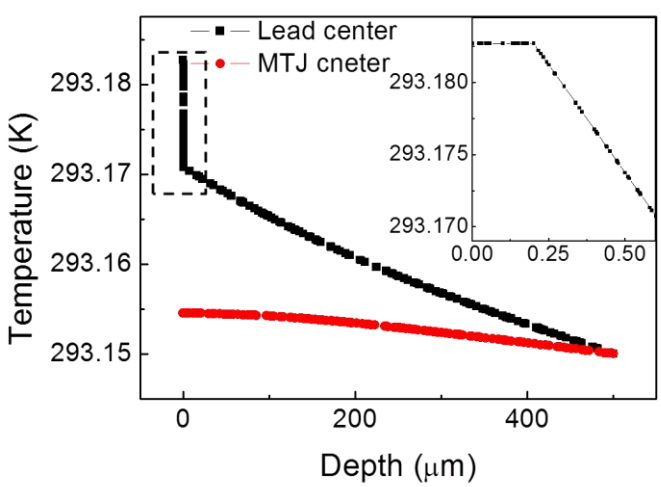

Figure 3 - 7: Temperature evolution as a function the depth. *The two studied point are located at the center of top lead (black) and junction (red). Inset highlights the temperature distribution in the metallic film (0.2 μm) and SiO_2 (0.4 μm). The main temperature drop happens in the SiO_2.*

Now we know that the temperature difference across the tunneling barrier is quite small (<1mK). If we consider the light induced voltage as Seebeck voltage, the Seebeck coefficient will be greater than $10^8 \mu V/K$, which is absolutely enourmous. On one hand it could certainly be good news for applications since this huge signal can be measured easily. On the other hand this incredible value plus the fact that the Magneto-Voltage ratio $(V_P-V_{AP})/V_P$ is no more equal to TMR are in contradiction with the previous model leading to a long search for the origin of this phenomena

3-5 INJURY OF ELECTRODE

Since a thick Al_2O_3 insulating layer (400nm) separates the sample and the silicon substrate, the role of Si was previously taken as insignificant. Moreover the high resistance and the value of the TMR of the MTJ measured are in agreement with other measured values in literature. Therefore those results did not alarm us…

Only measurements performed on uncutted wafers that did not show the huge light induced voltage started to help us in our investigation. We find out that after cutting the wafer to pieces to isolate one MTJ devices, the high Seebeck voltage became present again… We could then demonstrate that during the cutting procedure an electrical short cut between the leads and the silicon substrate was created. We confirmed that by creating an artificial contact between a lead and the silicon substrate Fig. 3-8 shows the light induced voltage as a function of external field under 30mW laser power. When the contact of MTJ was intact, the laser induced voltage is a few μVs and no influence of the magnetic configuration could be detected. This voltage can be attributed to some thermoelectric voltage in the multilayer stack, as there are lots of interfaces in a MTJ in addition to the tunneling barrier. After contact was

made between the bottom (and the top) electrodes and the substrate, the voltage induced by light of same power rose immediately to 60mV. It clearly shows that the giant voltage needs the contact between the silicon substrate and the electrodes. Sample grown on glass did not show any of those effects.

The detailed mechanism will be described in the Chapter 4.

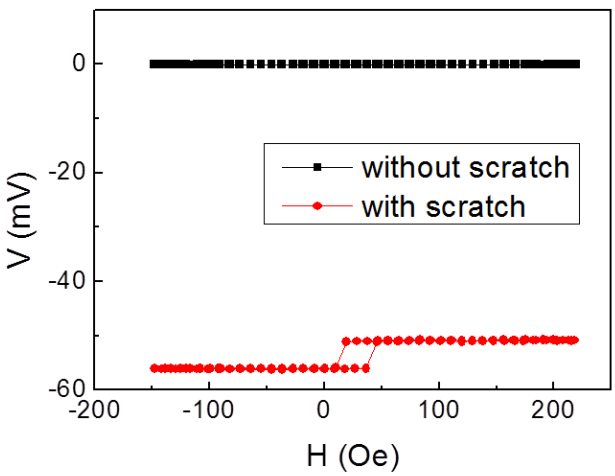

Figure 3 - 8: The influence of injury on the electrodes. *Voltage is plotted as a function of field measured for 40s oxidized sample a) without any scratch on the contact and b) with scratches on both electrodes.*

3-6 SUMMARY

We studied the IETS of AlOx based MTJ with different oxidation time. It was found that as the oxidation time increases, a non-magnetic contribution appears at low bias voltage. This non magnetic contribution

could indicate a higher magneto-Seebeck coefficient, according to the theory proposed in our previous work [17]. However, the huge light induced voltage is not due to the Seebeck effect across the AlOx tunneling barrier. To understand the giant light induced voltage, we must take the silicon substrate into consideration.

4-1 INTRODUCTION

As is discussed in Section 1-4, several publications have reported the laser induced voltage in MgO MTJ, the order of which reaches several hundreds of μV. Our precedent work on Al_2O_3 shows that the magnetic dependent voltage could reach the order of mV. The starting point was that we wanted to understand the origin of this giant magnetic dependent voltage, and further increase and control this voltage for possible application.

In order to elucidate the origin of the giant voltage, several factors need to be examined, including substrate, MTJ geometry, electrode, barrier et al. Results in Section 3-5 shows that the injury of electrode was responsible for giant laser induced voltage. The measurements on other samples, e.g. different substrate or different MTJ geometry, show a few μV under laser radiation, which can be explained using conventional Seebeck effect on metals. A contact between the leads and Si substrate is thus necessary to have an enhanced voltage. Therefore, we try to build a model system to study the photovoltage. We performed a series of measurements to characterize and understand the effect of light shining on a MTJ grown on a specific substrate.

This chapter is organized as follows. First of all we characterize the MTJ by measuring its conventional magnetoresistance (TMR) by simply measuring the resistance versus applied field as an external electric source is powering the device. Then we measured the generated voltage across the MTJs in absence of an external electrical power source but 1) as a continuous laser is shining the device, it is called DC measurement, 2) as the laser intensity is modulated at a given frequency while the voltage is measured synchronously, we call it AC measurements and 3) as a function of time after a single light pulse (typically 20 ns). This study is performed by analyzing the influence of the geometry of the sample, the nature of the substrate, as well as the size of the junction on the photo voltage and current. The influence of the light excitation is also probed by varying the intensity, wavelength and position of the light excitation. The optimized conditions are presented.

4-2 DC BEHAVOIR

Resistance versus magnetic field

First we show results obtained on the following MTJ stack: (Si p-low doping (substrate)/Ta (5nm)/Co (10nm)/IrMn (7.5nm)/Co (5nm)/Al_2O_3 (2nm)/ Co (10nm)/Pt (5nm)) for which two types of devices geometries have been processed as explained in Section 2-3. One called *No Contact* is a "conventional" design where the top lead is insulated from the substrate by a 150 nm SiO_2 thick insulating layer (Fig. 4-1a). The second one is called *Contact* where a direct metallic Ta/Au connection from the top lead to the substrate allows creating an electrical circuit including the MTJ in parallel to the substrate (Fig. 4-1a'). The size of the junction pillar is 20×20μm² and in the case of the *Contact* geometry the metallic connection 760×760, 120×120 or 20×20μm².

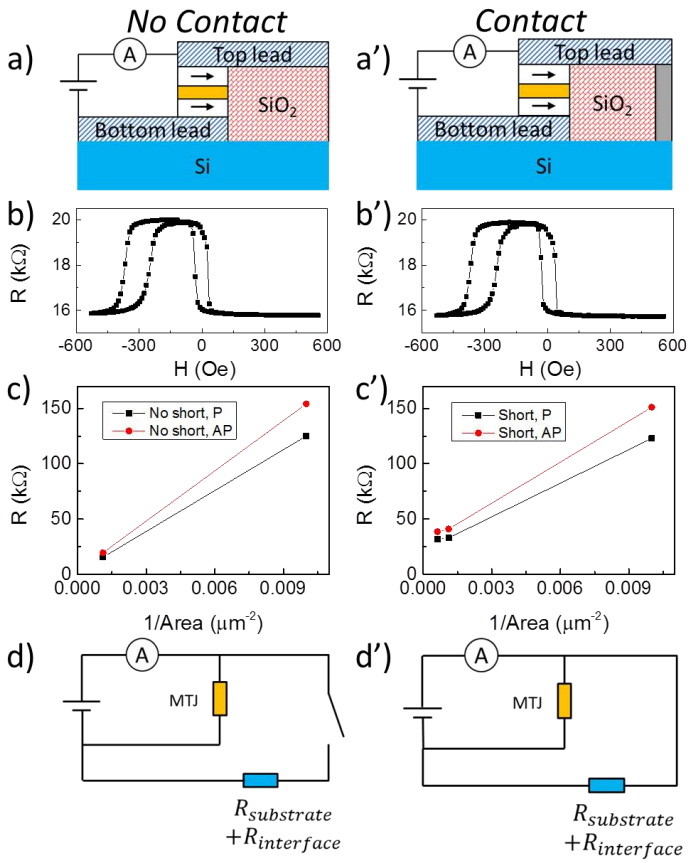

Figure 4 - 1: Resistance study of two magnetic tunnel junctions. *The multilayer stack, namely Ta(5nm) /Co(10nm)/ IrMn(7.5nm)/ Co(5nm)/ Al_2O_3(2nm)/ Co(10nm)/ Pt(5nm)), is grown on a Si substrate: in a* No Contact *(left panel) and* Contact *(right panel) geometry. a) Schematic of the devices in a resistance measurement configuration, b) Resistance of the MTJ as a function of the in-plane applied field c) Resistance of MTJ versus the inverse of the junction area, d) Schematic of the equivalent circuits that corresponds to the two geometries.*

Both the TMR (Fig. 4-1b, b') and resistance (Fig. 4-1c, c') are not affected by the device geometry (*Contact* or *No Contact*). Indeed the resistances of the MTJ in P and AP states are small compare to the

resistance of the parallel branch that includes the resistance of substrate and contact resistance, as sketched in Fig. 4-1d, d'). Moreover the contact resistance between the substrate and metallic contact include a Schottky barrier that will be discussed in the following. Consequently the TMR signal cannot be used as a proof of *Contact* or *No Contact* geometry.

Voltage versus magnetic field

DC voltage is measured under constant laser as the magnetic field is sweeping. Fig. 4-2a) and a') show the schematic view of the DC voltage measurement. When the device is no more powered by an electric source but a light source in the *No Contact* geometry, the DC voltage does not present noticeable changes with the magnetic field (Fig. 4-2b). This result implies that there is no detectable spin dependent voltage created across the studied MTJ. This result is confirmed when the Si substrate is replaced by an insulating glass substrate.

On the other hand, in the case of the *Contact* geometry the DC measured voltage presents a magnetic hysteresis loop comparable to the TMR signal. Under laser power of 60 mW, the voltage is -43.4mV and -49.4mV for P state and AP state, respectively. The difference between the two samples is shown in Fig. 4-2 c) and c'). The branch for MTJ and the branch of Si substrate are separated from each other by the insulator in *No Contact* geometry, which they are connected by the metal contact in *Contact* geometry.

In order to test the influence of the substrate on the effect we have grown the same stack on a Glass substrate and on GaAs substrate. On the glass substrate no field dependent signal could be detected whereas on a GaAs substrate a strong field dependent voltage similar to the one shown in Fig. 4-2b) could be detected. Since Glass is an insulator and GaAs a semiconductor those findings indicate that the nature of substrate is important for the light induced voltage. The behavior for different substrates will be explained in Section 4-4.

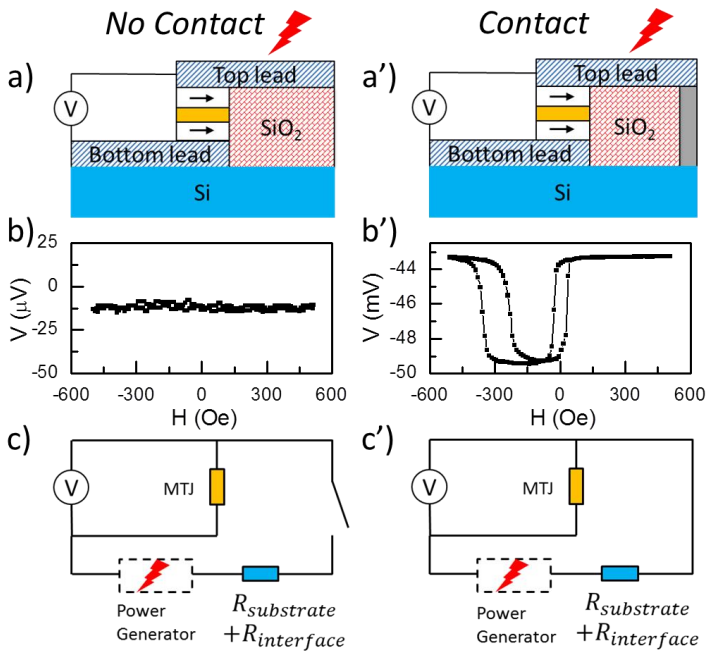

Figure 4 - 2: DC voltage measurement for the two geometries. *Samples No Contact (left) and Contact (right) measured at constant laser power 60 mW: a) Schematic of the device in a DC voltage measurement configuration. b) DC voltage as a function of in-plane magnetic field. c) Schematic representation of the equivalent circuit.*

Current versus magnetic field

By replacing the voltmeter by an ampermeter a DC current can also be measured. Laser induced currents in both geometries are measured under constant laser of the sample power (Fig. 4-3a and a'). In the case of the *No Contact* geometry, the measured current is below the sensitivity of the Keithley 2000 used for the measurement and can then be considered as zero. On the contrary, the current measured in *Contact* geometry reaches 7.4 μA. In both cases the current does present a variation with the applied magnetic field.

Liebing et al reported the magnetic dependence of thermocurrent in a MgO based MTJ. [78] The thermocurrent drops by 45% from P to AP state. The thermocurrent is sensitive to the magnetic configuration because it comes from the temperature gradient across the MgO barrier. In our case, there is no spin-dependent Seebeck effect across the MTJ in our system. The electrical source is related closely with Si instead of the tunneling barrier.

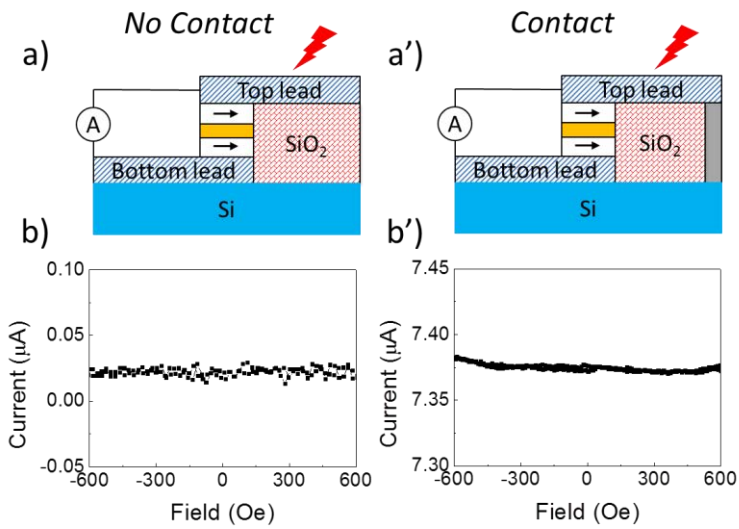

Figure 4 - 3: DC current measurement for the two geometries*. Samples No Contact (left) and Contact (right) measured at constant laser power 59mW: a) Schematic of the device in a DC current measurement configuration. b) DC current as a function of in-plane magnetic field.*

4-3 AC BEHAVOIR

Magnetic dependence

The situation is different when using a square wave modulated light. Fig. 4-4a) and a') show the lock-in measurement of AC voltage on the sample *No Contact* and *Contact*. The MTJ is powered using a laser diode shining the device at a frequency of 20 kHz and a power of 5.4 mW without any external current source. Voltage of MTJ is then measured using SR830 lock-in amplifier. The experiment setup is described in Section 2-4. The evolutions of the AC voltage as a function of the applied field are shown in Fig. 4-4b) and b'). A significant AC voltage depending on the magnetic configuration of the MTJ is observed for both *Contact* and *No Contact* geometry. Its evolution with field is again comparable to the TMR signal leading to a voltage difference between P and AP states equals around 0.2mV.

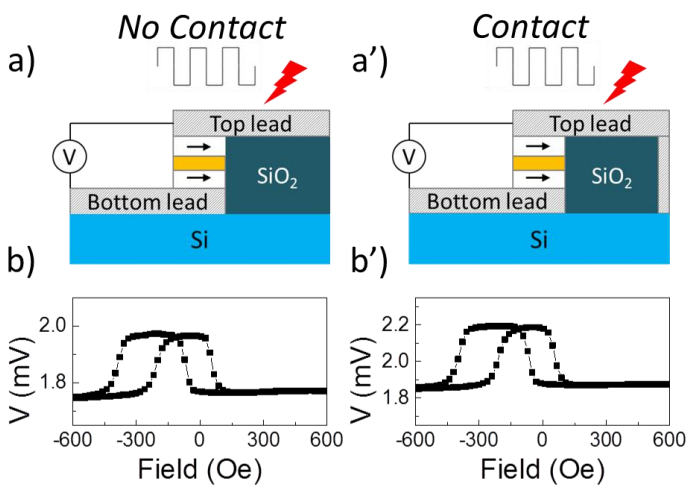

Figure 4 - 4: Lock-in AC voltage measurement for the two geometries at fixed frequency. *Samples No Contact (left) and Contact (right) are shined under 5.4 mW laser modulated by a square wave of 20 kHz. a) Schematic of the device in a AC voltage measurement configuration. b) AC voltage as a function of in-plane magnetic field.*

Frequency dependence and simulation

This AC voltage amplitude at P and AP states is also observed to strongly vary with the modulation frequency of the light as shown in Fig. 4-5a) and 5a'). The maximum AC voltage amplitude between the P and AP state is measured for a frequency close to 20 kHz (around 0.2 mV for the two geometries, the magnetic dependences are presented in Fig. 4-4). When moving toward low frequency the results are consistent with the DC results shown in previous DC voltage measurement (Fig. 4-2). In the *No Contact* geometry, the voltage is close to zero and thus does not depend on the magnetic state any more. When moving toward high frequency, the capacitance of MTJ barrier becomes important for both samples. The difference between P state and AP state is vanishing at high frequency.

Those behaviors can be mimic considering an equivalent circuit similar to the one of Fig. 4-2c) and 2c') except that two capacitors have to be added (Fig. 4-5b and 5b'). One capacitor originates from the SiO_2 insulating layer between the top lead and the substrate and the other from the tunneling barrier inside the MTJ. The experimental data in Fig. 4-5a) and 5a') are thus fitted by adjusting the values of the different resistances and capacitances. An excellent fit (solid line in Fig. 4-5a) and 5a') is obtained using the parameters shown in Table 3-1. These parameters are either obtained by a direct measurement, a simple calculation or adjusted in agreement with values from the literature. All the reported measurements can then be described by the equivalent circuits sketch on Fig. 4-5b and 5b', where the details of the generator will be discussed in the next section.

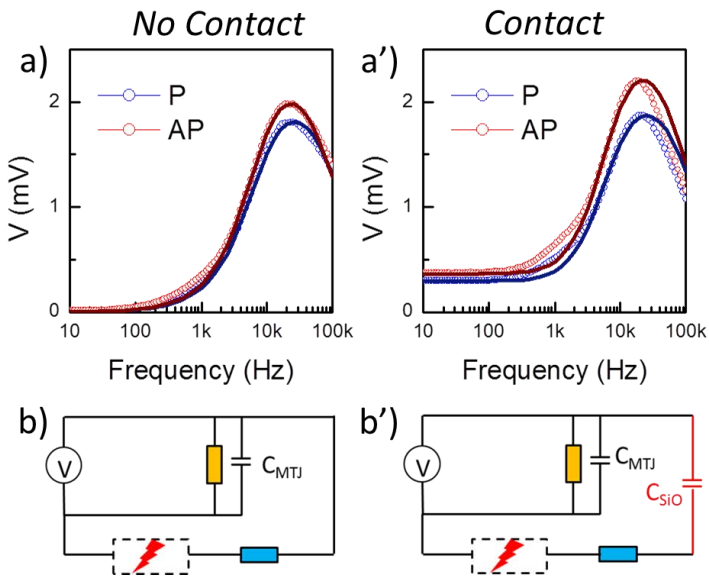

Figure 4 - 5: Frequency dependence in Lock-in AC voltage measurement. *Laser of 5.4mW is modulated by a square wave of tunable frequency. a) Frequency dependence of the AC voltage for P and AP states. Empty dots correspond to the experiment data and solid lines correspond to the fitting considering an equivalent electrical circuit. b) Sketch of the equivalent electrical circuits.*

The capacitors of MTJ, insulator that separates top lead and silicon are given by estimation using parallel-plate model. Resistance of MTJ at P and AP configurations, resistance of silicon are determined by experiments. We have no direct access to the capacitor due to the Schottky barrier, but the values are chosen to be close to the reported values [95,96]. For the sake of simplicity, the Schottky barrier has been treated as simple resistance for AC measurments.

		No Contact	*Contact*	*Source*
Capacitor of MTJ	C_{MTJ}	40pF	40pF	Estimated
Resistance of MTJ at AP	$R_{MTJ\ AP}$	20 kΩ	20 kΩ	Measured

Resistance of MTJ at P	$R_{MTJ\ P}$	16 kΩ	16 kΩ	Measured
Resistance of substrate	R_{Si}	100 kΩ	100 kΩ	Measured
Capacitor of insulator	C_{SiO}	115pF	115pF	Estimated
Capacitor of bottom SB	C_{SB1}	30pF	30pF	[96]
Resistance of bottom SB	R_{SB1}	40kΩ	40kΩ	[96]
Capacitor of top SB	C_{SB2}	-	30pF	[95]
Resistance of top SB	R_{SB2}	-	950kΩ	[95]

Table 4 - 1: Parameters to simulate the frequency dependence of Fig. 4-5a) and 5a').

It is clear that the light interacting with our sample act as an electric generator, that can be considered without loss of generality as a Norton or Thevenin generator located in the branch formed by the contact and the substrate. This is confirmed by the current measured from DC current measurement presented in Section 4-2. The AC and DC voltages reported here have similar characteristics than experimental works reporting the effect of heat on MTJ [17,18,70,78] leading to thermovoltage and thermocurrent. Those studies described the measurements in terms of pure Seebeck effect due to a temperature gradient across the tunnel barrier. In the following we confirm that a thermovoltage exists but we demonstrate that in our system, the main contribution comes from the interaction between the light and the substrate. In a context where more and more study concentrate on electron, spin transport in the presence of temperature gradient and light [17,18,70,78,97], our measurements underline other effects that should be taken into account.

Moreover those results demonstrate the possibility of using light to power a MTJ. Indeed such large photo-voltage obtained on MTJ grown on Si (with a low resistance contact from the top lead to Si) can be used to self-powered spintronic application. The photo-voltage is large enough to enable the determination of the MTJ magnetic states, in *No Contact* or *Contact* geometries, by using AC light or continuous light, respectively. In addition, this device is by nature CMOS compatible, no additional lithography or/and integration step are needed and has been electrically well characterized.

4-4 ORIGIN

In the previous simulation of AC behavoir, we assumed that there is an electric source in the circuit, without mentioning the detailed mechanism of the source. The physical origin of the giant voltage effect is still unclear. In the following, specific additional measurements demonstrate that the light-induced voltage can be described in terms of two co-existing effects: photovoltaic effect and Seebeck effect.

A first step is to consider the contribution of the light interaction with the substrate. To analyse such effect, the influence of the laser excitation (position of the laser spot, wavelength and laser power) has been studied on a simplified version of the sample. Since the electrical source is related to the Si instead of MTJ, we could remove the complex MTJ structures to simplify our experiment and analysis. Indeed we observed the effects responsible for the photo-voltages when shinning light on the substrate or/and at the interface of substrate/metal electrode.

We have studied simplified devices consisting of a Si substrate with two metallic contacts. A series of samples is made to study the origin of photovoltage: p-Si/Ta(200 nm), n-Si/Au(100 nm), n-Si/Ti(10 nm)/Au(100 nm), n-GaAs/Au(100 nm). The thin films are patterned into square contacts of 1×1 mm^2, 1.5 mm apart (center to center). The voltage is measured between these two contacts. As is described in section 2-4, voltmeter Keithley 2000 is used to record the voltage difference as the laser spot is scanned over the entire measurement window. For the detailed description of the setup, please refer to Section 2-4.

Voltage map

Fig. 4-6a) shows an optical picture of p-Si/Ta. The measurement window here is limited to $500\times1000\mu$m^2, as is sketched in Fig. 4-6a). In Fig. 4-6b), the influence of the laser spot (10μm in diameter) position compared to the leads location is presented. The voltage amplitude is the largest when the laser shines the substrate close to the leads. As we move the laser spot away from one of the leads the voltage decreases. Moreover it

is clear from Fig. 4-6b) that the signal in the middle of the contact is much weaker than the signal close to the edge. Since the structure of our sample is totally symmetric, the voltages also changes sign when we move from one lead toward the other lead. One can then conclude that the signal is maximal when the laser shines a position close to the Si/metal interface.

Therefore, the Si/Ta interface is important for the generation of voltage. Effects that are related to the metal/semiconductor interface, such as photovoltaic effect or interfacial Seebeck effect, are likely to be important for the measured voltage. From this measurement, we cannot exclude anyone of the two contributions. In the case of photovoltaic effect, the voltage amplitude depends on how many carriers can arrive to the space-charge region. The maximum voltage at the Si/Ta interface could be due to the high density of excited carriers that are excited close to the space-charge region. In the case of Seebeck effect, the interfacial temperature gradient could be high when the laser is shining at the interface, giving rise to the maximum voltage close the interface. Note that both effects are expected to decrease as the laser spot is moved away from the contact pad and change sign when the laser spot moves from one contact to the other one.

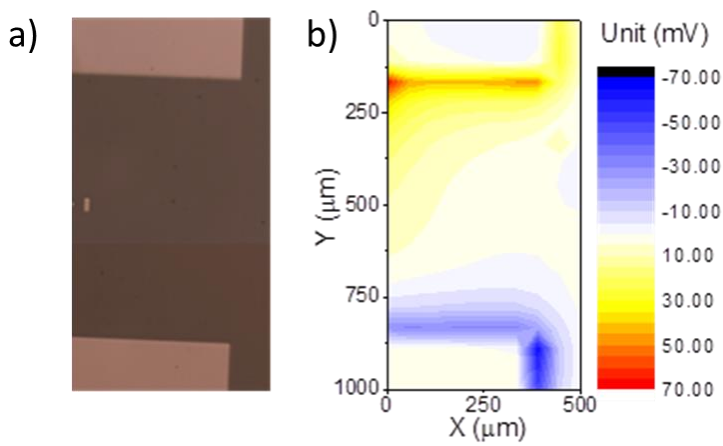

Figure 4 - 6: Spatial resolved measurement on a simplified sample. *The two contacts of Ta layer on a Si substrate are connected with a voltmeter. a) Picure of the sample. b) Evolution of*

the DC voltage measured by the voltmeter as a function of the laser spot position on the sample.

Time resolved measurement

To go deeper in understanding the light-mater interaction mechanism, time and wavelength dependences of the photo-voltage were carried out. Practically the voltage was measured in the range of several hundreds of µs after a 20 ns laser pulse excitation shined the substrate close to one of the lead for wavelength ranging from 400nm to 2200nm. Fig. 4-7a) and b) show a peak of large intensity less than 1µs after the laser pulse and a broader peak is measured for typical time of 50µs. As can be seen on Fig. 4-7a) and b), those two peaks behave differently with laser wavelength and the nature of sample holder which suggest two effects have different origins.

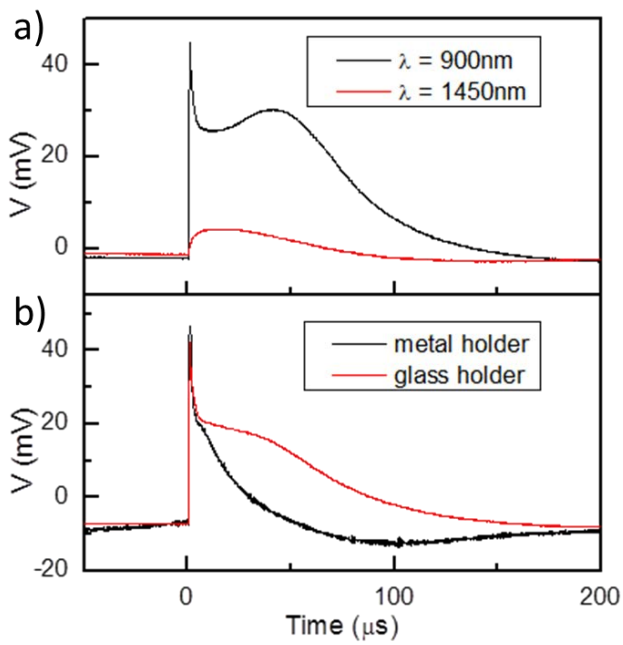

Figure 4 - 7: Time resolved measurement on a simplified sample. *a) Time resolved signal after a 20ns laser pulse of 900nm and*

1450nm for sample on a glass holder. b) Time resolved signal after a 20ns laser pulse of 750nm wavelength for sample on a metal holder and a glass holder.

Focusing on the first peak, we observe that it vanishes when the wavelength is larger than 1100nm (Fig. 4-7a) corresponding to a photon energy lower than 1.12 eV, which is the Si band gap. From these results we attribute the first peak to a photovoltaic effect. Indeed light with a photon energy larger than the gap would create electron-hole pairs that would flow through the sample. The time scale of the first peak is less than one microsecond, which is consistent with reported values. [98]

Similar behavoir can be found in other type of samples. For example, Fig. 4-8 shows complete wavelength dependence for sample n-Si/Au, which normally is a good Schottky barrier. The color in the figure stands for the voltage amplitude. The red region, which corresponds to voltage amplitude above 0.2 V, covers only the wavelength range between 800nm and 1100nm and short time duration.

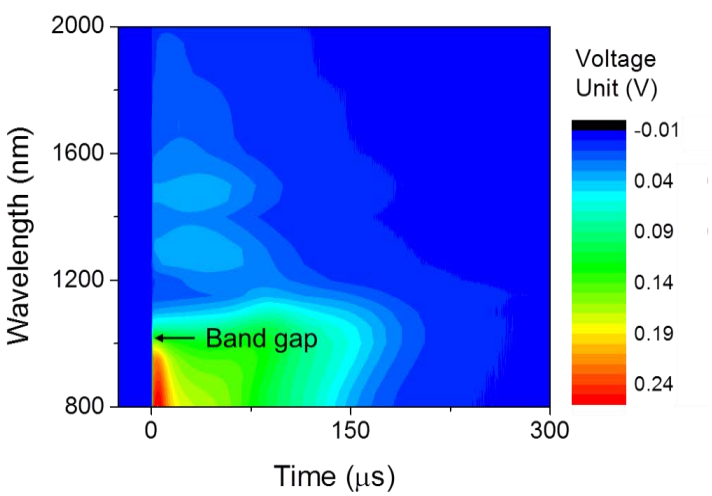

Figure 4 - 8: Wavelength dependence of time resolved signal. *Voltage between two Si/Au contacts is plotted as a function of time in the wavelength range of 800nm – 2000nm. The color stands for the amplitude of the voltage.*

The origin of the second peak in Fig. 4-7 is different. The photovoltaic effect alone is no more sufficient to explain and Seebeck effects must be included. First its intensity strongly depends on the nature of the sample holder. It decreases significantly in the case of metal holder as presented in Fig. 4-7b). Because the penetration depth of a 750nm laser is around 10μm in Si, the nature of the sample holder only influences the boundary condition of thermal propagation. The glass sample holder can be viewed as a thermal insulator, whereas the metal one has a much better heat conductivity. Consequently the metallic sample holder behaves as a heat sink, which is confirmed using COMSOL simulation (presented later in this section). This gives credit to the fact that the second peak is linked to a generated temperature gradient. We would attribute the second peak to a Seebeck effect in the Si substrate and/or Si/Ta interface. The typical time scale of this second effect is of a few tens of μs, which is consistent with thermal conductivity time scale. This is also confirmed by a finite element simulation (presented in the following). On the contrary, the characteristic of the first peak is independent on the nature of sample holder, which is in agreement with our conclusions.

The two effects generate a charge accumulation that can flow through the MTJ only if the circuit is closed, which explains the difference between the *No Contact* and *Contact* geometry. In the particular case of a photovoltaic effect a Schottky barrier is needed to separate electron-hole pair and give rise to a flowing current (avoiding recombination). Indeed if electron-hole pairs are created far from the substrate/metal interface, recombination is more likely to happen.

When we shine close to one contact, the light will create electron-hole pair and also break the symmetry of the internal electric field. We can see this effect by the disappearance of the signal when the laser shines at the middle between the two contacts. For the same reason of symmetry the temperature gradient between behave in the same way.

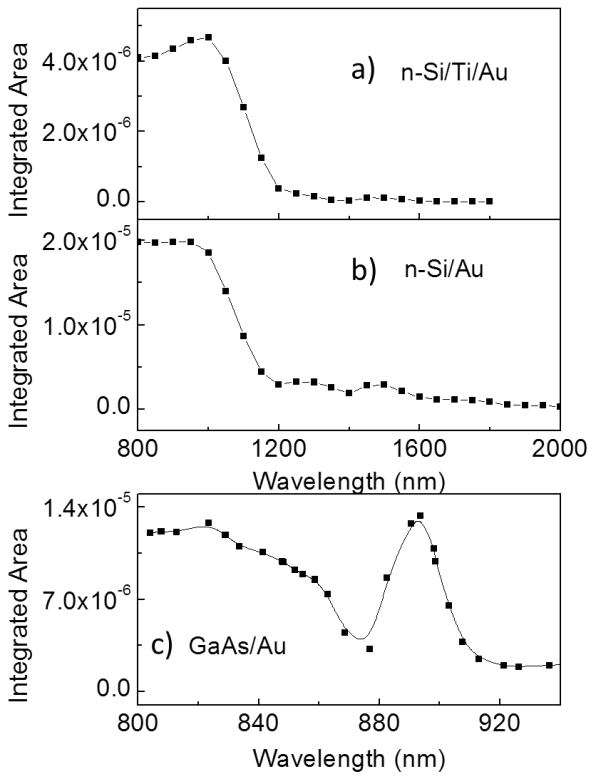

Figure 4 - 9: Wavelength dependence of integrated area of time resolved data. *a), b) and c) correspond to n-Si/Ti/Au, n-Si/Au and n-GaAs/Au, respectively. The solid line is a guide for the eye.*

To understand the role of semiconductors, we performed similar measurement on samples on n-Si substrate and n-GaAs substrate. We integrate the time resolved data to see the abosorption of semiconductor more clearly. Fig. 4-9 shows the integrated area as a function of wavelength for n-Si/Ti/Au, n-Si/Au and n-GaAs/Au. The abosorption of light in semiconductors depends on wavelength of light and the band structure of semicondcutors (direct or indirect band gap). As is shown in Secition 1-3, the absorption depth in Si is 50μm for wavelength of 900nm, and increases to 2000μm for the wavelength range of 1100nm.

This could explain the decrease of the integrated area in Fig. 4-9a) and b). Our substrate thickness is around 500μm. When the light absorption depth is greater than the substrate thickness, the absorption will decrease a lot. Fig. 4-9c) shows the wavelength dependence of GaAs sample. GaAs is known to be a direct bandgap semiconductor. Unlike the monotonous decrease of integrated area in Si, for GaAs sample we found a strong peak of absorption at around 888nm, which corresponds to the exciton energy of GaAs. The wavelength dependence of the two samples can be well understood with light absorption in semiconductors.

Simulation of heat propagation

We attributed the second peak in the time resolve measurement to Seebeck effect in silicon. While interfacial Seebeck contribution is difficult to deal with, it is possible to study the bulk Seebeck contribution through heat propagation in bulk silicon using COMSOL simulation. In the following, we simulatate the situation of heat pulse shining on Si surface or sample holder. Temperature difference of two points at the surface of silicon, which represent the two metal contacts in the sample, is then plotted as a function of time. Information about the heat propagation in bulk silicon is useful for the understanding of time-resolved data in previous experiments. Three facters will be examined to see their influences to heat propagation: spot distance, the choice of material and boundary condition.

Heat propagation in Si

In this part, the temperature evolution in Si is studied after a laser pluse shines on the surface. The geometry is shown in Fig. 4-10a), consisting of Si($4\times4\times0.5$ mm^3) and the sample holder, which is made of Cu and FR4 (insulator, commonly used for printed circuit board). The silicon size is defined to be $4\times4\times0.5$ mm^3. The laser pulse is modelled as starting condition of a hot spot in silicon. The hot spot, 0.2mm in diameter, is set to 800K as initial condition. The rest part is set to room temperature. We use convective cooling 5 $W/(m^2K)$ to mimic influence of the air. Simulation of heat propagation is performed to check the time constant for heat diffusion in the silicon substrate.

The temperature distribution at 1s is shown in Fig. 4-10b). It can be seen that the temperature is homogenous at the surface of Si. While the whole system is far from thermal equilibrium, the equilibrium in silicon has been achieved. The temperature gradient locates mainly at the boundary between Si and sample holder. This is due to the difference in diffusivity between Si (99.5 mm^2/s) and FR4 (0.384mm^2/s). The global temperature equilibrium usually needs more than 1 minute. Therefore, for heat propagation at short time scale (below 1s), the copper part which is isolated from Si by insulator FR4 plays a negligible role in heat propagation. Copper legs are neglected in the following simulation.

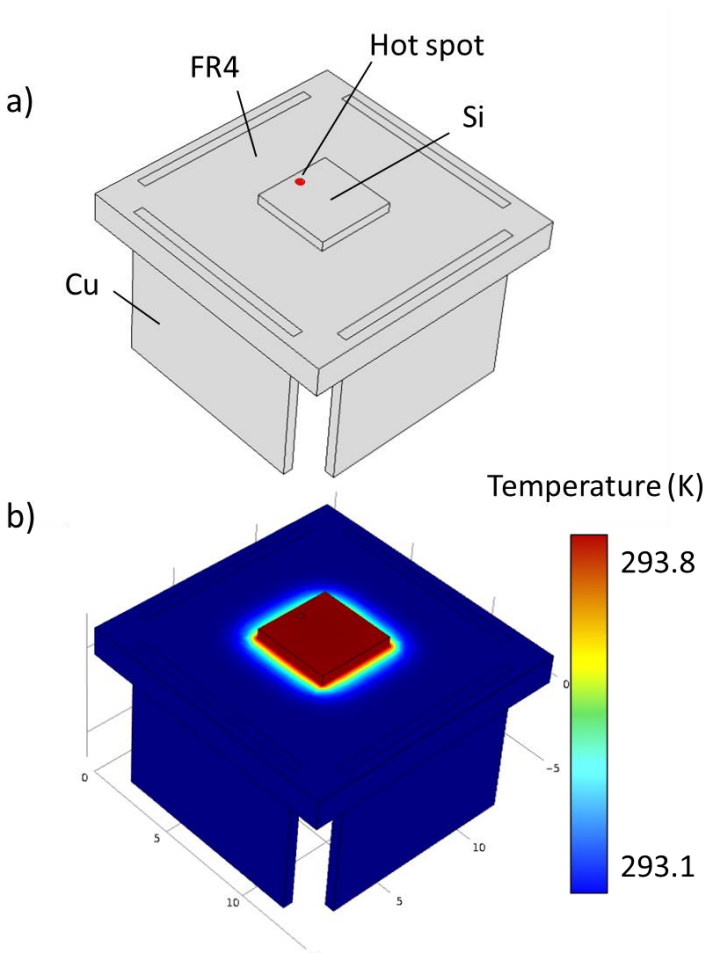

Figure 4 - 10: COMSOL simuluation of heat propagation in a mounted sample. *a) Sketch of geometry. Si(4×4×0.5 mm^3) is placed on of the sample holder, which is made of Cu and FR4. As initial condition, the red hot spot is set to 800 K and the rest is set to room temperature. b) The temperation distribution at 1s. Equilibrium has been reached in Si.*

The effect of spot distance

Now let's look at the short time scale to check the effect of spot distance. To simplify the simulation, single piece of silicon on FR4 sample holder is under consideration. The geometry of the sample is shown in Fig. 4-11b). The temperature difference (ΔT) between two points (A and B, 2mm apart) is examined and compared to the time-resolved measurement in this section.

H, A and B are three points located in a line on the surface of Si. Fig. 4-11a) shows temperature difference between the two measurement points A and B as a function of time. The arrival time of maximum temperature difference **Δ**T depends on the position of heat source. The maximum temperature difference **Δ**T arrives at 500μs when the distance is around 0.3mm. On a given material, the thermal diffusion time is largely determined by the distance. As we move the spot closer to the measurement point, the maximum **Δ**T appears sooner. As is shown in the figure, the characteristic time (See guide for the eyes) is below 100μs when the laser spot is 0.1mm away from the measurement point A. Such time scale is in agreement with the time scale of Seebeck effect found in time-resolved measurement (around 50 μs).

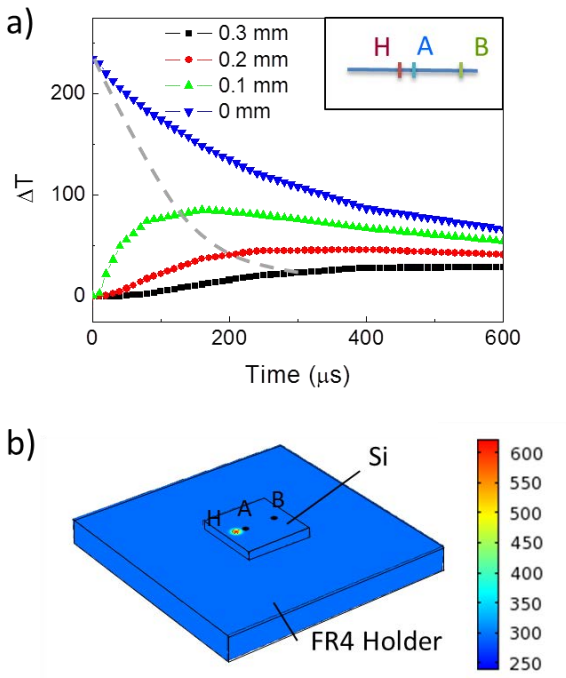

Figure 4 - 11: Lateral heat propagation in Si substrate. *a) Simulation of heat propagation in the silicon. H, A and B are three points located in a line on the surface of Si. The temperature difference (ΔT) between two points (A and B, 2mm apart) as the distance between A and the hot spot H is varied from 0mm to 0.3mm. The characteristic time for each case is shown by the dash line. b) Demonstration of heat diffusion at 100 μs. In the case of HA= 0.1mm, temperature difference between A and B reaches maximum at 100 μs.*

The effect of boundary condition

We mentioned before that the sample holder can influence the Seebeck contribution in time-resolved measurement. In this simulation, we also check two kinds of material for the sample holder (FR4 and copper) to check the influence to heat propagation. It is found that copper substrate results in quicker evacuation of heat than FR4 substrate.

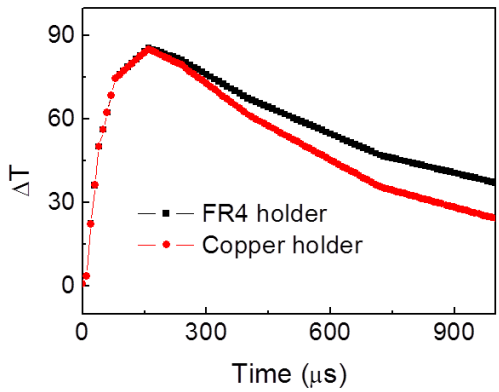

Figure 4 - 12: Influence of sample holder to heat propagation in Si. *Temperature difference as a function of time for FR4 holder (black) and copper holder (red). The spot is kept at the same position HA=0.1mm. In the case of copper holder, temperature difference ΔT decreases faster, indicating quicker evacuation of heat.*

Heat propagation is largely dominated by the thermal diffusion parameter and the heat diffusion length. In the case of FR4 holder, Si, heat diffusivity is one hundred times larger than that of holder. Therefore, the heat propagation behavior is largely dominated by the Si substrate at micro second scale. We could consider, therefore, only the thermal propagation in Si.

In the case of copper holder, the temperature difference increases at the same speed as FR4 holder in the first 170 μs, then decreases at a faster speed. 170 μs can be seen as the travel time for the heat to reach the holder. After that we need to consider the heat propagation in the perpendicular direction as well as in the lateral direction. In this case, the copper holder can be viewed as a heat sink and suppress the heat propagation in the lateral direction.

Heat propagation in insulate holder

In this part, we explore the possibility of heat propagation from holder to silicon. Same sample geometry is studied and the laser spot shines at 0.8mm from silicon. The temperature distribution at 4s is shown in Fig 4-13b). It can be seen that the temperature is almost homogenous in Si and the temperature gradient locates almost entirely inside the FR4 holder. The global temperature equilibrium needs again more than 1 minute.

Similar to the definition as before, the temperature difference between A and B is plotted against time. As is shown in Fig. 4-13a), the maximum temperature difference arrives at around 4s, which represents the heat propagation time from holder to silicon. The maximum temperature difference between the two points in Si is merely 0.07 K. The heat propagation from FR4 sample holder is very weak and can be neglected in the time-resolved measurement.

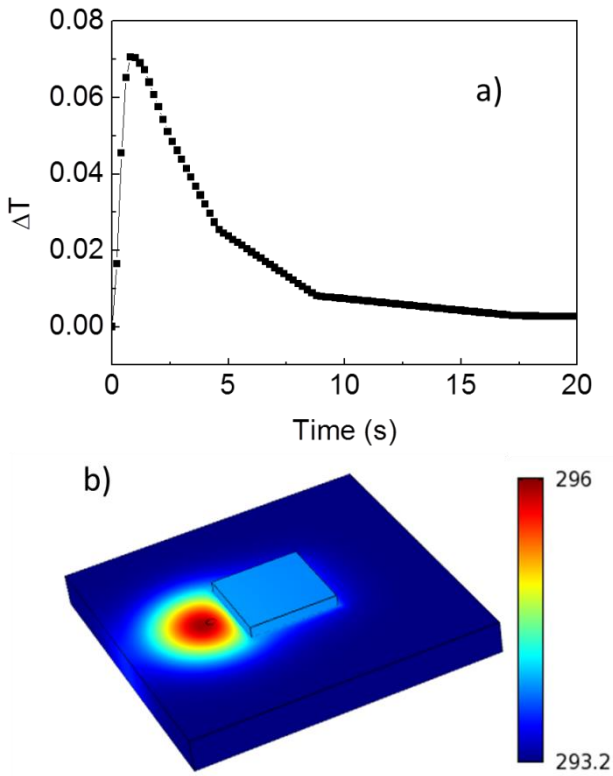

Figure 4 - 13: Heat propagation from FR4 holder to Si. *(a) Temperature difference as a function of time when hot spot is on the sample holder. (b) The temperature distribution at 4s.*

Liquid Nitrogen cooling

We argued that Seebeck effect exists in our time-resolved measurement in addition to photovoltaic effect. Seebeck contribution is studied in an indirect way using COMSOL simulation. Here we provide a primitive but direct evidence of the existence of Seebeck effect. We use liquid N_2 to creat temperature gradient in the sample to rule out the contribution from photovoltaic effect. In this way, the sample is also free from any electric noise due to electric resistance heating. In this measurement, only voltmeter is connected to the sample without any laser radiation. Liquid

N_2 was poured onto the sample to creat the temperature gradient in the sample. Fig. 4-14 shows the recorded voltage versus magnetic field during the warming up process. Similar to the result of V-H in Section 4-2, the voltage changes at different magnetic configuration.

Since no laser participated in the measurement, we could rule out the contribution of photovoltaic effect to the observed voltage. The giant voltage is created only from Seebeck effect (likely to be in semiconductor). Note here temperature gradient in Silicon substrate created by liquid N_2 could be very high, resulting in a high voltage up to 80 mV. Due to the limitation of experimental setup, for the moment we have no way to determine exactly the temperature gradient in the system.

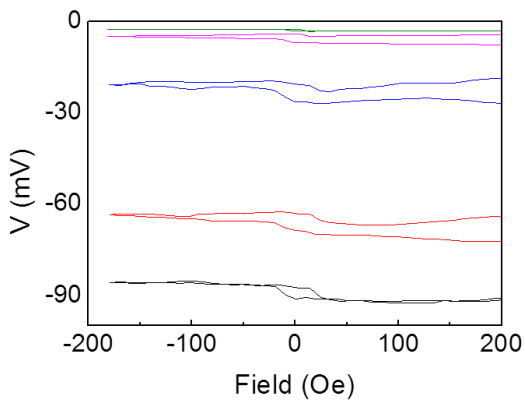

Figure 4 - 14: Liquid N_2 Measurement. *Voltage as a function of external field recorded after liquid N_2 cooling. The curves are taken during the waming up process.*

Photovoltaic effect on S/I/M

From previous discussion, one may have the impression that the interface Si/metal is the origin of the photovoltaic effect. We demonstrate here that the direct interface Si/Metal is not necessary for the photovoltaic effect.

The studied MTJ consists of a bottom reference layer Ta(5 nm)/PtMn(25 nm)/$Co_{90}Fe_{10}$(2 nm)/Ru(0.8 nm)/$Co_{90}Fe_{10}$(3 nm) and a free layer $Co_{90}Fe_{10}$(2 nm)/$Ni_{80}Fe_{20}$(5 nm)/Ru(4.8 nm)/Au(10 nm) separated by a 2 nm thick amorphous Al_2O_3 barrier, as shown in Fig. 4-15a). Measurement similar to those in Section 4-2 and 4-3 has also been performed. DC measurement (data not shown) has shown that no observable voltage can be found for DC laser power up to 200mW, which is similar to the behavior in Fig. 4-2b). Unlike the magneto-Seebeck voltage reported in literature [17,70], the Seebeck voltage induced by the temperature gradient across the Al_2O_3 barrier is negligible in our sample.

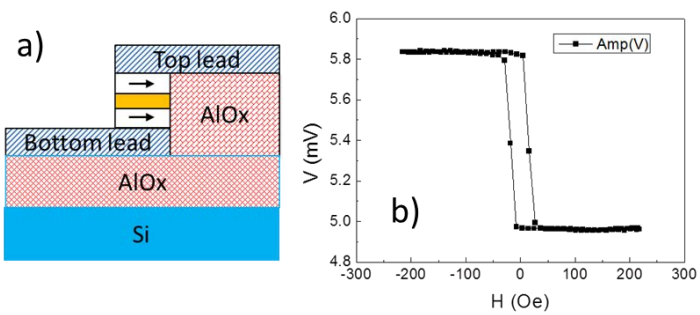

Figure 4 - 15: Laser induced voltage on Si/AlOx/MTJ structure. *a) Sketch of MTJ. Metallic multilayers are separated from silicon substrate by insulator Al_2O_3(400 nm). b) Voltage as a function of external magnetic power under AC laser power 5 mW.*

Fig. 4-15b) shows AC voltage as a function of external field under laser power of 5mW. Well defined magnetic configuration found in the figure corresponds to the parallel and antiparallel configuration, which is confirmed by the R-H measurement. Surprisingly we could measure big stable voltage even though no direct contact exists between metal layer and Si.

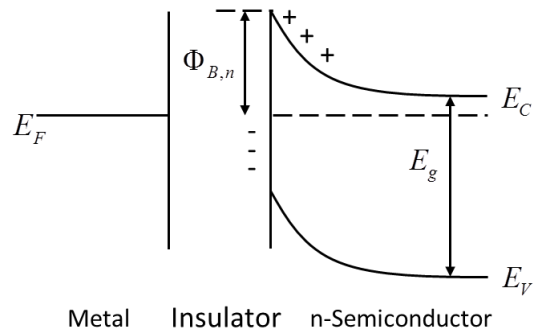

Figure 4 - 16: Explanation for photovoltaic effect of AC laser in Si/I/M contact. *In the insulator region, carriers (electrons and holes) accumulate and release at the frequency of laser power. The accumulated charges at the semiconductor interface lead to the energy band bending in Si.*

To explain the light induced voltage, the proposed mechanism is shown in Fig. 4-16. The AlOx insulate layer separating the metal and semiconductor acts as a capacitor. The alternative laser ON and laser OFF lead to the accumulation and discharging of carriers at the insulator interface. The induced carriers are at the same electrochemical potential as those in the metal layer. Due to the existence of the induced carriers, band bending in semiconductor is established and removed alternatively at the laser frequency. The band bending is responsible for the observation of light induced voltage in Fig. 4-15.

4-5 IV CURVE AND SIMULATION

From those conclusions we can now describe in more details the equivalent electrical generator. The Seebeck contribution can be viewed as a voltage source in the Si circuit and the photovoltaic effect can be described as current sources in parallel to each Schottky barrier formed by the contact between the semiconductor substrate and the bottom and

top metallic leads. Fig. 4-17 shows the complete circuit for both MTJ samples.

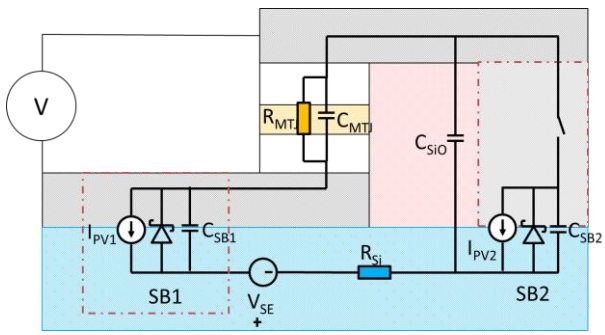

Figure 4 - 17: Schematic of the full equivalent circuit. *Photovolatic effect and Seebeck effect are taken as a current source and a voltage source, respectively. The metal contact of sample Contact is represented by the dashed box. Circuit without the dashed box corresponds to the sample No Contact.*

For the sake of simplicity, the two opposite Schottky diode can be described as only one effective Schottky diode in the small voltage limit. The simplification of electric circuit was shown in Fig. 4-18a). The two Schottky barrier (SB) generate an asymmetric electric filed which can extract from the silicon the electrons generated by the light. Note that if the two electrode contacts are symmetric and the light shined at equal distance of the two contacts no photocurrent can be created. Moreover, from an electrical point of view, it is equivalent to consider the different electrical sources as an effective current source (I_{PV}) in parallel with the effective Schottky diode as shown in Fig. 4-18a) right.

In order to analyse quantitatively the behaviour of such generator we performed measurement of I(V) curves on a contact MTJ sample for the two magnetic states and for various power intensity as shown in Fig. 4-18b) and c). The I(V) behavior of the effective source can be expressed as:

$$I_S = I_0\,[exp(\frac{eV_S}{kT}) - 1] + I_{PV},$$

in which I_0 stands for the dark saturation current of the effective Schottky diode [64], I_{PV} the light induced current, I_S and V_S stand for

the current and voltage at the level of the effective Schottky diode. Fig. 4-18b) shows I(V) curve measured for the two MTJ magnetic states (AP and P). Here the current (I) passing through the tunnel junction is measured, as the MTJ is biased with a variable DC voltage (V) and a laser is continuously shining the substrate close to the MTJ. Note that for zero voltage the current (Y-intercept) does not depend on the magnetic configuration as shown in Fig. 4-3, whereas for zero current the voltage (X-intercept) depends on the magnetic configuration (Fig. 4-2). The information in the previous DC measurement is reproduced here. It is shown again that the photo-voltage depends on the magnetic configuration and the photo-current is independent of the magnetic configuration.

The curves can be described as the sum of a linear part with an offset and a deviation from the linearity. The linear behaviour is essentially due to the Ohmic behaviour of the substrate and of the MTJ. The two different slopes for P and AP are due to the two different resistance values of the two states. The offset comes from the equivalent current source due to the laser shining. The deviation from the linearity is due to non-linear behavior of the effective Schottky diode.

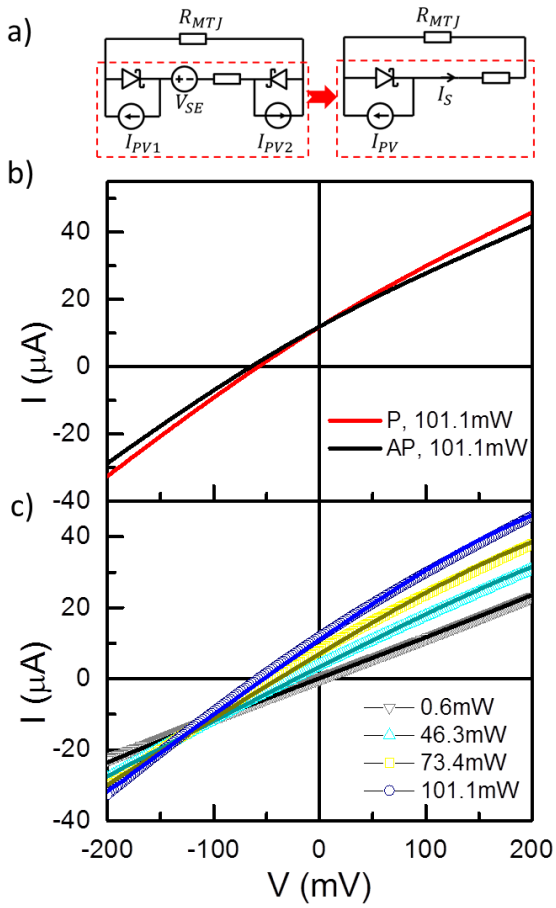

Figure 4 - 18: Measurement and simulation of IV curves under different power. *a) Sketch of the electric circuit used to model the I(V) curves, in which I_{PV} , V_{SE} stand for the photovoltaic current and Seebeck voltage. The two sources are equivalent to an effective Schottky barrier, of which the photo generated current is given by $I_{PV'}$. b) I(V) curves for P and AP magnetic configuration obtained on a Contact geometry device. c) I(V) for the P magnetic configuration for different laser power.*

On Fig. 4-18c) the evolution of the I(V) curves for different light power are presented while the MTJ is kept in the P magnetic state by applying an external field. As is shown here, the IV curve crosses the zero point under low laser power and the IV curves deviates from the zero point at increasing laser power. Here is a transition from pure passive element to an active source for the sample. As the laser power increases, the photo-voltage and photo-current increases.

Another feature that we can observe in Fig. 4-18c) is a convergent point for a bias voltage around -100mV independent of the laser power. This point depends on the asymmetry between the two SBs described above. At this bias point, the electrical field inside the Si substrate becomes symmetric, and consequently the electron generated by the light can no longer contribute to a net current flow in the circuit.

Simulation of the IV curves takes into account a effective Schottky barrier, the resistance of silicion substrate and the MTJ. Under laser radiation, the Schottky barrier can be view as an electrical source, with a current source in parallel to the Schottky barrier. The current in the substrate branch can be expressed as:

$$I_S = I_0 \left[\exp\left(\frac{eV_S}{kT}\right) - 1 \right] + I_{PV}.$$

Thus the total voltage V and current I are expressed using the voltage of Schottky barrier V_S as a parameter:

$$V = V_S + I_S R_{Si}$$

$$I = \frac{V_S + I_S R_{Si}}{R_{MTJ}} + I_S$$

At increasing laser power, the resistance of silicon is decreasing and the photocurrent of the effective is inceasing. Values for resistance of silicon at different laser power are extracted from the IV curves. The photocurrent is optimized to reproduce the IV curve. The values of silicon resistance and photocurrent are list in Table 4-2. With these parameters, the I(V) data of different laser power are perfectly fitted by the expression above.

Laser power	R_{Si}(kΩ)	I_{PV}(μA)
200	8.7	23.3
180	9.5	18
160	12.3	15.7

140	14.3	12.8
120	22	8.7
100	33	5.7
80	44	4.7
60	100	0.8
40	150	0

Table 4 - 2: Resistance of Si and photocurrent at different laser power used in fitting.

Note in all the laser power, the values of I_0 is kept constant. This value is directly linked to the barrier hight of the effective Schottky barrier: $I_0 \propto exp(-\Phi_B/kT)$, as is shown in Section 1-3. Although it is difficult to vary the barrier high experimentally, it can be varied easily in simulation to check its influence. For example, if we set I_0 to 100nA, IV curve is shown in Fig. 4-19a). Clearly the converging point of the IV curves has been shifted toward higher voltage. We set this value to 100nA, 375nA, 700nA and 1000nA and we can get four converging points, plotted in Fig. 4-19b). The four points can be fitted perfectly using a exponential equation: $Is = 4.34 \times 10^{-5} \exp(-40.5V)$. This equation provides a way to access the height of the effective Schottky barrier. This can be seen as an auxiliary proof the simulation of the IV curves.

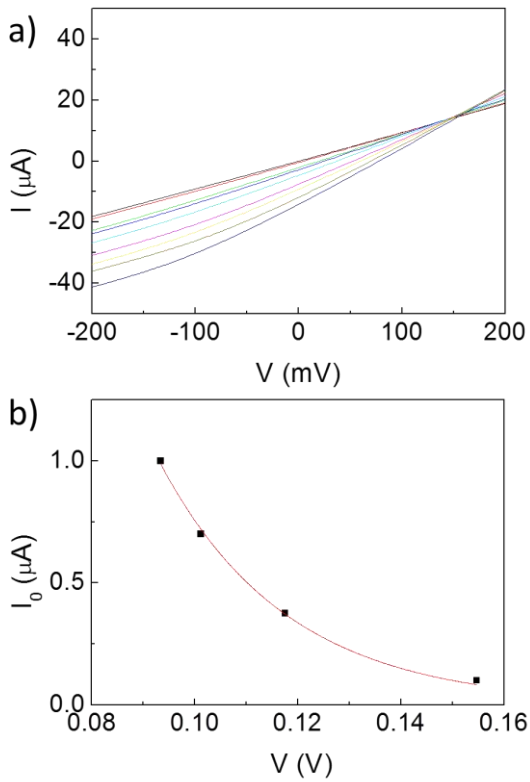

Figure 4 - 19: Simulation of IV curves with different Schottky barrier height. *a) Simulated IV curves when the I_0 is set to 100nA. b) Four black dots are the converging points in four IV curve simulation. The red line is fitting using: $I_0 \propto exp(-\Phi_B/kT)$.*

4-6 SUMMARY

In conclusion we have demonstrated that the magnetic configuration inside an MTJ can be probed using light shining on the device and without any other external source. A voltage is actually measured using a

continuous or pulse light. The light acts as an additional generator and the system (sample + light) response can be modeled by an equivalent electrical circuit. Since magnetization manipulation using pulsed light has also been demonstrated this new degree of freedom could lead to All Optical powered spintronic devices. By growing model system on various substrates and using continuous and pulse laser we propose two different origins for the photo generated voltage. First a photovoltaic effect that can be detected in the structures if a semiconductor substrate is used. The effect would rise from the creation of electron–hole pairs which leads to charge propagation through the magnetic tunnel junction if a Schottky barrier is formed between the substrate and the lead. Such signal is found to vanish once the light's wavelength reaches a critical value (1100 nm for Si) which corresponds to the energy band gap inside the semiconductor. Secondly a Seebeck effect could also be detected originating from a temperature gradient between the two parts of the electrical circuit formed by the MTJ, the leads, the substrate and the insulator. We are able to fully describe the electrical behavior of the devices and we have highlighted the different key parameters that govern the latter.

The possibility of reading the magnetic configuration of an MTJ (based element of any spintronic application) opens new applications in magnetic memory, logic, processing and sensor. Indeed given the current trends for silicon nanophotonics, this photovoltaic + Seebeck effect added to the all optical magnetization reversal offer the ability to couple photonic, and spintronic opening a new field that can be called "optical-spintronic".

In this chapter we report on the presence of thermomagnetic effect in our devices when using a glass substrate. In this particular case the effects described in Chapter 4 vanish.

5-1 GEOMETRY AND MEASUREMENT

Fig. 5-1 shows the geometry of our experimental setup. A multilayer structure: Ta (5nm)/Co (10nm)/IrMn (7.5nm)/Co (4nm)/Al_2O_3 (2nm)/Co (10nm)/Pt (5nm) has been patterned using UV lithography. The upper layers Al_2O_3/Co/Pt acts as an electrode while a laser shines the lower layers, namely Ta/Co/IrMn/Co. In this geometry, the thermal gradient is perpendicular to the film plane.

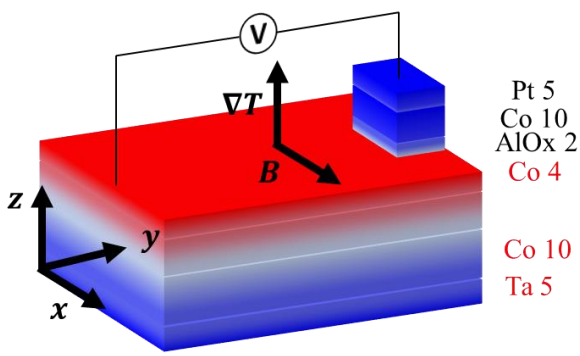

Figure 5 - 1: Sketch of Anomalous Nernst voltage measurement in the multilayer structure. *Red and blue correspond to hot and cold region, respectively. Temperature gradient ∇T is applied perpendicular to the film plane and magnetic field B is applied in-plane. The xyz coordinate system shown here will be used in the following discussion.*

The electrical measurements presented in the following are done in an open circuit geometry (considering an infinite impedance of the used lock-in amplifier). An in-plane magnetic field is applied while recording the voltage developed between the top and bottom electrodes. The Fig. 5-

2 c) presents the measured voltage as a function of the magnetic field. We should note here that the magnetic field is applied along the easy axis of magnetization of all ferromagnetic layers so that the measured voltage, the thermal gradient and the magnetizations are all orthogonal to each other. It is here striking to note that the signal resemble a M(H) loop in which two magnetic hysteresis are present. According to both their switching fields and bias fields it is possible to identify which magnetic layers are leading to the recorded effect. Surprisingly the two ferromagnetic we identify as responsible for the voltage changes are the ones present in the bottom electrode. Since no hysteretic signal correspond to top electrode Al_2O_3/Co/Pt we can rule out any effect implying the magnetic junction Co/Al_2O_3/Co/Pt. Note that we have check the integrity of the MTJ before and after all the measurements presented in this chapter. This proves that we are probing only a voltage and not a conductance variation because if there is a leakage current, it should tunnel through the MTJ and the hysteretic signal corresponding to the top electrode Al_2O_3/Co/Pt should appear.

Considering that magnetic layers, thermal gradient, and voltage measurement are involved in the effect we are interpreting the data in the framework of a thermomagnetic effect taking place in the bottom electrode. In this geometry the phenomenology of the anomalous Nernst effect states that an electrical field $\boldsymbol{E_y}$ proportional to the component of magnetization $\boldsymbol{m_x}$ orthogonal to both the thermal gradient $\frac{\partial T}{\partial z}$ and the direction defined by the voltage probes is to be expected:

$$\boldsymbol{E_y} = -Q_{AN}^{\perp}\boldsymbol{m_x}\frac{\partial T}{\partial z}.$$

This equation is derived from the last equation presented in Section 1-2 considering the acting thermal gradient has only z component. So in this framework we can explain why the recording signal resemble M(H) loops.

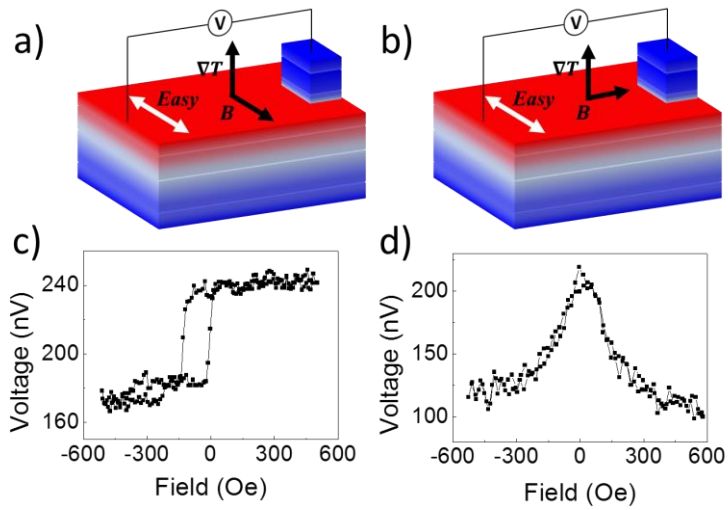

Figure 5 - 2: Sketch of Nernst voltage perpendicular to the easy axis. *Magnetic field is applied in the easy axis (left) and hard axis (right), (a) and (b) show the measurement configuration. Voltage as a function of external field in the easy axis and hard axis are shown in c and d.*

To check a bit further the validity of our interpretation we have applied the magnetic field perpendicularly to the easy axis of the magnetization. The recorded signal as well as the geometry is presented in Fig. 5-2 b) and d). For high magnetic fields, in absolute values, the magnetization is almost aligned with the magnetic field in the (y) direction: $\boldsymbol{m_x \approx 0}$. This is associated with a minimum value of the recorded voltage $\boldsymbol{E_y}$. When, again in absolute value, the magnetic field decreases and goes to zero, the magnetization progressively aligns itself in the easy direction of magnetization and thus $\boldsymbol{m_x}$ increases. This corresponds to an increase of voltage. Again the observed voltage variation with the magnetic field could be explained by taking into account the anomalous Nernst effect in the bottom electrode. At this point it is important to note that the only discrepancy with our interpretation is the existence of an offset voltage. Indeed the signal $\boldsymbol{E_y}$ should drop to zero volt along with cancelation of the $\boldsymbol{m_x}$ component of magnetization. This voltage offset is probably due to classical Seebeck effects taking place in the whole stack as discussed afterward.

In a second step we have prepared an almost identical sample expect that this time the easy axes of magnetization is aligned along the direction defined by the voltage probes. With this new device, we have repeated the two previous experiments: either the magnetic field is applied along the voltage probes (Fig. 5-3a) or perpendicularly to the voltage probes direction (Fig. 5-3b). The thermomagnetic voltages measured as function of the applied field are presented in Fig. 5-3c) and d). In the first case (magnetic field parallel to both the voltage probes and the easy axes magnetization) no signature resembling to an M(H) loop is to be excepted with regard to the previous equation. Indeed whatever the value of the applied field the $\boldsymbol{m_x}$ component of magnetization should remain equals to zero (we neglect in this analysis any $\boldsymbol{m_x}$ component due to a magnetic domain wall). Experimentally no signal having a magnetic signature is recorded in this configuration (see data presented in Fig. 5-3c). The variation of the observed signal is attributed here to some drift (probably thermal drift) since when sweeping the magnetic field back and forth the recorded voltages does not overlap at the end of the sweep). In the last case, magnetic field perpendicular to both the easy axis of magnetization and to the voltage probes direction, we expect to observe a signal resembling a classical hard axis magnetization loop. This is indeed the case in this experiment (see data presented in Fig. 5-3d). So, all the observed behaviors (four geometries of measurement) can be interpreted by considering that we are measuring an anomalous Nernst effect taking place in the bottom electrode of our devices.

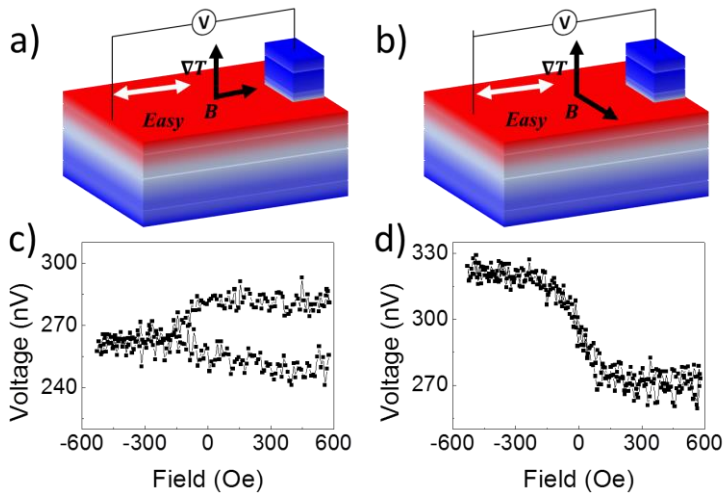

Figure 5 - 3: Sketch of Nernst voltage parallel to the easy axis. *Magnetic field is applied in the easy axis (left) and hard axis (right), (a) and (b) show the measurement configuration. Voltage as a function of external field in the easy axis and hard axis are shown in (c) and (d).*

5-2 THERMAL TRANSFER IN MAGNETIC NANOSTRUCTURE

In order to get deeper in the understanding of the different effects that can appear in our samples, we check the effect of the repetition frequency of the laser on the amplitude of the anomalous Nernst signal. We also check the evolution of the phase of the lock-in signal and surprisingly we found a replica of the amplitude signal when sweeping the field.

Effect of the excitation frequency

From Fig. 5-4, we can see that the amplitude of the loop due to the magnetization reversal of the bottom Co layer is reduced when the frequency increase. It is also the case for the offset voltage.

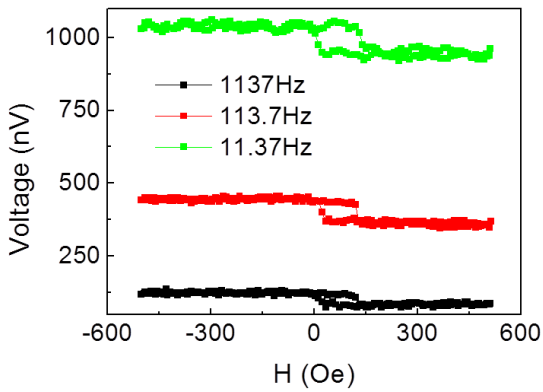

Figure 5 - 4: Voltage as a function of field at different frequency. *The offset voltage and Nernst voltage increase as the frequency decreases.*

At this point it is important to discuss about this offset. We attribute it to the thermovoltage due to all the asymmetric interfaces between the different layers in contact (namely thermocouple effect). To verify this hypothesis we check that this voltage is directly linked to the temperature of the room. We also test other stacks and find that the thermovoltaic offset depends on the latter. In conclusion this offset come from the thermocouple formed by the different interfaces of the stack [99].

The fact that the ANE and the thermocouple voltage decrease with the frequency can be understood as follows. The heat propagation time is given by the heat capacitances and the conductivities of the different layers, and their associated interfaces. In a simple approximation we can considered that it behaves as a RC filter with the following characteristic time constant $\frac{C_p}{k}$, C_p and k are effective values that describe the whole stack, without loss of generality. In this context, when the frequency of

the excitation is too fast, the equivalent capacitor has not the time to fully discharge. Then the mean temperature of the sample increases, but the variation around this mean value decreases. This leads to the observed decrease of the ANE and thermocouples voltage measured by the lock-in.

Evolution of the phase signal

A very intriguing point is that the variation of the ANE voltage is replicated in the phase, which is not expected (Fig. 5-5). Because there is no change in electrical resistance when the bottom Co layer reverse, any change of electrical RC circuit can occur. In consequence, this variation in the phase cannot be attributed to electrical effect.

For the moment this effect is again under investigation. We propose a possible explanation based on the Co/IrMn interface. The thermal interfacial resistance associated to it could depend on the relative magnetic orientation between the last spin plane of the IrMn antiferromagnetic layer and the adjacent Co layers similarly to the thermogalvanic voltage effect reported by L. Gravier et al [100]. To go deeper in this investigation more data sets are required. First measuring systemically the offset, the ANE amplitudes and the phase as a function the laser repetition frequency could reveals an unexpected phase change between the offset voltage and the ANE. In a second step swapping the IrMn layer with a non-magnetic layer such as Ta should allow us to unveil the role played by the F/AF interface.

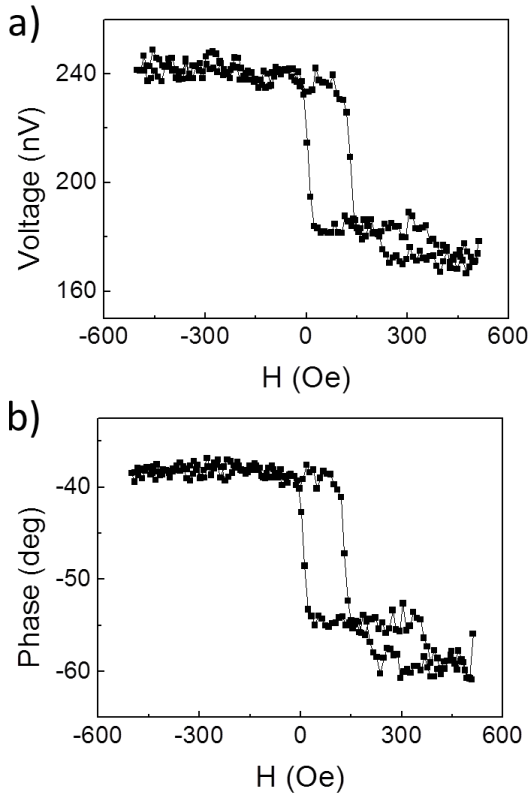

Figure 5 - 5: The amplitude and phase of Nernst voltage as a function of field. *Both the amplitude (a) and phase (b) depend on the magnetic configuration.*

5-3 SUMMARY

We report the observation of anomalous Nernst voltage. The voltage is measured with external magnetic field applied along or perpendicular to the easy axis. The voltage versus magnetic field can be explained using

anomalous Nernst effect. This conclusion is further confirmed by the behavior of another sample, of which the easy axis is along the voltage direction (y direction). Since the Nernst voltage is proportional to the temperature gradient at given magnetization direction, we investigate the heat propagation in multilayer system, for example the frequency dependence. The explanation of the phase change at different magnetic configuration may need to consider thermal conductivity for spin polarized electrons. More experiment data is needed to support this explanation.

In this thesis, we have demonstrated that the magnetic configuration inside an MTJ can be probed using light shining on the device without any other external source. Two types of MTJs with Al_2O_3 tunnel barrier were fabricated on Si substrates: with and without intended leakage from the top contact to Si substrate. An open voltage across the MTJ up to mV can be measured, which depends on the magnetic configuration (parallel or antiparallel). To explore the origin of this voltage, we have done the following study:

1. The response of voltage with DC continuous light and AC pulsed light. We have model the whole system as equivalent electrical circuit, which can well reproduce the voltage *vs.* AC frequency curves. Our model can also fit the MTJ IV curves with light;

2. Time-resolved study of the voltage response with *ns* pulse laser. Two peaks are found to contribute to the measured voltage signal. One peak with short response time (~ns) is due to the photo-voltaic effect rising from the creation of an electron–hole pair in Si which leads to charge propagation through the magnetic tunnel junction when a Schottky barrier is formed between the substrate and the lead. The other peak with long response time (~μs) is attributed to the Seebeck effect due to the light generated temperature gradient in the whole system;

3. Spatial-resolved study of the voltage response. This study allow us clearly observe that the maximum voltage is obtained when we shine the light at the edge of the electrode, while it is much reduced when the light is shined in the middle between MTJ two electrodes.

4. We report the observation of anomalous Nernst effect and we investigate the thermal propagation in multilayer system using Nernst voltage as tool.

PROSPECTIVE:

Optimization the efficiency of Schottky solar cell

Since the open voltage across the MTJ is proportional to the density of light generated photocurrent, the efficiency of the Schottky solar cell could be optimized by choosing appropriate metals on different semiconductor substrates (Si, GaAs, Ge….). In addition, a special designed p-n junction solar cell can be also employed to power the MTJ to enhance the spatial light absorption efficiency.

Study spin photocurrent with ferromagnetic contact

As a large part of this thesis has been contributed to study the Schottky property of metal-semiconductor contact with light, it will be a great interesting to continue extending this study on the interlayer of circular polarized light with ferromagnetic contact on semiconductor. The study the spin-dependent photocurrent will be an inversed process compared to spin-LED, which uses the ferromagnetic contact to inject spin-polarized current to emit circular polarized light.

Study anomalous Nernst effect in different ferromagnetic thin films

In this thesis, we have studied Nernst effect in MTJ structure. The lithography design is not suitable to define the temperature gradient in the structure. To resolve this problem, we have to make a new design with Hall bar shape of electrodes. With the new designed structure, we expect to study the Nernst effect in different ferromagnetic thin films with different magnetization (in-plan or perpendicular). This will allow us to well understand the

dependence of Nernst voltage *vs.* temperature gradient and magnetization direction.

[1] C. Chappert, A. Fert, and F. N. Van Dau, Nat. Mater. **6**, 813 (2007).
[2] S. A. Wolf, D. D. Awschalom, R. A. Buhrman, J. M. Daughton, S. von Molnár, M. L. Roukes, A. Y. Chtchelkanova, and D. M. Treger, Science **294**, 1488 (2001).
[3] J. M. Slaughter, in *Device Res. Conf. 2007 65th Annu.* (2007), pp. 245–246.
[4] ITRS, http://public.itrs.net/
[5] M. N. Baibich, J. M. Broto, A. Fert, F. N. Van Dau, F. Petroff, P. Etienne, G. Creuzet, A. Friederich, and J. Chazelas, Phys. Rev. Lett. **61**, 2472 (1988).
[6] M. Julliere, Phys. Lett. A **54**, 225 (1975).
[7] J. C. Slonczewski, J. Magn. Magn. Mater. **159**, L1 (1996).
[8] H. Riahi, *Propriétés Du Réseau Kagomé Artificiel : Micromagnétisme, Chiralités et Cristaux de Charges Émergents* (Université de Lorraine, 2013).
[9] I. Žutić, J. Fabian, and S. Das Sarma, Rev. Mod. Phys. **76**, 323 (2004).
[10] B. Van Waeyenberge, A. Puzic, H. Stoll, K. W. Chou, T. Tyliszczak, R. Hertel, M. Fähnle, H. Brückl, K. Rott, G. Reiss, I. Neudecker, D. Weiss, C. H. Back, and G. Schütz, Nature **444**, 461 (2006).
[11] W.-G. Wang, M. Li, S. Hageman, and C. L. Chien, Nat. Mater. **11**, 64 (2012).
[12] T. A. Ostler, J. Barker, R. F. L. Evans, R. W. Chantrell, U. Atxitia, O. Chubykalo-Fesenko, S. El Moussaoui, L. Le Guyader, E. Mengotti, L. J. Heyderman, F. Nolting, A. Tsukamoto, A. Itoh, D. Afanasiev, B. A. Ivanov, A. M. Kalashnikova, K. Vahaplar, J. Mentink, A. Kirilyuk, T. Rasing, and A. V. Kimel, Nat. Commun. **3**, 666 (2012).
[13] I. M. Miron, K. Garello, G. Gaudin, P.-J. Zermatten, M. V. Costache, S. Auffret, S. Bandiera, B. Rodmacq, A. Schuhl, and P. Gambardella, Nature **476**, 189 (2011).
[14] C.-H. Lambert, S. Mangin, B. S. D. C. S. Varaprasad, Y. K. Takahashi, M. Hehn, M. Cinchetti, G. Malinowski, K. Hono,

Y. Fainman, M. Aeschlimann, and E. E. Fullerton, Science 1253493 (2014).
[15] S. Mangin, M. Gottwald, C.-H. Lambert, D. Steil, V. Uhlíř, L. Pang, M. Hehn, S. Alebrand, M. Cinchetti, G. Malinowski, Y. Fainman, M. Aeschlimann, and E. E. Fullerton, Nat. Mater. **13**, 286 (2014).
[16] C. D. Stanciu, F. Hansteen, A. V. Kimel, A. Kirilyuk, A. Tsukamoto, A. Itoh, and T. Rasing, Phys. Rev. Lett. **99**, 047601 (2007).
[17] W. Lin, M. Hehn, L. Chaput, B. Negulescu, S. Andrieu, F. Montaigne, and S. Mangin, Nat. Commun. **3**, 744 (2012).
[18] M. Walter, J. Walowski, V. Zbarsky, M. Münzenberg, M. Schäfers, D. Ebke, G. Reiss, A. Thomas, P. Peretzki, and M. Seibt, Nat. Mater. **10**, 742 (2011).
[19] N. F. Mott, Proc. R. Soc. Lond. Ser. - Math. Phys. Sci. **156**, 368 (1936).
[20] A. Fert and I. A. Campbell, Phys. Rev. Lett. **21**, 1190 (1968).
[21] G. Binasch, P. Grünberg, F. Saurenbach, and W. Zinn, Phys. Rev. B **39**, 4828 (1989).
[22] S. S. P. Parkin, Z. G. Li, and D. J. Smith, Appl. Phys. Lett. **58**, 2710 (1991).
[23] N. Locatelli, V. Cros, and J. Grollier, Nat. Mater. **13**, 11 (2014).
[24] B. Dieny, V. S. Speriosu, B. A. Gurney, S. S. P. Parkin, D. R. Wilhoit, K. P. Roche, S. Metin, D. T. Peterson, and S. Nadimi, J. Magn. Magn. Mater. **93**, 101 (1991).
[25] B. Dieny, V. S. Speriosu, S. Metin, S. S. P. Parkin, B. A. Gurney, P. Baumgart, and D. R. Wilhoit, J. Appl. Phys. **69**, 4774 (1991).
[26] D. L. L. Mills and J. A. C. Bland, *Nanomagnetism: Ultrathin Films, Multilayers and Nanostructures* (Elsevier, 2006).
[27] K. H. J. Buschow, *Handbook of Magnetic Materials* (Elsevier, 2003).
[28] J. S. Moodera, L. R. Kinder, T. M. Wong, and R. Meservey, Phys. Rev. Lett. **74**, 3273 (1995).
[29] J. C. Slonczewski, Phys. Rev. B **39**, 6995 (1989).

[30] F. Montaigne, M. Hehn, and A. Schuhl, Phys. Rev. B **64**, 144402 (2001).
[31] D. Wang, C. Nordman, J. M. Daughton, Z. Qian, and J. Fink, IEEE Trans. Magn. **40**, 2269 (2004).
[32] W. H. Butler, X.-G. Zhang, T. C. Schulthess, and J. M. MacLaren, Phys. Rev. B **63**, 054416 (2001).
[33] J. M. MacLaren, X.-G. Zhang, W. H. Butler, and X. Wang, Phys. Rev. B **59**, 5470 (1999).
[34] J. Mathon and A. Umerski, Phys. Rev. B **63**, 220403 (2001).
[35] S. Yuasa, T. Nagahama, A. Fukushima, Y. Suzuki, and K. Ando, Nat. Mater. **3**, 868 (2004).
[36] S. S. P. Parkin, C. Kaiser, A. Panchula, P. M. Rice, B. Hughes, M. Samant, and S.-H. Yang, Nat. Mater. **3**, 862 (2004).
[37] S. Yuasa and D. D. Djayaprawira, J. Phys. Appl. Phys. **40**, R337 (2007).
[38] R. Matsumoto, A. Fukushima, T. Nagahama, Y. Suzuki, K. Ando, and S. Yuasa, Appl. Phys. Lett. **90**, 252506 (2007).
[39] J. Faure-Vincent, C. Tiusan, C. Bellouard, E. Popova, M. Hehn, F. Montaigne, and A. Schuhl, Phys. Rev. Lett. **89**, 107206 (2002).
[40] P.-J. Zermatten, G. Gaudin, G. Maris, M. Miron, A. Schuhl, C. Tiusan, F. Greullet, and M. Hehn, Phys. Rev. B **78**, 033301 (2008).
[41] F. Greullet, C. Tiusan, F. Montaigne, M. Hehn, D. Halley, O. Bengone, M. Bowen, and W. Weber, Phys. Rev. Lett. **99**, 187202 (2007).
[42] L. Berger, Phys. Rev. B **54**, 9353 (1996).
[43] C. O. Avci, K. Garello, I. M. Miron, G. Gaudin, S. Auffret, O. Boulle, and P. Gambardella, Appl. Phys. Lett. **100**, 212404 (2012).
[44] M. Cubukcu, O. Boulle, M. Drouard, K. Garello, C. O. Avci, I. M. Miron, J. Langer, B. Ocker, P. Gambardella, and G. Gaudin, Appl. Phys. Lett. **104**, 042406 (2014).
[45] L. Liu, T. Moriyama, D. C. Ralph, and R. A. Buhrman, Phys. Rev. Lett. **106**, 036601 (2011).

[46] L. Liu, C.-F. Pai, Y. Li, H. W. Tseng, D. C. Ralph, and R. A. Buhrman, Science **336**, 555 (2012).
[47] R. D. Barnard, *Thermoelectricity in Metals and Alloys* (Taylor & Francis London, 1972).
[48] K. Uchida, S. Takahashi, K. Harii, J. Ieda, W. Koshibae, K. Ando, S. Maekawa, and E. Saitoh, Nature **455**, 778 (2008).
[49] T. Yang, T. Kimura, and Y. Otani, Nat. Phys. **4**, 851 (2008).
[50] D. Ilgaz, J. Nievendick, L. Heyne, D. Backes, J. Rhensius, T. A. Moore, M. Á. Niño, A. Locatelli, T. O. Menteş, A. v. Schmidsfeld, A. v. Bieren, S. Krzyk, L. J. Heyderman, and M. Kläui, Phys. Rev. Lett. **105**, 076601 (2010).
[51] R. Tolley, T. Liu, S. Le Gall, Y. Xu, M. Gottward, T. Hauet, M. Hehn, F. Montaigne, E. Fullerton, and S. Mangin, unpublished.
[52] J.-C. Le Breton, S. Sharma, H. Saito, S. Yuasa, and R. Jansen, Nature **475**, 82 (2011).
[53] A. Slachter, F. L. Bakker, J. P. Adam, and B. J. Van Wees, Nat. Phys. **6**, 879 (2010).
[54] Y. Takezoe, K. Hosono, A. Takeuchi, and G. Tatara, Phys. Rev. B **82**, 094451 (2010).
[55] I. L. Prejbeanu, M. Kerekes, R. C. Sousa, H. Sibuet, O. Redon, B. Dieny, and J. P. Nozières, J. Phys. Condens. Matter **19**, 165218 (2007).
[56] L. I. Anatychuk, *Physics of Thermoelectricity*, 1ST edition (Institute of Thermoelectricity, 1998).
[57] D. M. Rowe, Appl. Energy **40**, 241 (1991).
[58] T. M. Tritt and M. Subramanian, MRS Bull. **31**, 188 (2006).
[59] O. Madelung, *Introduction to Solid-State Theory* (Springer Science & Business Media, 1996).
[60] T. R. McGuire and R. I. Potter, IEEE Trans. Magn. **11**, 1018 (1975).
[61] J. Mundo-Hernández, B. de Celis Alonso, J. Hernández-Álvarez, and B. de Celis-Carrillo, Renew. Sustain. Energy Rev. **31**, 639 (2014).
[62] P. Chattopadhyay, Solid-State Electron. **31**, 1641 (1988).
[63] S. M. Sze, *Modern Semiconductor Device Physics* (Wiley-Interscience, 1998).

[64] S. M. Sze and K. K. Ng, *Physics of Semiconductor Devices* (John Wiley & Sons, 2006).
[65] H. C. Card and E. H. Rhoderick, J. Phys. Appl. Phys. **4**, 1589 (1971).
[66] D. L. Pulfrey, IEEE Trans. Electron Devices **25**, 1308 (1978).
[67] PV Education, http://pveducation.org/
[68] M. H. Kryder, E. C. Gage, T. W. McDaniel, W. A. Challener, R. E. Rottmayer, G. Ju, Y.-T. Hsia, and M. F. Erden, Proc. IEEE **96**, 1810 (2008).
[69] G. E. W. Bauer, E. Saitoh, and B. J. van Wees, Nat. Mater. **11**, 391 (2012).
[70] N. Liebing, S. Serrano-Guisan, K. Rott, G. Reiss, J. Langer, B. Ocker, and H. Schumacher, Phys. Rev. Lett. **107**, 177201 (2011).
[71] C. Jaworski, J. Yang, S. Mack, D. Awschalom, J. Heremans, and R. Myers, Nat. Mater. **9**, 898 (2010).
[72] K. Uchida, J. Xiao, H. Adachi, J. Ohe, S. Takahashi, J. Ieda, T. Ota, Y. Kajiwara, H. Umezawa, and H. Kawai, Nat. Mater. **9**, 894 (2010).
[73] M. Hatami, G. E. W. Bauer, Q. Zhang, and P. J. Kelly, Phys. Rev. Lett. **99**, 066603 (2007).
[74] T. T. Heikkilä, M. Hatami, and G. E. W. Bauer, Phys. Rev. B **81**, 100408 (2010).
[75] J. Kimling, J. Gooth, and K. Nielsch, Phys. Rev. B **87**, 094409 (2013).
[76] M. J. Conover, M. B. Brodsky, J. E. Mattson, C. H. Sowers, and S. D. Bader, J. Magn. Magn. Mater. **102**, L5 (1991).
[77] L. Piraux, A. Fert, P. A. Schroeder, R. Loloee, and P. Etienne, J. Magn. Magn. Mater. **110**, L247 (1992).
[78] N. Liebing, S. Serrano-Guisan, P. Krzysteczko, K. Rott, G. Reiss, J. Langer, B. Ocker, and H. W. Schumacher, Appl. Phys. Lett. **102**, 242413 (2013).
[79] A. Boehnke, M. Walter, N. Roschewsky, T. Eggebrecht, V. Drewello, K. Rott, M. Münzenberg, A. Thomas, and G. Reiss, arXiv:1303.6553 (2013).

[80] M. Czerner and C. Heiliger, J. Appl. Phys. **111**, 07C511 (2012).
[81] G. Malinowski, Transport Dépendant Du Spin et Couplage D'échange : De La Jonction Tunnel Au Capteur Magnétique Intégré, Université Henri Poincaré - Nancy I, 2004.
[82] J. Nassar, M. Hehn, A. Vaurès, F. Petroff, and A. Fert, Appl. Phys. Lett. **73**, 698 (1998).
[83] J. Bernos, Elaboration de Jonctions Tunnel Magnétiques et de Jonctions Métal/oxyde/semi-Conducteur Pour L'étude Du Transport et de La Précession Du Spin D'électrons Chauds, Thèse de l'Université Henri Poincaré, Nancy, 2010.
[84] E. Steveler, Etude Des Mécanismes de Photoluminescence Dans Les Nitrures et Oxydes de Silicium Dopés Aux Terres Rares (Er, Nd), Université de Lorraine, 2012.
[85] Keithley 2182, http://www.keithley.fr/data?asset=15912
[86] Keithley 2000, http://www.keithley.fr/data?asset=3086
[87] Keithley, (2012), Making Precision Low Current and High Resistance Measurements.
[88] Stanford Research Systems, (2011).
[89] J. P. Heremans, B. Wiendlocha, and A. M. Chamoire, Energy Environ. Sci. **5**, 5510 (2012).
[90] J. P. Heremans, V. Jovovic, E. S. Toberer, A. Saramat, K. Kurosaki, A. Charoenphakdee, S. Yamanaka, and G. J. Snyder, Science **321**, 554 (2008).
[91] C. M. Jaworski, R. C. Myers, E. Johnston-Halperin, and J. P. Heremans, Nature **487**, 210 (2012).
[92] V. Drewello, J. Schmalhorst, A. Thomas, and G. Reiss, Phys. Rev. B **77**, 014440 (2008).
[93] F. Mahfouzi and B. K. Nikolić, Phys. Rev. B **90**, 045115 (2014).
[94] J. S. Moodera, J. Nowak, and R. J. M. van de Veerdonk, Phys. Rev. Lett. **80**, 2941 (1998).
[95] H. Çetin, B. Şahin, E. Ayyildiz, and A. Türüt, Phys. B Condens. Matter **364**, 133 (2005).
[96] Y. S. Ocak, M. F. Genisel, and T. Kılıçoğlu, Microelectron. Eng. **87**, 2338 (2010).

[97] W. Jiang, P. Upadhyaya, Y. Fan, J. Zhao, M. Wang, L.-T. Chang, M. Lang, K. L. Wong, M. Lewis, Y.-T. Lin, J. Tang, S. Cherepov, X. Zhou, Y. Tserkovnyak, R. N. Schwartz, and K. L. Wang, Phys. Rev. Lett. **110**, 177202 (2013).
[98] D. H. Auston, Appl. Phys. Lett. **26**, 101 (1975).
[99] L. Gravier, A. Fukushima, H. Kubota, A. Yamamoto, and S. Yuasa, J. Phys. Appl. Phys. **39**, 5267 (2006).
[100] L. Gravier, S. Serrano-Guisan, F. Reuse, and J. P. Ansermet, Phys. Rev. B **73**, 024419 (2006).

This thesis is devoted to the study of the effects of light on a magnetic tunnel junction (MTJ). A MTJ is made of a nanometer thick insulating layer sandwiched between the two magnetic layers. When an electric current is injected into such a structure, a voltage can be measured across the insulating layer. This voltage depends on the relative orientation of the magnetizations of the two magnetic layers. Generally, the resistance in the parallel configuration of the magnetizations is lower than in the antiparallel configuration and the variation of resistance can reach 600% at room temperature. This effect is known as the tunnel magnetoresistance and has been proposed to be used in new magnetic memories called MRAM. In those memories, the information is stored in the MTJ: a parallel configuration will correspond to a bit "0" while an antiparallel orientation will correspond to a "1". Measuring the voltage across the MTJ allows to read information.

In this thesis, we have shown that a voltage that dependents on the orientation of the magnetizations of the two magnetic layers can be measured when the junction is illuminated with light. Very high voltages up to several tens of millivolts have been measured. From a technological point of view, this effect could be used to read information in MRAM without the use of any external electric generator which causes power consumption. We were able to model the interaction of light and MTJ as an equivalent electrical generator and determine its characteristics. By studying the influence of the substrate and the position of the light spot on the sample, we have shown that the most important signals were observed when the spot light was close to the interface between the contacts and the semiconductor substrate (Si or GaAs). Further studies of the influence of the wavelength of the electromagnetic radiation and the temporal evolution of the voltage across the tunnel junction after a laser pulse were used to describe the phenomenon by considering a photoelectric effect and a Seebeck effect. In both cases, electric charges are generated and the presence a Schottky barrier at the interface between the semiconductor substrate and the contact of the MTJ is necessary to set the load through the MTJ. Finally we observe a voltage generated by the presence of a temperature gradient which can be described as an Anomalous Nernst effect.

Cette thèse porte sur l'étude des effets de la lumière sur une jonction tunnel magnétique (JTM). Une JTM est constituée d'une couche isolante d'épaisseur nanométrique prise en sandwich entre deux couches magnétiques. Lorsqu'un courant électrique est injecté dans une telle structure, une tension apparaît. Cette tension dépend de l'orientation relative des aimantations des 2 couches magnétiques. En général, lorsque l'orientation des deux aimantations est parallèle, la résistance est plus faible que dans la configuration antiparallèle. Cet effet est appelé « magnétorésistance tunnel » et a été proposé pour être utilisé dans de nouvelles architectures de mémoires magnétiques non volatiles à accès aléatoire, les MRAM. Dans ces mémoires, l'information est stockée grâce à des JTM : une configuration parallèle correspondra à un bit d'information « 0 » tandis qu'une orientation antiparallèle correspondra à un bit « 1 ». La mesure de la tension/résistance aux bornes des JTM permet donc de lire l'information stockée.

Dans cette étude, nous avons pu montrer qu'une tension dépendante de l'orientation relative des aimantations des couches magnétiques peut être mesurée lorsque la JTM est irradiée avec de la lumière. Des tensions très importantes atteignant plusieurs dizaines de millivolt ont pu être mesurées. Ce phénomène pourrait donc être utilisé pour lire l'information des MRAMs sans recourir à un générateur électrique extérieur qui entraine une consommation d'énergie. Nous avons pu modéliser l'interaction lumière-JTM comme un générateur électrique équivalent et en déterminer ses caractéristiques. En étudiant l'influence du substrat et la position du spot lumineux sur l'échantillon, nous avons pu montrer que les signaux les plus importants étaient observés lorsque la lumière éclairait un substrat semi-conducteur (Si ou GaAs) proche des contacts de la jonction tunnel. De plus, l'étude de l'influence de la longueur d'onde du rayonnement électromagnétique ainsi que de l'évolution temporelle de la tension aux bornes de la jonction tunnel après un pulse laser a permis de décrire le phénomène en considérant un effet photo-électrique et un effet Seebeck. Dans les deux cas, des charges électriques sont générées et la présence qu'une barrière Schottky à l'interface entre le substrat semi-conducteur et le contact de la JTM est nécessaire pour permettre aux charges de traverser la JTM. Enfin, nous observons une tension générée par la présence d'un gradient de température et qui peut être décrit comme un effet Nernst Anomal.